2014

Next Discoveries in Neutrino Mixing: Electron Neutrino Appearance

Hongyue Duyang
University of South Carolina - Columbia

Next Discoveries in Neutrino Mixing: Electron Neutrino Appearance

by

Hongyue Duyang

Bachelor of Science
Shandong University 2008

Submitted in Partial Fulfillment of the Requirements

for the Degree of Doctor of Philosophy in

Physics

College of Arts and Sciences

University of South Carolina

2014

Accepted by:

Sanjib R. Mishra, Major Professor

Varsha Kulkarni, Committee Member

Roberto Petti, Committee Member

Jeff Wilson, Committee Member

Rich Showman, Committee Member

Lacy Ford, Vice Provost and Dean of Graduate Studies

Dedication

This dissertation is dedicated to my parents.

Acknowledgments

First of all, great gratitude to Professor Sanjib R. Mishra, without whose guidance this dissertation would never be possible. His energy and understanding has encouraged me to go through the four years of my Ph.D study in this exiting area of neutrino physics, especially at the most difficult time of my career.

Many thanks to my committee members, Dr. Roberto Petti, Dr. Jeff Wilson, Dr. Varsha Kulkarni, and Dr. Richard Showman. Your guidances is greatly appreciated.

Many thanks to Prof. Purohit and Dr. Woochun Park for their great help when I first started my research on high energy physics. Thanks for taking your time to answer my naive questions and help me through the physics and softwares.

Many thanks to my colleagues and friends at University of South Carolina and Fermilab: Xinchun Tian, Jiajie Ling, Jae Jun Kim, Libo Jiang, Xinjie Qiu, Zukai Wang, Xuebing Bu, Barnali Chowdhury, Kuldeep Mann, and Nitin Yadav. Special thanks to Andrew Svenson and Tyler Alion for reading my thesis and correcting the English.

Abstract

The discovery of neutrino oscillation is a clear evidence of new physics beyond the Standard Model. Measurements of electron neutrino (ν_e) and electron anti-neutrino ($\bar{\nu}_e$) appearances are the most important channels to complete the neutrino mixing matrix. In a $\nu_e/\bar{\nu}_e$ appearance experiment, a near detector (ND) is used to constrain the neutrino flux and measure the backgrounds to the signal. Backgrounds to the ν_e appearance comes from Neutral Current Muon Neutrino Interactions (ν_μ-NC), Charged Current Muon Neutrino Interactions (ν_μ-CC), beam ν_e events and outside backgrounds. The background components are then extrapolated to the far detector (FD). By looking for excess of signal $\nu_e/\bar{\nu}_e$ -like events in FD, we measure the neutrino mixing angle, neutrino's mass hierarchy and the elusive CP-violation in the lepton sector.

This dissertation focuses on the signals and backgrounds in $\nu_e/\bar{\nu}_e$ appearance measurements. The first part of the dissertation presents an analysis of ν_e appearance in a large Water Cherenkov detector such as the one proposed by the LBNE collaboration. The analysis, including scanning thousands of events, aims to distinguish ν_e signals from the NC backgrounds. The second part of the dissertation presents measurements of Resonance Neutrino Interactions using the NOMAD data. This process plays a critical role in not only neutrino-nuclear cross section but also in the precision analysis of the next generation of neutrino oscillation experiments such as NOνA and LBNE. The last part of the dissertation discusses the method of using low-ν fit method to measure relative neutrino flux and constrain beam ν_e background.

Table of Contents

List of Tables

List of Figures

Chapter 1

Introduction

Neutrinos are leptons. They have no electric charge and interact only through the weak force. While the Standard Model predicts that neutrinos are massless the discovery of neutrino oscillation is a clear evidence of non-zero mass of neutrinos, and therefore provide a unique opportunity to explore the new physics beyond the Standard Model.

This chapter gives a general introduction on neutrino physics and experiments. Section 1 provides a historical view of neutrinos. Section 2 discusses basic neutrino interaction modes such as Quasi-Elastic, Resonance, Coherent and Deep-Inelastic, which are the signals and backgrounds in neutrino oscillation experiments. Section 3 presents the basics of neutrino oscillation physics. The historical and current status of neutrino oscillation experiments are discussed in Section 4. The last section focuses particularly on one type of neutrino oscillation experiment, ν_e appearance, which is the main topic of this thesis.

1.1 A Brief History of Neutrinos

Neutrinos were proposed by Wolfgang Pauli in 1930 in an effort to interpret the result of β decay experiments. In 1914, Chadwick found that electrons from β decay have a continuous spectrum of energy. It is a violation of the principle of energy and momentum conservation if electrons and neutrons are the only decay products as people thought. In what he called "a desperate remedy", Pauli proposed that β decay is a 3-body decay process instead of 2-body decay ($n \longrightarrow p + e^- + \bar{\nu}_e$). The additional

mystery particle should be neutral, spin 1/2, weakly interacting, and not yet known to people at that time. This concept was further developed by Enrico Fermi in 1930s.

The discovery of neutrino was made by Reines and Cowan in 1956 [1]. A detector was placed by the Savannah River nuclear plant to measure electron anti-neutrinos through inverse beta decay:

$$p + \bar{\nu}_e \longrightarrow n + e^+$$

They observed excesses of 1.23 ± 0.24 events/hour and 0.98 ± 0.22 events/hour in two independent run periods.

Shortly after the discovery of neutrino, Schiwinger and Nishijima predicted the existence of separate muon and electron neutrinos as muons decay weakly but not electromagnetically ($\mu \longrightarrow e + \gamma$). The existence of a second type of neutrino associated with muons was showed by Leon M. Lederman, Melvin Schwartz and Jack Steinberger in 1962.[2]. It was then well established that each charged lepton (e, μ) has a partner neutrino (ν_e, ν_μ).

The discovery of the third type of charged lepton, τ in 1975 at the Stanford Linear Accelerator Center suggested an associated neutrino (ν_τ). In 2000 by the DONUT collaboration at Fermilab announced the first detection of tau neutrino interactions.[3].

Today three generations of leptons are known. Each generation has one charged lepton and a corresponding neutrino with the same lepton number:

$$\begin{pmatrix} e \\ \nu_e \end{pmatrix} \begin{pmatrix} \mu \\ \nu_\mu \end{pmatrix} \begin{pmatrix} \tau \\ \nu_\tau \end{pmatrix} \tag{1.1}$$

In the Standard Model, neutrinos are known as massless, left handed, and interact with matter only through weak interactions, which will be discussed in the next section.

1.2 Neutrino Interactions

Neutrinos interact with matter through the weak force. There are two general types of interactions: charged current (CC) or neutral current (NC). In a charged current interaction, a W boson is exchanged causing the neutrino to change into a charged lepton, while in a neutral current interaction a Z boson is exchanged leaving the neutrino unchanged.

Neutrino interactions can be further divided into four different kinematic regions depending on its hadronic final states: Quasi-Elastic (QE), pion productions including Resonance (RES) and Coherent (COH), and finally Deep Inelastic Scattering (DIS). Cross-section of neutrino interactions are showed in figure **??** as a function of neutrino energy. At low energy ($< 1GeV$) Quasi-Elastic dominates. As energy goes up the RES and DIS interaction turns on one by one. At energy above a few GeV, the inclusive cross section increase linearly as a function of neutrino energy, as expected for point-like scattering of neutrinos from quarks, an assumption which breaks down at lower energies.

Neutrino interactions are historically measured for their importance in understanding the weak interaction and nuclear structure functions. Greater interests on them in recent years follow from neutrino oscillation experiments. Although neutrino oscillation experiments use both a near and far detector to measure interactions before and after oscillation which reduces uncertainties from cross-sections, those uncertainties can not be completely cancelled due to differences in detector efficiencies, flux, and interactions between the two detectors. The cross-section knowledge of neutrino interactions therefore is crucial for any oscillation search.

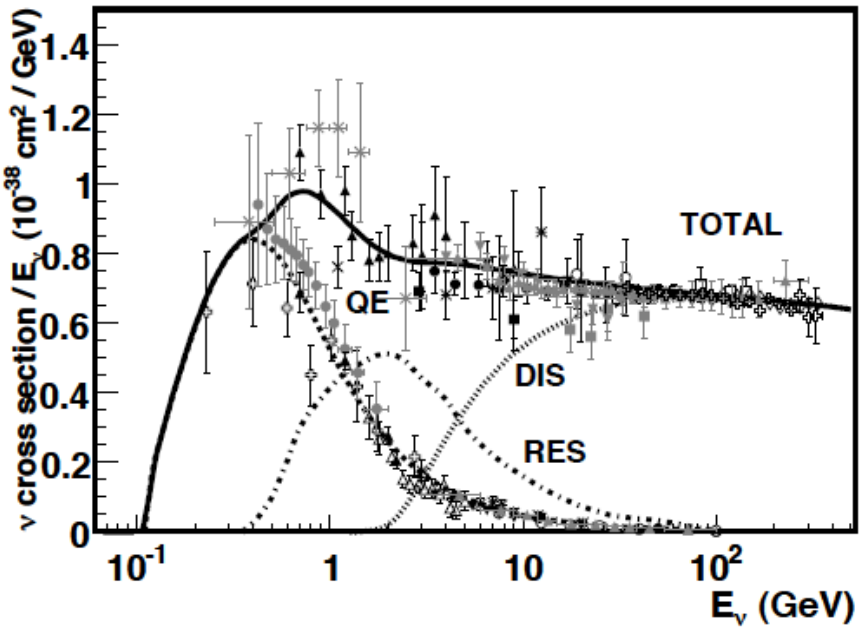

Figure 1.1 Neutrino per nucleon charged current cross sections divided by neutrino energy as a function of the energy. The Monte Carlo prediction is from the NUANCE generator. QE, RES, and DIS cross-sections are shown as well as total CC cross-section. The symbols are experiment data taken from ANL, PRD 16, 3103 (1977), BEBC, NP B343, 285 (1990), BNL, PRD 23, 2499 (1981), FNAL, PRD 28, 436 (1983) (D2), GGM, NC A38, 260 (1977), MiniBooNE, PRD 81, 092005 (2010), C, NOMAD, EPJ C63, 355 (2009), Serpukhov, ZP A320, 625 (1985), Al, SKAT, ZP C45, 551 (1990), BEBC, ZP C2, 187 (1979), MINOS, PRD 81, 072002 (2010), NOMAD, PLB 660, 19 (2008), NuTeV, PRD 74, 012008 (2006). [22]

Quasi-Elastic

QE is the dominate interaction for neutrino energy below 2 GeV. In a QE interaction the neutrino scatters off an entire nucleon rather than its constituent partons by exchange of the W boson. A neutron is converted to a proton in neutrino interaction, and the opposite happens in anti-neutrino interactions:

$$\nu_\mu n \longrightarrow \mu^- p,\ \bar{\nu}_\mu p \longrightarrow \mu^+ n$$

QE interaction provide a large source of signal events in many neutrino oscillation experiments operating in this energy range.

Resonance

When neutrino energy goes up, resonance interaction becomes important. The target nucleon becomes a baryon resonance which decays most often to a nucleon and pion.

$\nu + N \longrightarrow l + N^*$, $N^* \longrightarrow N' + \pi$

Other mode such as multi-pion production or photon production is also possible.

For single pion production, there are 7 possible channels, 3 for charged current interaction:

$$\nu_\mu p \longrightarrow \mu p \pi^+,\ \nu_\mu n \longrightarrow \mu n \pi^+,\ \nu_\mu n \longrightarrow \mu p \pi^0,$$

and 4 for neutral current interaction:

$$\nu_\mu p \longrightarrow \nu_\mu p \pi^0,\ \nu_\mu p \longrightarrow \nu_\mu n \pi^+,\ \nu_\mu n \longrightarrow \nu_\mu p \pi^-,\ \nu_\mu n \longrightarrow \nu_\mu n \pi^0.$$

The RES interaction is described by the Rein-Sehgal model [6].

RES is an important signal source for neutrino oscillation experiments with neutrino energy at few-GeV level. The π^0s from NC interaction also contribute to the background of ν_e appearance measurement. More about the theory and experiment of RES will be presented in chapter 3 of this thesis.

Coherent

The neutrino scatters coherently off a target nucleus. No quantum numbers (charge, spin, isospin) exchange and there is little momentum transfer between the lepton and nucleon. A single meson (π or ρ) is produced at small angles with respect to the incident neutrino. Both charged and neutral interactions are possible:

$$\nu_\mu A \longrightarrow \mu^- A \pi^+,\ \nu_\mu A \longrightarrow \mu^- A \rho^+$$
$$\nu_\mu A \longrightarrow \nu_\mu A \pi^0,\ \nu_\mu A \longrightarrow \nu_\mu A \rho^0$$

Coherent π production can be described by partially conserved axial current (PCAC) and Adler's theorem while coherent ρ is described by conserved vector current (CVC)

and vector meson dominance (VMD). The coherent process measurement thus provides the opportunity to probe the Lorentz structure of weak current as predicted by the theoretical models.

In addition to theoretical interest, measuring the coherent processes also has the following extra benefits in neutrino experiments. The neutrino induced and anti-neutrino induced charged current coherent interactions have identical signatures, namely outgoing charged leptons and charged mesons. Therefore by measuring the ratio of positive to negative charged mesons coherent production, one can obtain a constraint on the ratio of $\nu/\bar{\nu}$ flux. The cross-section of neutrino-induced coherent ρ^0 production can be related to that of well measured photon-induced ρ^0 production and thus makes an absolute flux measurement possible. Moreover, the feature of outgoing meson's near co-linearity with the incident neutrinos makes it possible to measure neutrino direction with good resolution and provide a constraint on neutrino beam divergence. Finally coherent-π^0 production makes up the background in ν_e appearance measurement.

Deep-Inelastic

DIS dominates the high energy region. In a DIS interaction the neutrino scatters off an individual quark inside the nucleon with large 4-momentum exchange through a W or Z boson, and produces a lepton and a hadronic shower in the final state. One can have NC or CC deep inelastic scattering:

$$\nu_\mu N \to \mu X,\ \bar{\nu}_\mu N \to \bar{\mu} X$$
$$\nu_\mu N \to \nu_\mu X,\ \bar{\nu}_\mu N \to \bar{\nu}_\mu X$$

The measurement of DIS is important in that it can be used to validate the Standard Model and probe nucleon structure. DIS is also the major source of background in many neutrino oscillation experiments.

Generally speaking, charged current interactions provide signal events in neutrino oscillation experiments since the neutrino type can be identified according to the emerging charged lepton. The cross-section knowledge is very important in any oscillation-searching experiments. The measurement of one of the important CC interactions in neutrino oscillation energy region, RES, will be presented in chapter 3. Neutral current interactions, on the other hand, usually make main backgrounds by mimicking charged lepton in its hadron products. It is important then to constrain NC type interactions in neutrino oscillation experiment. Chapter 2 of this thesis will present such an effort on LBNE.

1.3 Neutrino Oscillation: Physics

Standard Model predicts zero neutrino mass. However the discovery of neutrino oscillations is a clear evidence of non-zero neutrino mass, indicating new physics beyond Standard Model. Neutrino oscillation was first proposed by Pontercorvo and Sakata in 1957. This section will first introduce the theory behind it, and section 1.4 will discuss up-to-date experimental measurement of neutrino oscillation.

Suppose neutrinos have masses, with mass eigenstates $|\nu_i\rangle$. On the other hand, flavor eigenstates are written as $|\nu_\alpha\rangle$. Furthermore, suppose that flavor basis and mass basis may not be identical but are related by the Pontecorvo-Maki-Nakagawa-Sakata (PMNS) matrix [4]

$$|\nu_\alpha\rangle = \sum_{i=1}^{N} U^*_{\alpha i}|\nu_i\rangle \tag{1.2}$$

While neutrinos can only be detected in certain flavours, time evolution of neutrinos is based on mass eigenstate. A neutrino in mass eigenstate $|\nu_i\rangle$ with four-position $\mathbf{x}$ and four-momentum $\mathbf{p}$ evolve as:

$$|\nu_i(\mathbf{x})\rangle = e^{-i\mathbf{p}\cdot\mathbf{x}}|\nu_i(\mathbf{0})\rangle \tag{1.3}$$

If the neutrino energy E is much greater than neutrino mass m, the momentum can be approximated as:

$$p = \sqrt{E^2 - m^2} \simeq E - m_i^2/2E \tag{1.4}$$

Then we have

$$\mathbf{p} \cdot \mathbf{x} = Et - pL \simeq m_i^2 L/2E \tag{1.5}$$

And the evolution of neutrino becomes

$$|\nu_i(\mathbf{x})\rangle = e^{-im_i^2 L/2E}|\nu_i(\mathbf{0})\rangle \tag{1.6}$$

Now consider flavor mixing. Using PMNS matrix we get the evolution of neutrino in flavor eigenstates:

$$\begin{aligned} |\nu_\alpha(\mathbf{x})\rangle &= \sum_{i=1}^{N} e^{-im_i^2 L/2E} U_{\alpha i}^* |\nu_i(0)\rangle \\ &= \sum_{\beta} \sum_{i} e^{-im_i^2 L/2E} U_{\alpha i}^* U_{\beta i} |\nu_\beta(0)\rangle \end{aligned} \tag{1.7}$$

The probability of neutrinos starting from one flavor and ending up in another flavor is

$$\begin{aligned} P(\nu_\alpha \longrightarrow \nu_\beta) &= |\langle \nu_\alpha(\mathbf{x}) | \nu_\beta \rangle|^2 \\ &= \delta_{\alpha\beta} - 4 \sum_{i>j} Re(U_{\alpha i}^* U_{\beta i} U_{\alpha j} U_{\beta j}^*) \sin^2(\frac{\Delta m_{ij}^2 L}{4E}) \\ &\quad + 2 \sum_{i>j} Im(U_{\alpha i}^* U_{\beta i} U_{\alpha j} U_{\beta j}^*) \sin(\frac{\Delta m_{ij}^2 L}{2E}) \end{aligned} \tag{1.8}$$

where Δm_{ij}^2 is the difference between squared mass of i^{th} and j^{th} mass eigenstates. It is clear that if Δm_{ij}^2 is non-zero and U is not diagonal, there is a non-zero probability that neutrinos starting from one flavor α may oscillate into a different flavor β .

Consider 3-flavor mixing. The PMNS matrix can be written as a product of three rotation matrices based on 3 mixing angles (θ_{12}, θ_{23}, θ_{13}) between the mass eigenstates.

$$
\begin{aligned}
U &= \begin{pmatrix} 1 & 0 & 0 \\ 0 & c_{23} & s_{23} \\ 0 & -s_{23} & c_{23} \end{pmatrix} \begin{pmatrix} c_{13} & 0 & s_{13}e^{-i\delta} \\ 0 & 1 & \\ -s_{13}e^{i\delta} & & c_{13} \end{pmatrix} \begin{pmatrix} c_{12} & s_{12} & 0 \\ -s_{12} & c_{12} & 0 \\ 0 & 0 & 1 \end{pmatrix} \\
&= \begin{pmatrix} c_{12}c_{13} & s_{12}c_{13} & s_{13}e^{-i\delta} \\ -s_{12}c_{23} - c_{12}s_{23}s_{13}e^{i\delta} & c_{12}c_{23} - s_{12}s_{23}s_{13}e^{i\delta} & s_{23}c_{13} \\ s_{12}s_{23} - c_{12}c_{23}s_{13}e^{i\delta} & -c_{12}c_{23} - s_{12}c_{23}s_{13}e^{i\delta} & c_{23}c_{13} \end{pmatrix}
\end{aligned} \tag{1.9}
$$

where $c_{ij} \equiv \cos\theta_{ij}$ and $s_{ij} \equiv \sin\theta_{ij}$.

Using the PMNS matix, we can re-write the probability of neutrino oscillations in the form of mixing angles. For example the ν_μ to ν_e oscillation which is the focus of this thesis:

$$
\begin{aligned}
p(\nu_\mu \longrightarrow \nu_e) = {} & s_{23}^2 \sin^2 2\theta_{13} \sin^2 \frac{\Delta m_{31}^2 L}{4E} \\
& + c_{13}^2 c_{23}^2 \sin^2 2\theta_{12} \sin^2 \frac{\Delta m_{21}^2 L}{4E} \\
& + 8 c_{13}^2 s_{13} c_{12} s_{12} s_{23} c_{23} \sin^2 \frac{\Delta m_{21}^2 L}{4E} \sin^2 \frac{\Delta m_{31}^2 L}{4E} \cos(\frac{\Delta m_{32}^2 L}{4E} + \delta) \\
& - 2 s_{12}^2 s_{23}^2 \sin^2 2\theta_{13} \sin^2 \frac{\Delta m_{21}^2 L}{4E} \sin^2 \frac{\Delta m_{31}^2 L}{4E} \cos(\frac{\Delta m_{32}^2 L}{4E}) \\
& + 4 c_{13}^2 s_{12}^3 s_{13} s_{23} (s_{23} s_{13} s_{12} - 2 c_{12} c_{23} \cos\delta) \sin^2 \frac{\Delta m_{21}^2 L}{4E}
\end{aligned} \tag{1.10}
$$

Besides mixing angles, the oscillation probabilities also depends on the Dirac phase δ as well as neutrino mass spacing Δm_{ij}^2. The Dirac phase makes the neutrino and anti-neutrino oscillation probabilities differ, indicating CP violation. Previous experiments have shown that Δm_{ij}^2 is greater than Δm_{ij}^2 by 2 orders of magnitude. However, it is unknown whether m_3 is larger or smaller than m_1 and m_2. Therefore 2 mass hierarchies are possible at this point, referred to as the normal hierarchy and inverted hierarchy (Fig **??**). The measurement of mixing angles, CP violation and mass hierarchy are the main physics goals of neutrino experiments.

Now ν_μ to ν_e oscillation probability can be approximately written as:

$$p(\nu_\mu \longrightarrow \nu_e) \simeq s^2_{23} \sin^2 2\theta_{13} \sin^2 \frac{\Delta m^2_{13} L}{4E} \tag{1.11}$$

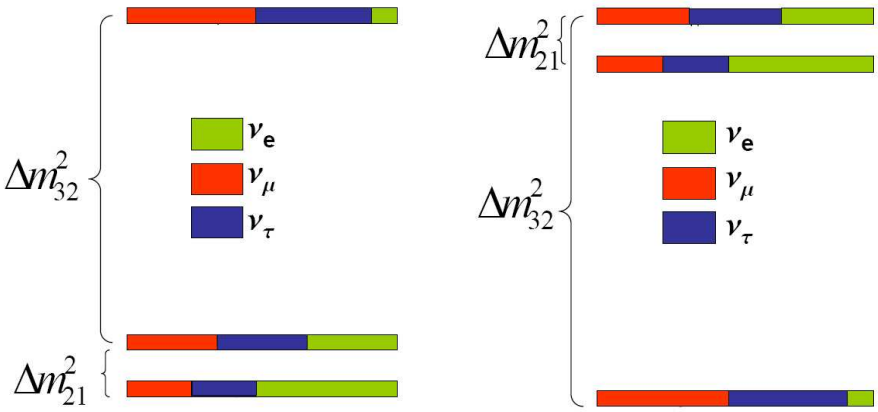

Figure 1.2 The two possible mass hierarchy states as we know today. The left is the normal hierarchy, where neutrino mass is sorted in the order $\nu_1 < \nu_2 < \nu_3$. The right shows another possibility called inverted hierarchy, where ν_3 has smaller mass than ν_1 and ν_2

Another issue greatly affect neutrino oscillation measurement is the matter effect [5]. Matter is composed of nucleons and electrons, and while all flavors of neutrino interact with them through neutral current scattering only the electron neutrinos interact with electrons through both the neutral current and the charged-current scattering. This effect significantly changes the position and the magnitude of the oscillation pattern measured by long baseline experiments. It is also sensitive to the sign of Δm^2, which allows for the determination of mass hierarchy.

1.4 Neutrino Oscillation: Experiments

There are two basic methods of oscillation searches: "disappearance" and "appearance". A disappearance experiment measures the survival probability of a neutrino flavor by counting the number of interactions in the detector and comparing it with the expected number assuming no oscillation. Appearance experiments, on the other

hand, look for new flavors in their detectors which are not present in the initial beam. Background is much smaller in appearance experiments compared to disappearance experiments so they can be sensitive to rather small values of the mixing angle.

There are four types of neutrino sources: solar, atmospheric, reactor, and accelerator.

Solar neutrinos are dominated by ν_e from nuclear interaction in the Sun. Atmospheric neutrinos are produced when cosmic rays (typically protons) hit the nuclei in the upper atmosphere. Pions are produced, then decay into neutrinos and charged leptons with a flux ratio of 2:1 muon neutrinos to electron neutrinos.

Historically solar and atmospheric neutrino experiments plays important roles in the discovery of neutrino oscillation. In 1968 Davis Homestake experiment found a deficit of neutrinos from the sun compared with the predictions of the standard solar model [7]. In 1988 a similar deficit of atmospheric muon neutrinos was observed by the Kamiokande experiment [8]. In 1998 the Super-Kamiokande experiment announced a very precise measurement of neutrino oscillation of atmospheric neutrino with a baseline of the diameter of the Earth [9]. In 2002 the SNO experiment made precise measurements of solar neutrino oscillation [10] [11].

Aside from solar and atmosphere sources, modern neutrino experiments also use neutrinos from reactors and accelerators to study neutrino oscillation. Reactor neutrinos are almost pure $\bar{\nu}_e$ from nuclear interactions. Examples of current reactor neutrino experiments includes Double Chooze, Daya Bay and RENO. They use a $\bar{\nu}_e$ flux from β decay in fusion reactors in the energy region of a few MeV. In 2003, the KamLAND experiment found the first evidence for reactor $\bar{\nu}_e$ oscillations [12].

Higher energy neutrinos can be produced at accelerators. Such experiments include MINOS, NOνA, and the proposed next generation experiment LBNE. They collide protons on a target, usually beryllium or carbon, and produce secondary mesons. Positive or negative charge meson are then focussed toward the direction of

the beamline with a magnetic device called a horn. The horn is able to focus one charge-sign and defocus the other to produce beams which are dominantly neutrinos or antineutrinos depending on the sign-selection. The beamline will also have a long secondary meson decay region where the mesons decay into neutrinos, predominately ν_μ. This is followed by a beam dump and an extended region of shielding to remove all particles except neutrinos. Accelerator beams have the advantage that they can be tuned to a specific energy range, for example ~ 1 GeV region where QE and one pion production dominate, which provide clear signals. An example of such an accelerator neutrino beam, the NUMI beam at Fermilab, will be discussed in Chapter 4.

The physics goal of neutrino oscillation experiments are to measure the mixing angle, mass hierarchy, and CP violation, as discussed in section 1.3. Super-Kamiokande, SNO, and KamLANB provided the first precision measurements of the solar oscillation parameters θ_{12} and Δm^2_{32} [10] [11] [12]. The limits they set are $\sin^2 2\theta_{12} \approx 0.86^{+0.03}_{-0.04}$ and $\Delta m^2_{32} \approx 8.0 \pm 0.3 \pm 10^{-5} eV^2$. Super-Kamiokande, K2K and MINOS measure atmospheric oscillation parameters as $\sin^2 2\theta_{23} > 0.92$ at 90% confidence level [13] [14]. Finally, Daya Bay experiment reports $\sin^2 2\theta_{13} = 0.091 \pm 0.016(stat) \pm 0.005(syst)$ [15].

1.5 ν_e Appearance Measurement

The focus of this thesis is one particular type of neutrino oscillation experiment: ν_e appearance measurement using muon neutrinos from an accelerator source. The approach of ν_e appearance analysis can be summarized in four steps:

1. Determine the selection criteria for ν_e candidate events.

2. Use the near detector to constrain the neutrino flux and measure the backgrounds.

3. Extrapolate background components measured at near detector to far detector, assuming no oscillations.

4. Look for excess of ν_e-like events in the far detector, measure mixing angles, mass hierarchy, and CP-violation.

The ν_μ to ν_e oscillation probability is given by equation 1.11. This measurement is sensitive to the 13 sector (θ_{13}, Δm^2_{31}) of the neutrino mixing, which is the least measured sector so far. The matter effects induced by long baseline increase the potential to search for CP-violating phase δ_{CP} and resolve mass hierarchy in the neutrino sector.

The signal events in ν_e appearance measurement are charged-current ν_e interactions. At low energy, the dominant interaction mode is QE. At the few-GeV level RES becomes important, and DIS dominates when the energy goes higher. They are characterized by an emerging electron which induce EM shower in neutrino detectors. Future ν_e appearance experiments, such as LBNE, will be sensitive to oscillation energy range at few-GeV level. To maximize the ν_e-appearance sensitivity, therefore, it is important not to bias the selection toward QE at the expense of RES and DIS channels. This requires a better understanding of the cross-section and the energy scales of various neutrino interactions.

The detector actually measures flux $\times$ cross-section, therefore any uncertainties from the cross-section will contribute to the uncertainties of oscillation measurement. One way to reduce these uncertainties is to use both a near and far detector to measure the interactions before and after oscillation. However, any differences in Far/Near detector can make them impossible to completely cancel. Therefore knowledge of neutrino interaction cross-section is crucial in ν_e appearance search.

Background to ν_e appearance measurement comes from neutral current muon neutrino Interactions (ν_μ-NC), charged current muon neutrino Interactions (ν_μ-CC), beam ν_e events, and outside backgrounds.

1. ν_μ-NC is the dominant background. In a ν_μ-NC event the outgoing muon neutrino is undetectable. The hadron shower, on the other hand, may generate

an energetic and forward π^0, which then decay into a pair of energetic photons: $\pi^0 \longrightarrow \gamma\gamma$. In many neutrino detectors, such as Water Cherenkov detectors, photons make similar EM shower as electrons and fakes the ν_e signal.

2. ν_μ-CC makes background when the low energy muon evades detection. Most ν_μ-CC events are characterized by a long, clean muon track and can be easily identified. However it is also possible to have events with high energy transfer from lepton to hadron shower which makes the muon track relatively short and hard to reconstruct. In this case ν_μ-CC contributes to the background just like ν_μ-NC.

3. Beam ν_e are the ν_e events from the beam rather than from oscillation. They are produced mainly form K^+, K_L and $\pi+$ decay. Beam ν_e is rather irreducible by any algorithm, but needs to be constrained by flux measurement.

4. Outside background refers to the particles coming from the outside of the detectors, including interaction induced by cosmic rays, and when neutrinos interact with materials such as wall of experimental hall and produce secondary particles which register hits in the detectors. Usually they can be measured and reduced to a very low level by selection cuts, but as they are very abundant even a small portion of the events can make dangerous background to ν_e appearance measurement.

This dissertation presents the studies of signals and backgrounds in ν_e appearance measurement. Chapter 2 will present an analysis of ν_e appearance in a large Water Cherenkov detector such as the one proposed by the LBNE collaboration. Its focus is the efficiency and sensitivity of ν_e signal measurement against NC backgrounds. Chapter 3 of the dissertation presents measurements of Resonance neutrino interactions using the NOMAD data. This process play a critical role in not only neutrino-nuclear cross section but also in the precision analysis of the next generation of neutrino oscillation experiments such as NOνA and LBNE. Chapter 4 the dissertation discusses the method of using low-ν fit method to measure relative neutrino flux and constrain beam ν_e background performed at NOνA near detector. An

effort to use cosmic-induced EM shower to check ν_e reconstruction in NOνA detectors is also included.

Chapter 2

ν_e appearance Analysis in A Large Water Cherenkov Detector for LBNE

LBNE is a long-baseline neutrino oscillation experiment proposed to measure ν_μ to ν_e oscillation. There were 2 far detector (FD) choices: a Water Cherenkov detector (WCD) or a Liquid Argon Time Projection Chamber (LArTPC). The collaboration's decision is critically influencing by the far detector's sensitivity to the electron-neutrino (ν_e) appearance. This sensitivity is dependent on the detection efficiency of the signal and background events, where in this case the signal is defined as ν_e-Charged Current (ν_e-CC) events and the background as ν_μ-Neutral Current (NC) events where π^0s from the hadronic shower mimic signal electron.

The proposed WC sensitivity is largely based upon extensions of the Super-Kamiokande (SuperK or SK) algorithm. The SK algorithm, however, is not optimized for the higher neutrino energies anticipated in LBNE, especially the 1.5$\sim$8 GeV region covering the first oscillation maximum.

This chapter presents an effort of simulation and hand-scan method in order to understand and characterize the NC background that corresponds with ν_e-CC signal. Signal and background efficiencies are estimated which, in turn, will yield a figure-of-merit for the sensitivity (FoM) of the WCD to the ν_e-CC appearance.

2.1 Introduction to Long-Baseline Neutrino Experiment (LBNE)

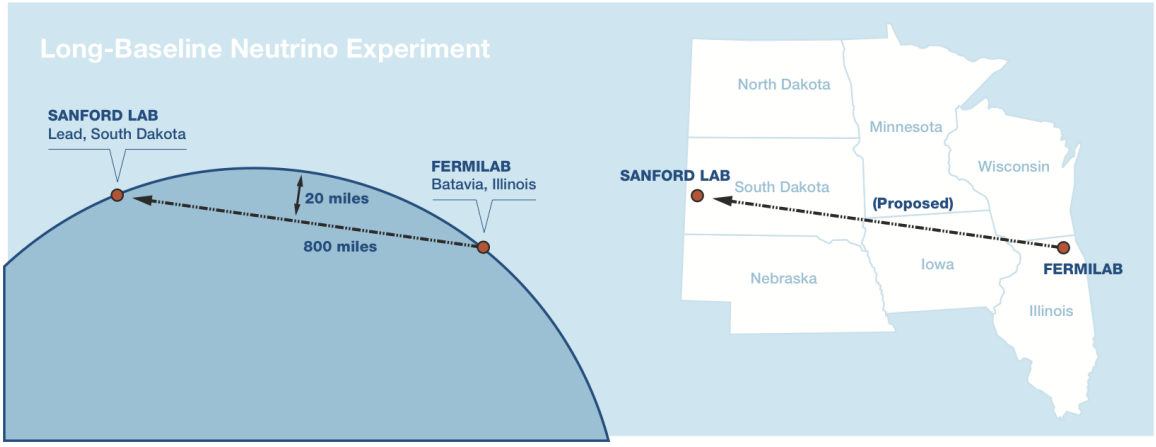

Figure 2.1 The proposed LBNE project showed on map. the beam will be generated at Fermilab site at Bartavia, IL, and a far detector is proposed to be located at Sanford, SD, with the baseline distance of 1300 km.

LBNE is designed with a 700 kW wide-band muon-neutrino beam from the Fermi National Accelerator Laboratory (FNAL) to the Sanford Underground Research Facility (SURF), South Dakota. The high intensity beam and long baseline (1300 km) of LBNE enable a decisive determination of the mass hierarchy and the CP-violation, as well as high precision measurement of oscillation parameters such as mixing angles and squared-mass differences. A fine-grained near detector is designed on the Fermilab site right downsteam of neutrino source to provide precision measurements of neutrino flux and neutrino interactions. Moreover, the shielding from cosmic rays provided by the deep underground far detector site enables the non-accelerator portion of the physics program, including nucleon decay searches, sensitive studies of neutrino bursts from galactic supernovae, and precision analyses of atmospheric neutrino samples [16].

While rich in various physics topics, LBNE's main scientific goal of measuring ν_μ to ν_e oscillation largely relies on its far detector's sensitivity to ν_e signal. Among two far detector choices proposed, Liquid Argon time Projection Chamber (LArTPC)

and Water Cherenkov Detector (WCD), LArTPC has the advantage of precise spatial and energy resolution and the ability of reconstructing complex neutrino interactions (figure 1.2). However, a LarTPC of such a large mass as proposed (34-kton) has never been built and incurs risk in building one for LBNE. WCD technology, on the other hand, is relatively mature thanks to experience from existing large detectors such as SuperK. A major drawback of WCD is its limited efficiency of identifying ν_e-CC from NC background. It is then critical to get a good understanding of WCD's ν_e sensitivity at the LBNE neutrino energy range, which is the focus of this chapter.

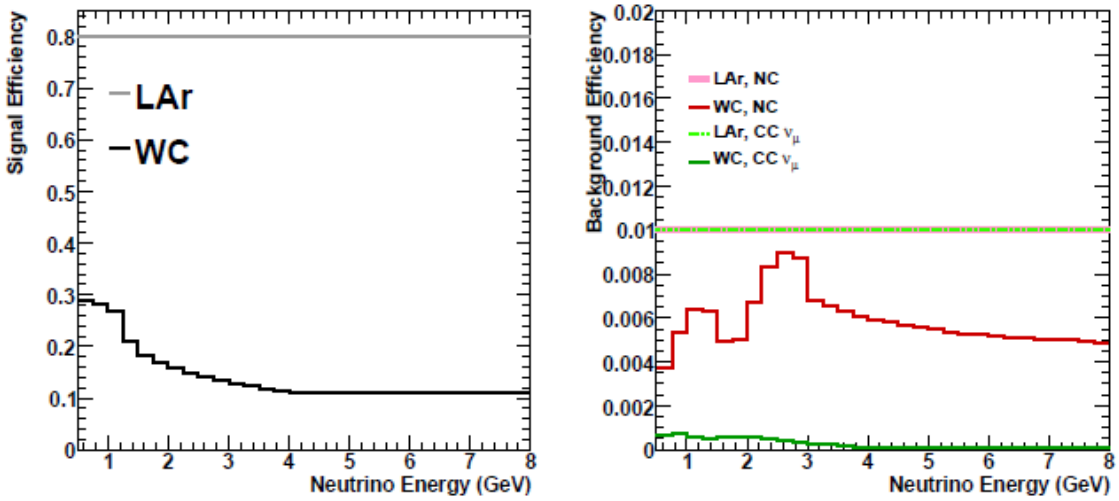

Figure 2.2 ν_e signal (left) and NC background (right) efficiencies of WCD vs LarTPC. The efficiencies are calculated based upon past experience of such detectors.

2.2 Water Cherenkov Detector

Cherenkov radiation is electromagnetic radiation emitted when a charged particle passes through a dielectric medium at a speed greater than the phase velocity of light in that medium. The radiation is at a fixed angle with respect to the direction of particle momentum, depending on particle velocity as well as diffraction factor:

$$\cos\theta = \frac{1}{n\beta} \tag{2.1}$$

Cherenkov radiation thus provide a way of detecting charged particles in high energy physics experiments.

A Water Cherenkov detector (WCD) is a large tank of clear water surrounded by photomultiplier tubes (PMT). Undoped oil may also be used, but water is much more affordable medium for a detector larger than a few ktons. Water acts as target as well as medium for Cherenkov radiation in a WCD. Neutrinos interact with water molecules and produce charged final state particles such as electrons, muons or pions. For example ν_e QE interaction: $\nu_e + n \rightarrow e^- + p$, or ν_μ QE: $\nu_\mu + n \rightarrow \mu^- + p$. The Cherenkov radiation produced by charged particle with velocity beyond threshold is detected by PMTs and converted to electronic signals. The projection of Cherenkov radiation on the detector wall is a ring called a Cherenkov ring.

Some characteristics of projected image of the Cherenkov ring can be used for particle identification. Muons are relatively heavier than electrons and produce a sharper ring. Electrons, on the other hand, are much lighter, and easily scatters and undergoes bremsstrahlung radiation. The radiated photon can also produce a electron-positrons pair, which may repeat the radiation process and produce an electromagnetic shower. Therefore the electron ring appears to be "fuzzy" compared to the muon ring. Figure 1.3 shows some example pictures of electron rings and muon rings in SuperK detector.

WCD proves to be capable of distinguishing electrons from muon with good efficiency as shown in figure 1.4 [17] [18]. The biggest background, however, comes from π^0s in hadronic showers from Neutral current muon neutrino interaction (ν_μ-NC). π^0s decay into a pair of energetic photons: $\pi^0 \rightarrow \gamma + \gamma$, which can also produce electromagnetic shower just like electrons. When one ring is missing, or the two over-lap, a single electron-like ring can be seen and mimic a true electron ring in WCD. Backgrounds also come from beam ν_e and ν_μ-CC events where muon energy is too small to be identified.

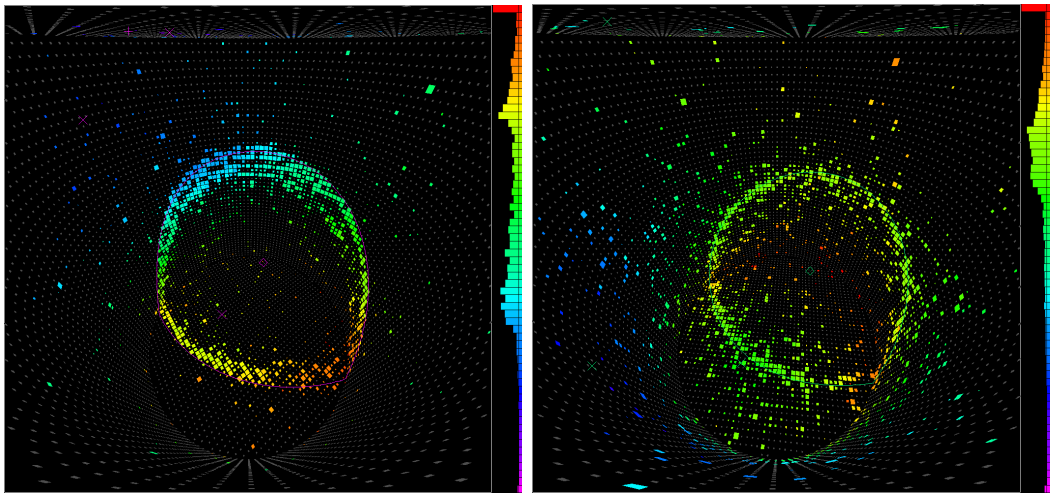

Figure 2.3 An example of a muon ring (left) and electron ring (right) in the SuperK Cherenkov detector using event display. Pictures taken from [19].

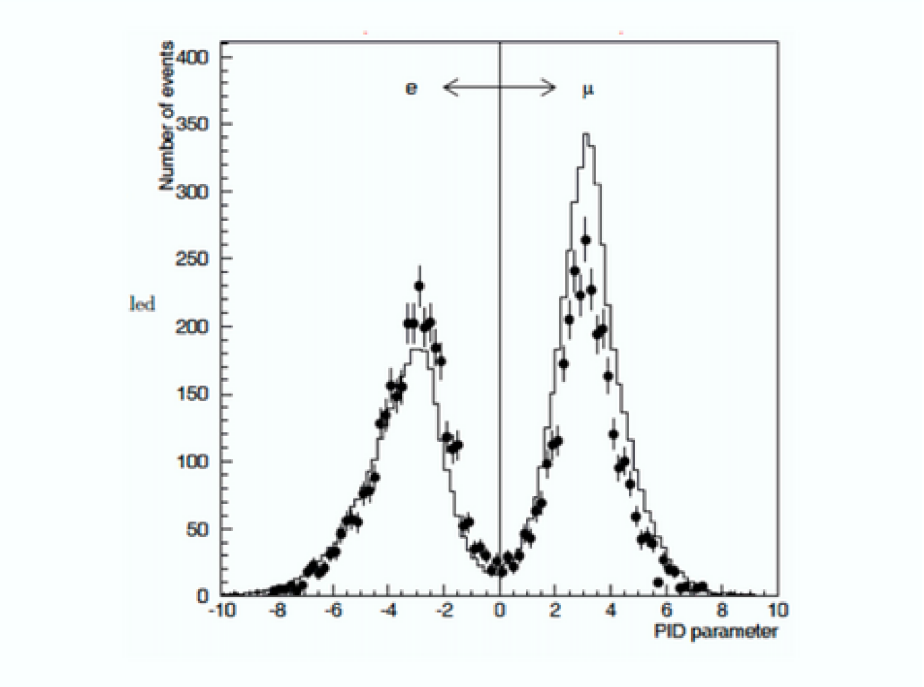

Figure 2.4 Particle identification parameter developed by SuperK to distinguish electrons from muons. Good separation can be seen between the electron peak and the muon peak.[18]

As shown above, the proposed WC sensitivity for LBNE is largely based upon extensions of the SuperK, not opimized for LBNE configuration. The following sections will present the method of simulation and hand scan we used to estimate the signal and background efficiencies.

2.3 WC simulation

The GENIE neutrino generator is used to generate neutrino interaction with water molecules. A sample of ν_μ events are generated following the proposed beam configuration of LBNE, with the fixed vertex at the origin. The vertices are then randomly distributed in a space corresponding to the fiducial volume of the detector.

A Geant4 package is built for the simulation of WCD response, named WCSim. The geometry of the detector used in the simulation is "DUSEL 100 kton", which is a cylinder with a radius of 26.6 m and hight of 60 m, instrumented with 10 inch, high QE photontube and with a 15% PMT coverage.

The Genie generated events are feed into WCSim, with random vertices in the fiducial volume which is 25 m in radius and 50 m in height. The output of WCSim is a rootfile containing WC neutrino events ready for scan and analysis.

The samples we use for scan contain about 1,000 ν_e-CC and about 10,000 ν_μ-NC events. Event pictures are generated for all events using the eventdisplay program for LBNE WC.

2.4 Scan Sample

In our study, we focus on three visible energy ranges between 0.5 GeV and 8 GeV. In considering the $0.5 \sim 1.5$ GeV range, which covers the second-oscillation maximum, we seek to confirm the consistency of our scan and analysis methods with those of Super-Kamiokande's estimates.

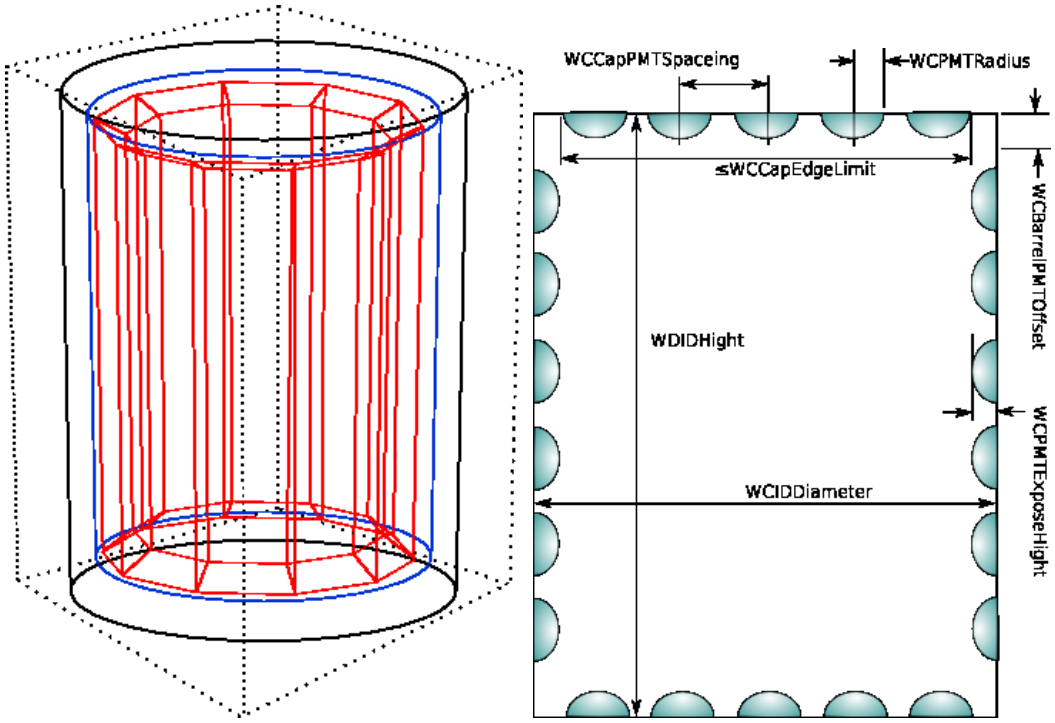

Figure 2.5 The simulation of WCD using Geant4. The large rectangular space showed in dash line is the world volume filled with water. The cylinders insides shows the outer and inter detector walls. PMTs are placed on the inter wall of the detector [20].

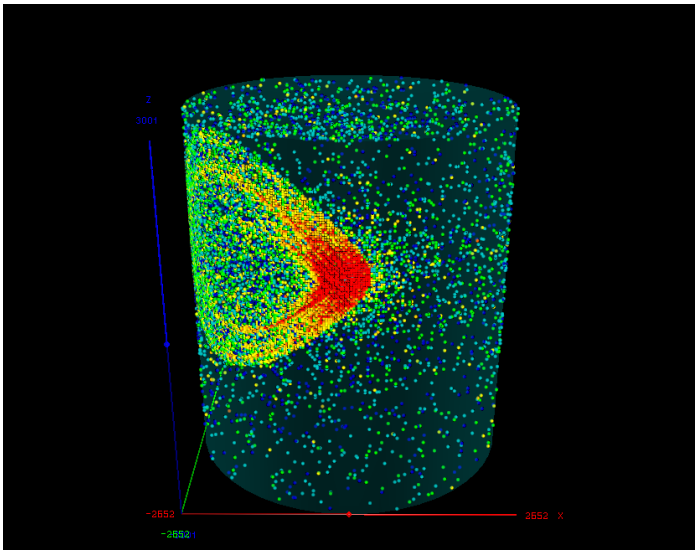

Figure 2.6 A simulated electron event in WCD showed in 3d event display.

The main focus of our work is on the $1.5 \sim 8$ GeV range. We divide it into two bins: $1.5 \sim 4$ GeV which envelops the first oscillation maximum, and $4 \sim 8$ GeV which can be treated as control-region, although with sufficient statistics oscillation effects should be visible up until about 8 GeV.

In order to deduce the visible energy necessary to arrange our samples into the above three energy bins, we consider the generated information by WCSim. ν_e-CC visible energy is the energy of the incoming neutrino while NC visible energy is the outgoing neutrino energy subtracted from the incoming neutrino energy. The visible energy distributions of ν_e-CC and ν_μ-NC are showed in Figure 1.7.

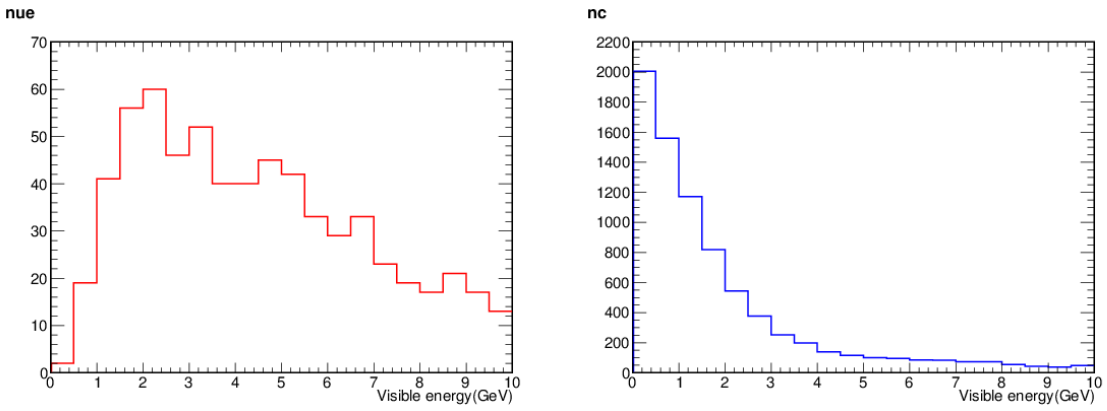

Figure 2.7 Visible energy distribution of ν_e-CC events (left) and ν_μ-NC (right)

To select scan sample, we further cut on electron energy (ν_e-CC) or π^0 energy (ν_μ-NC). For ν_e-CC events with visible energy between $1.5 \sim 8$ we require the electron energy to be greater than 1 GeV. For events in $0.5 \sim 1.5$ we require the electron energy to be greater than 0.25 GeV. Similar cuts are applied to NC events, but on energy of π^0 instead of electron. The numbers of events selected are showed in table 1.1 and 1.2.

The interaction modes of the events generated and scanned are examined. For ν_e-CC events the modes are classified into quasi-elastic (QE), resonance (Res), and

Table 2.1 ν_e-CC events selection

Visible Energy	All	$E_e > 1/0.25$ GeV
$1.5 \sim 8$ GeV	562	448
$0.5 \sim 1.5$ GeV	58	55

Table 2.2 ν_μ-NC events selection

Visible Energy	All	$E_{\pi^0} > 1/0.25$ GeV
$1.5 \sim 8$ GeV	3819	1019
$0.5 \sim 1.5$ GeV	1624	753

deep-inelastic scattering (DIS). The relevant modes of the NC events, dominated by the DIS process, are number of pions, especially π^0, in the final state. The fraction of these modes in the three E_{vis} rage are presented in the tables 1.3 to 1.8.

The tables show that the majority of the ν_e-CC events in the $0.5 \sim 8$ GeV range are due to resonance (Res) and deep-inelastic scattering (DIS). For example, in the $1.5 \sim 8$ GeV range, no more than 20% events are due to quasi-elastic (QE) interactions. To maximize the ν_e-appearance sensitivity, it is thus important not to bias the selection toward QE at the expense of Res and DIS channels. Such a selection also imposes an additional onus on LBNE to quantitate the cross-section and the energy scales of RES and DIS, in addition to QE. The NC background is dominated by events with ≥ 2 pions in the final state.

Table 2.3 ν_e-CC events in $0.5 \sim 1.5$ GeV

Interaction mode	QE	DIS	Res	Coh
Tot	26(44.8%)	7(12.1%)	25(43.1%)	0(0%)
Scanned	26(47.3%)	7(12.7%)	22(40%)	0(0%)

Table 2.4 ν_e-CC events in $1.5 \sim 4$ GeV

Interaction mode	QE	DIS	Res	Coh
Tot	70(25.7%)	109(40.1%)	85(31.2%)	3(1.1%)
Scanned	63(32.3%)	58(29.7%)	67(34.4%)	3(1.54%)

Table 2.5 ν_e-CC events in $4 \sim 8$ GeV

Interaction mode	QE	DIS	Res	Coh
Tot	36(12.4%)	204(70.3%)	39(13.4%)	1(0.345%)
Scanned	36(14.2%)	167(66%)	39(15.4%)	1(0.395%)

Table 2.6 NC events mode in $0.5 \sim 1.5$ GeV; 'n' refers to ≥ 2.

Mode	$1\pi^0$	nπ	$1\pi^+/\pi^-$	Coh
Tot	599(36.9%)	460(28.3%)	169(10.4%)	0(0%)
Scanned	483(64.1%)	270(35.9%)	0(0%)	0(0%)

Table 2.7 NC events mode in $1.5 \sim 4$ GeV; 'n' refers to ≥ 2.

Mode	$1\pi^0$	nπ	$1\pi^+/\pi^-$	Coh
Tot	210(7.34%)	2562(89.5%)	53(1.85%)	20(0%)
Scanned	133(24.4%)	412(75.6%)	0(0%)	0(0%)

Table 2.8 NC events mode in $4 \sim 8$ GeV; 'n' refers to ≥ 2.

Mode	$1\pi^0$	nπ	$1\pi^+/\pi^-$	Coh
Tot	19(1.99%)	937(97.9%)	0(0%)	0(0%)
Scanned	17(3.59%)	457(96.4%)	0(0%)	0(0%)

2.5 Scan Procedure

The procedure for scanning was undertaken in three stages: the formulation of a standard of reference, a period of training and self-correction, and the application of these two steps towards the measured set of events.

Scanning for all events was conducted by at least two persons working in tandem to reduce error. Each ring was proposed for inclusion on an empirical basis and assigned to the total count per event by category. These categories included "Clear Rings", "Not-So-Clear Rings", "Unclear Rings", and "Blob" rings. The "Blob" category was used to hold a type of miscellaneous ring that occurs when the vertex of the event is too close to the front wall of the detector to accurately resolve individual rings - resulting in a "blob" of active PMTs.

The creation of the standard of reference was undertaken with a small section of random events, where the scanners recorded their observations before referencing the corresponding true values of the event. The outcome of this was a solid definition of each category - Clear for very confident rings, Not-So-Clear to indicate a lower level of confidence, and Unclear to indicate even lower lever of confidence. These categories became stronger in their definitions with the training period, where a set of about 100 events were scanned and checked for coherence with true data. By this training we lower the level of mis-scan to 0.2% for clear rings, 2% for not-so-clear rings and 10% for unclear rings. This preparation helped to bolster a trustworthy set of scans for use in later statistical considerations.

With a low mis-scan rate for even unclear rings the number of rings in each event picture is calculated by adding up all three categories.

Thus, the classification of rings as Clear, Not-so-Clear, and Unclear served only to sharpen our scanning ability and played no further quantitative role in this analysis.

The detailed numbers of events in signal region (1.5 GeV - 4 GeV) and control region (4 GeV - 8 GeC) are listed in table 1.9 and table 1.10. Examples of 1-ring,

2-ring, 3-ring and 4+ ring categories are displayed in Figures 1.8 Only 1-ring (1R), 2-ring (2R), and 3-ring (3R) events are used in this analysis; events with 4+ ring events are not used.

Table 2.9 Number of (ν_e events classified into 1R, 2R, 3R and More-than-3R categories

Visible energy (GeV)	0.5 - 1.5	1.5 - 4	4 - 8	sum
Total generated	58	272	290	620
Total scanned	55	195	253	503
1R	24	59	41	124
2R	17	75	86	178
3R	9	47	69	125
More than 3R	5	14	30	49

Table 2.10 Number of NC events classified into 1R, 2R, 3R and More-than-3R categories

Visible energy (GeV)	0.5 - 1.5	1.5 - 4	4 - 8	sum
Total generated	1624	2862	957	5443
Total scanned	753	545	474	1772
1R	141	82	20	243
2R	391	215	107	713
3R	9	47	69	125
More than 3R	212	201	278	691

2.6 Analysis

After scan, the generated ID's were used to identify each ring as an electron ring (electron, positron or gamma) or a non-electron ring (muon or pion). By doing this we assume perfect ring identification in the Water Cherenkov detector, as the SuperK result suggested [17]. The generated particle energy was used as the energy of the ring. We then smear the momentum according to SuperK resolution (figure 1.9) and reconstruct the following variables:

1) P_t^L, which is the transverse momentum of the leading lepton with respect to the incoming neutrino.

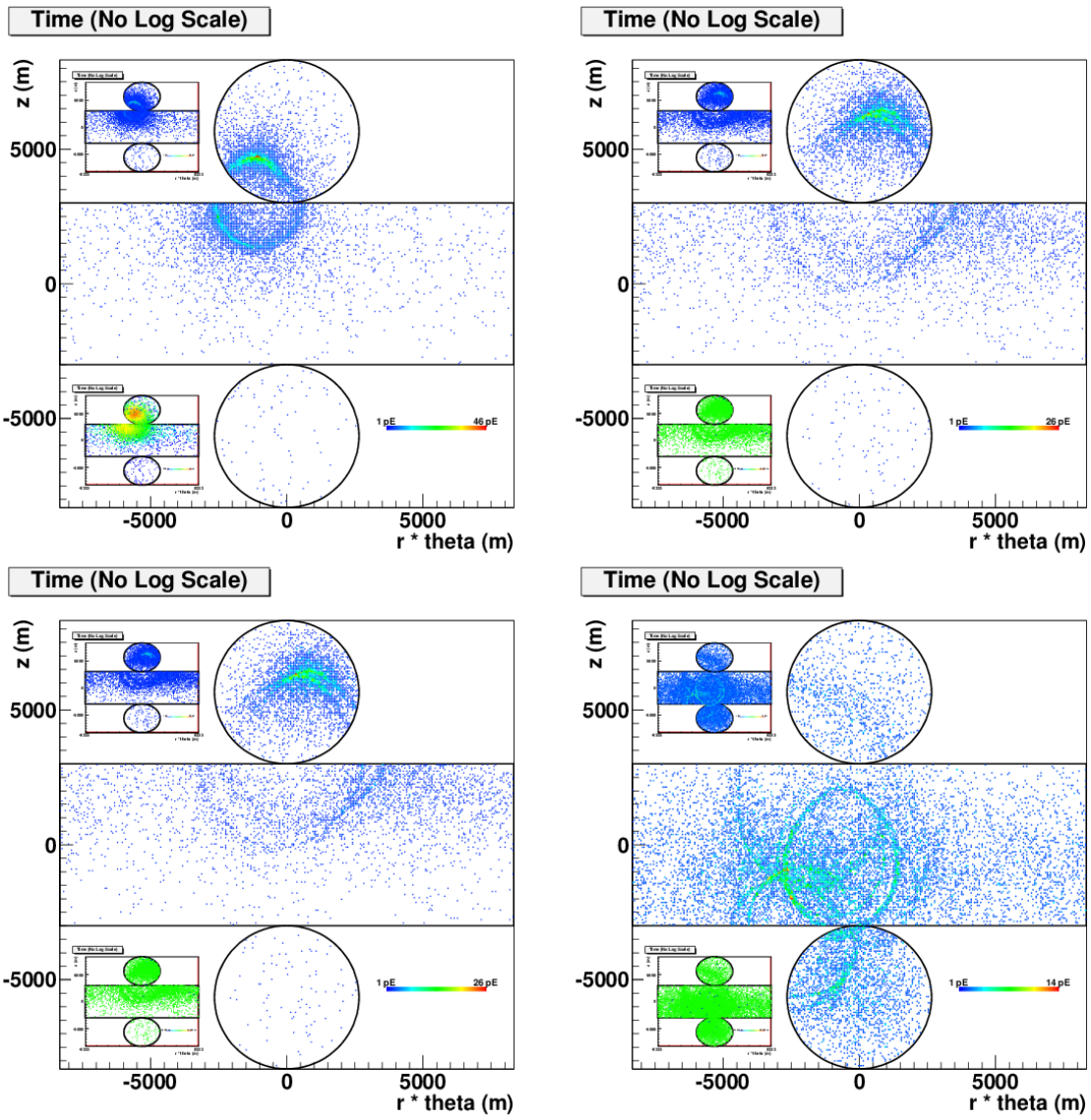

Figure 2.8 Example eventdisplay pictures of 1-ring event (top left), 2-ring event (top right), 2-ring event (bottom left) and more-than-4-ring event (bottom right)

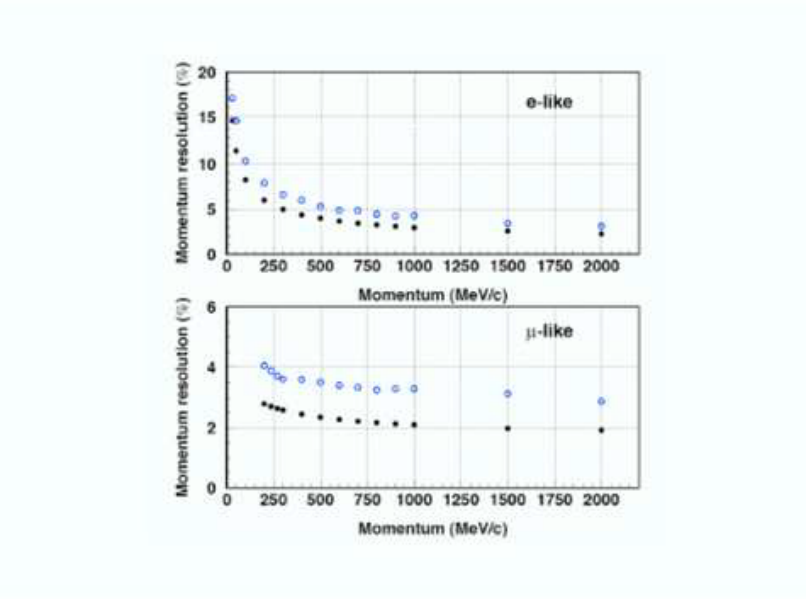

Figure 2.9 Electron-like (top) and muon-like (bottom) ring momentum resolution as measured in SuperK. [17]

2) P_t^{LH}, which is the transverse momentum of the leading lepton with respect to the second ring, if there is one.

3) M_{12}, which is the reconstructed mass using the 4-momentums of the leading ring and the second/third ring.

The distribution of those variables of nue and nc events were examined to decide cuts on them to reduce nc background.

We then apply cuts based on true and reconstructed kinematics on 1-ring, 2/3-ring events to reduce NC background.

For 1-ring events, the cuts are:

Cut 1: leading electron/gamma ring $\geq$ 300 MeV (for 0.5$\sim$1.5 GeV) or 1 GeV (for 1.5$\sim$4 GeV)

Cut 2: $P_t^L > 300$ MeV

For 2/3-ring events, the same cuts are applied as 1-ring, with 2 additional cuts on the reconstructed invariant mass M_{12} and P_t^{LH}. The cuts are:

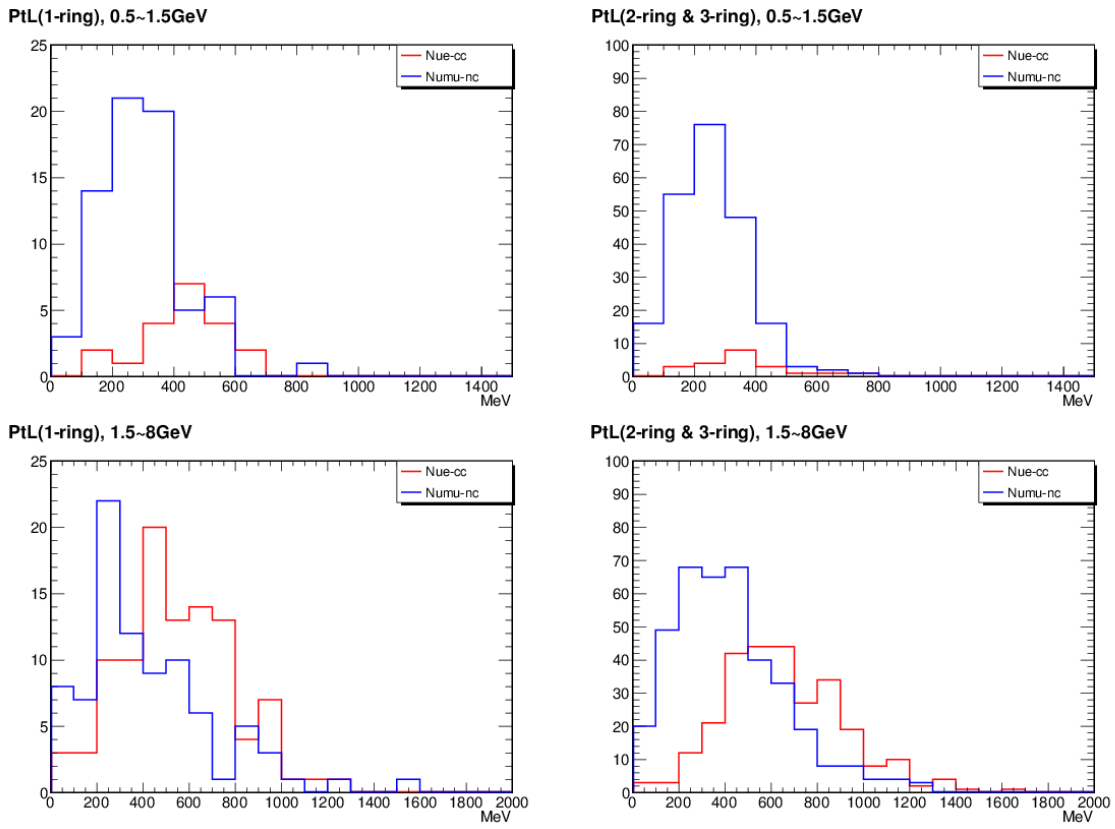

Figure 2.10 P_t^L distribution of 1R, 2R and 3R events in 0.5 $\sim$ 1.5 GeV region and 1.5 $\sim$ 8 GeV region.

Cut 1: leading electron/gamma ring $\geq$ 300MeV (for 0.5$\sim$1.5 GeV) or 1 GeV (for 1.5$\sim$4 GeV)

Cut 2: $P_t^L > 300$ MeV

Cut 3: 125 MeV$< M_{12} <$5 MeV (for 0.5$\sim$1.5 GeV) or $M_{12} > 175$ MeV (for 1.5$\sim$1.5 GeV)

Cut 4: $P_t^{LH} > 400$ MeV (for 0.5sim1.5 GeV) or $P_t^{LH} > 800$ MeV (for 1.5$\sim$4 GeV) or $P_t^{LH} > 900$ MeV (for 4$\sim$8 GeV)

The number of events after each cut are showed in table 1.11 $\sim$ 1.16.

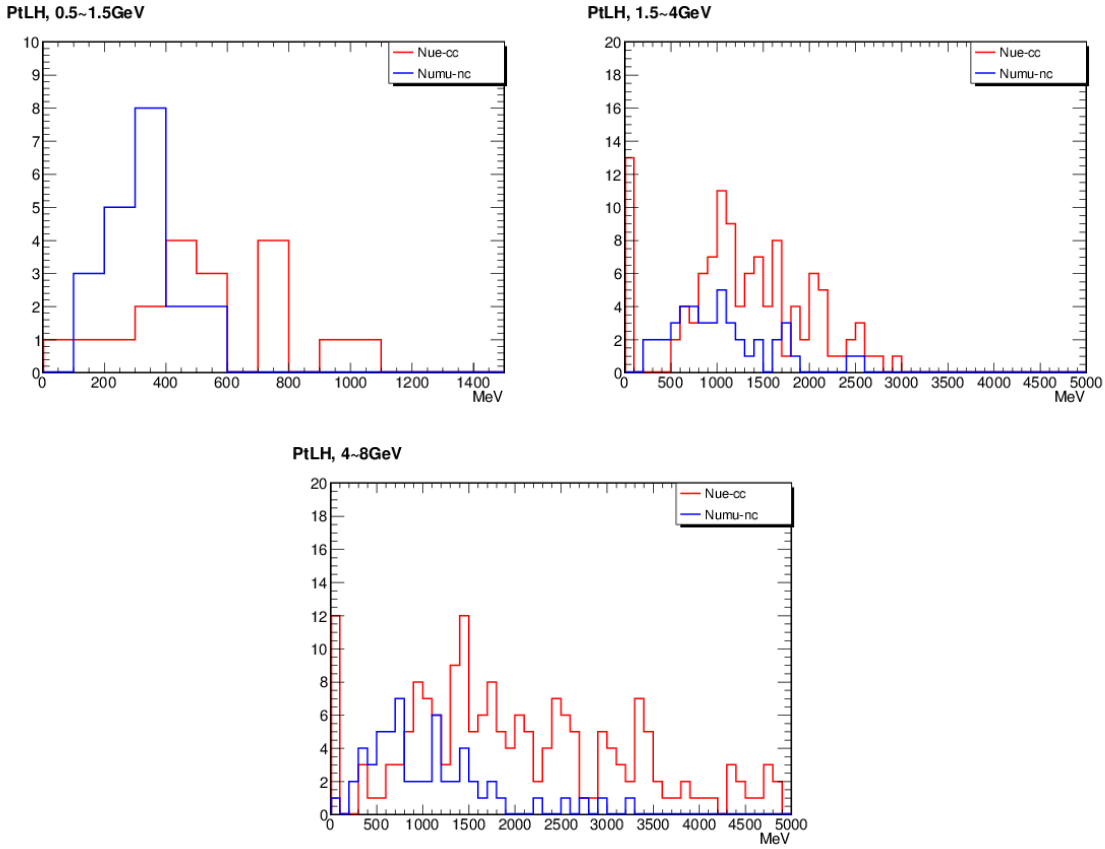

Figure 2.11 P_t^{LH} distribution of 1R, 2R and 3R events in 0.5 $\sim$ 1.5 GeV region and 1.5 $\sim$ 8 GeV region.

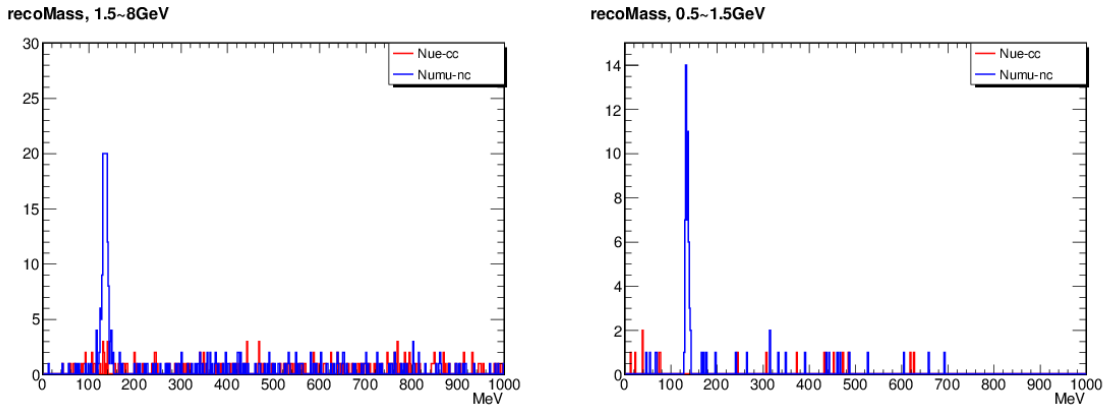

Figure 2.12 Reconstructed Mass of 2-ring and 3-ring events in 0.5 $\sim$ 1.5 GeV region and 1.5 $\sim$ 8 GeV region.

Table 2.11 Cut table for ν_eCC 1R events

Visible energy (GeV)	0.5 - 1.5	1.5 - 4	4 - 8	sum
Total scanned	24(41.4%)	59(21.7%)	41(14.1%)	124(20%)
cut1	20(34.5%)	59(21.7%)	41(14.1%)	120(19.4%)
cut2	18(31%)	50(18.4%)	34(11.7%)	102(16.5%)

Table 2.12 Cut table for NC 1R events

Visible energy (GeV)	0.5 - 1.5	1.5 - 4	4 - 8	sum
Total scanned	141(8.68%)	82(2.87%)	20(2.09%)	243(4.46%)
cut1	71(4.37%)	68(2.38%)	18(1.88%)	157(2.88%)
cut2	33(2.03%)	37(1.29%)	12(1.25%)	82(1.51%)

Table 2.13 Cut table for ν_eCC 2R events

Visible energy (GeV)	0.5 - 1.5	1.5 - 4	4 - 8	sum
Total scanned	17(29.3%)	75(27.6%)	86(29.7%)	178(28.7%)
cut1	13(22.4%)	75(27.6%)	84(29%)	172(27.7%)
cut2	10(17.2%)	65(23.9%)	81(27.9%)	156(25.2%)
cut3	10(17.2%)	54(19.9%)	76(26.2%)	140(22.6%)
cut4	7(12.1%)	38(14%)	60(20.7%)	105(16.9%)

Table 2.14 Cut table for NC 2R events

Visible energy (GeV)	0.5 - 1.5	1.5 - 4	4 - 8	sum
Total scanned	391(24.1%)	215(7.51%)	107(11.2%)	713(13.1%)
cut1	176(10.8%)	125(4.37%)	90(9.4%)	391(7.18%)
cut2	56(3.45%)	75(2.62%)	61(6.37%)	192(3.53%)
cut3	16(0.985%)	20(0.699%)	22(2.3%)	58(1.07%)
cut4	2(0.123%)	10(0.349%)	11(1.15%)	23(0.42%)

Table 2.15 Cut table for ν_eCC 3R events

Visible energy (GeV)	0.5 - 1.5	1.5 - 4	4 - 8	sum
Total scanned	9(15.5%)	47(17.3%)	69(23.8%)	125(20.2%)
cut1	8(13.8%)	47(17.3%)	69(23.8%)	124(20.0%)
cut2	4(6.9%)	42(15.4%)	69(23.8%)	115(18.5%)
cut3	4(6.9%)	29(10.7%)	59(20.3%)	92(14.8%)
cut4	2(3.45%)	24(8.82%)	48(16.6%)	74(11.9%)

Table 2.16 Cut table for NC 3R events

Visible energy (GeV)	0.5 - 1.5	1.5 - 4	4 - 8	sum
Total scanned	171(10.5%)	169(5.9%)	148(15.5%)	488(8.97%)
cut1	45(2.77%)	85(2.97%)	89(9.3%)	219(4.02%)
cut2	11(0.677%)	50(1.75%)	66(6.9%)	127(2.33%)
cut3	1(0.062%)	12(0.42%)	18(1.9%)	31(0.57%)
cut4	0(0%)	6(0.2%)	6(0.6%)	12(0.22%)

Table 2.17 Cut table for cumulative ν_e events

Visible energy (GeV)	0.5 - 1.5	1.5 - 4	4 - 8	sum
Total generated	58	272	290	620
Total scanned	55(94.8%)	195(71.7%)	253(87.2%)	503(81.1%)
cut1	41(70.7%)	181(66.5%)	194(66.9%)	416(67.1%)
cut2	32(55.2%)	157(57.7%)	184(63.4%)	373(60.2%)
cut3	32(55.2%)	133(48.9%)	169(58.3%)	334(53.9%)
cut4	27(46.6%)	112(41.2%)	142(49%)	281(45.3%)

2.7 Signal and Background Efficiencies

The ν_e-CC efficiency of 1-ring events is defined as the number of 1-ring ν_e-CC events after all cuts within each energy range divided by the corresponding number of generated events. The ν_e-CC and NC efficiencies are also plotted as a function of visible energy in Fig 1.13, and similarly we define efficiencies for 2-ring and 3-ring events, showed in figure 1.14.

Adding up 1-ring, 2-ring and 3-ring categories gives us the cumulative efficiencies, showed in figure 1.15. The cut table for cumulative ν_e and NC events are showed by table 1.17 and 1.18. In the first oscillation region ($1.5 \sim 4$ GeV) the ν_e-CC efficiency is 41.2% and the corresponding NC background efficiency is 1.85%. In the second oscillation region ($1.5 \sim 4$ GeV) the ν_e-CC efficiency is 46.6% and the corresponding NC background efficiency is 2.16%

Finally we define the sensitivity FoM of the WC detector as ν_e-Eff/$\sqrt{NC - Eff}$. By this definition we get the sensitivity in the first oscillation region to be

$FoM(0.5GeV \sim 1.5GeV) = 41.2\%/\sqrt{1.85\%} = 30.3$,

Table 2.18 Cut table for cumulative NC events

Visible energy (GeV)	0.5 - 1.5	1.5 - 4	4 - 8	sum
Total generated	1624	2862	957	5443
Total scanned	753(46.4%)	545(19%)	474(49.5%)	1772(32.6%)
cut1	292(18%)	278(9.71%)	197(20.6%)	767(14.1%)
cut2	100(6.16%)	162(5.66%)	139(14.5%)	401(7.37%)
cut3	50(3.08%)	69(2.41%)	52(5.43%)	171(3.14%)
cut4	35(2.16%)	53(1.85%)	29(3.03%)	117(2.15%)

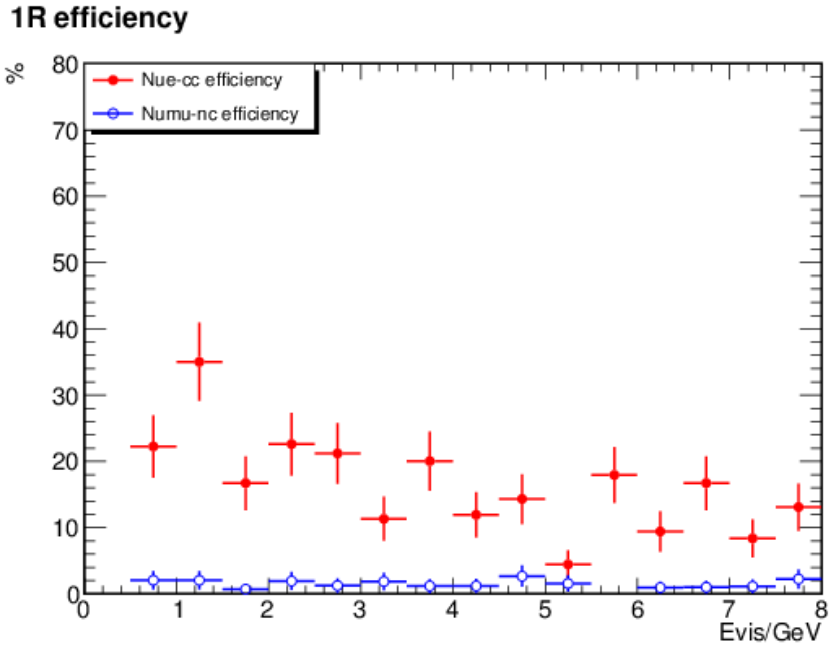

Figure 2.13 1-ring event efficiencies of ν_e-CC and NC

and in the second oscillation region it is

$FoM(0.5GeV \sim 1.5GeV) = 46.6\%/\sqrt{2.16\%} = 31.4.$

2.8 Composition of Surviving ν_e-CC and NC Events

We conducted a simple analysis of the composition of ν_e-CC signal and NC background. For the NuECC events generated, scanned, and cut, we examined the interaction modes QE, DIS, Res, and Coh. For NC the numbers of pions were counted. The table 1.19 $\sim$ 1.24 the interaction modes of all events in the sample, scanned events and those after the cuts. They show that the scan preferentially picks out

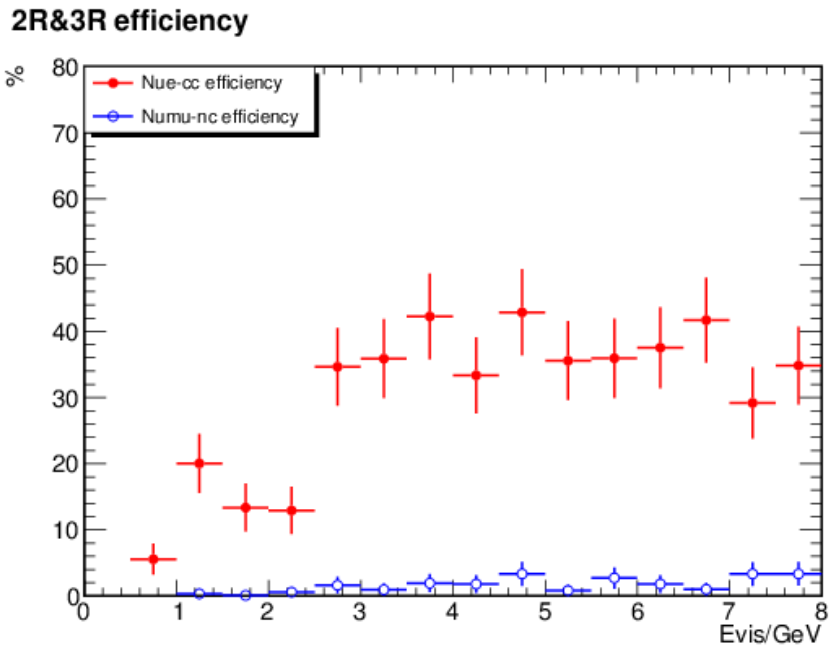

Figure 2.14 2-ring and 3-ring event efficiencies of ν_e-CC and NC

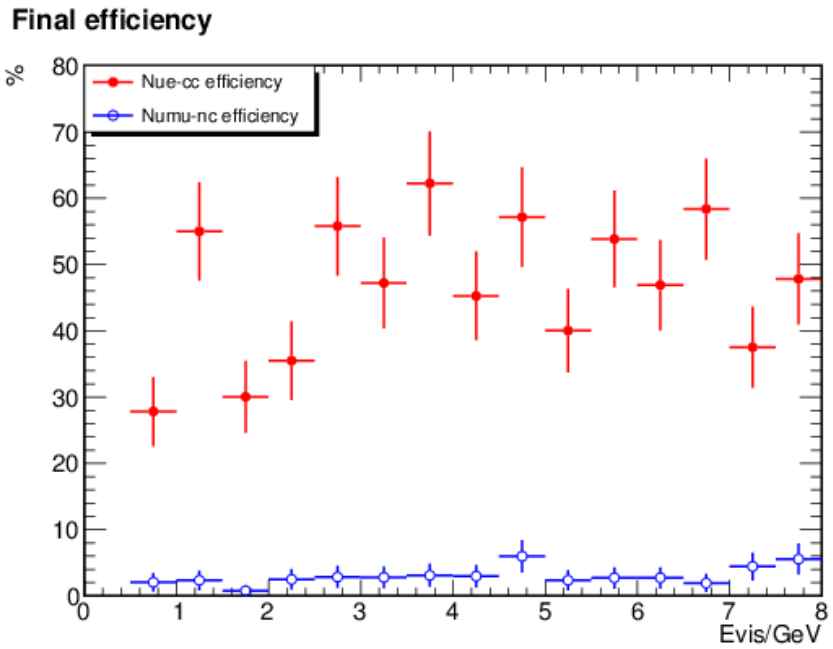

Figure 2.15 Cumulative efficiencies of ν_e-CC and NC.

Table 2.19 ν_e-CC event modes in 0.5 $\sim$ 1.5 GeV

Interaction mode	QE	DIS	Res	Coh
Tot	26(44.8%)	7(12.1%)	25(43.1%)	0(0%)
Scanned	26(47.3%)	7(12.7%)	22(40%)	0(0%)
After cuts	17(58.6%)	15(51.7%)	10(34.5%)	0(0%)

Table 2.20 NC event modes in 0.5 $\sim$ 1.5 GeV

Mode	$1\pi^0$	nπ	$1\pi^+/\pi^-$	Coh
Tot	599(36.9%)	460(28.3%)	169(10.4%)	0(0%)
Scanned	483(64.1%)	270(35.9%)	0(0%)	0(0%)
After cuts	66(90.4%)	7(9.59%)	0(0%)	0(0%)

Table 2.21 ν_eCC event modes in 1.5 $\sim$ 4 GeV

Mode	QE	DIS	Res	Coh
Tot	70(25.7%)	109(40.1%)	85(31.2%)	3(1.1%)
Scanned	63(32.3%)	58(29.7%)	67(34.4%)	3(1.54%)
After cuts	29(25.2%)	57(49.6%)	44(38.3%)	1(0.87%)

lower-Y_{BJ} ν_e-CC events, but by no means only QE. The surviving NC-events are dominated by ≥ 2 π^0.

2.9 Conclusion

To summarize the work: an analysis of ν_e-appearance sensitivity in a Water Cherenkov detector (WCD) is conducted in the proposed LBNE neutrino beam. A sample of 500 ν_e charged current (ν_e-CC) and 1800 neutral current (NC) events, simulated randomly across the fiducial volume of a 100-kT WCD instrumented with 10-inch, high-QE PMTs with a 15% coverage is scanned. The signal ν_e and the background NC events are mixed before scanning in an attempt to conduct a 'blind' scan. Each subsample, composed of signal plus background events, is scanned by at least two

Table 2.22 NC events mode in 1.5 $\sim$ 4 GeV

mode	$1\pi^0$	nπ	$1\pi^+/\pi^-$	Coh
Tot	210(7.34%)	2562(89.5%)	53(1.85%)	0(0%)
Scanned	133(24.4%)	412(75.6%)	0(0%)	0(0%)
After cuts	16(30.2%)	37(69.8%)	0(0%)	0(0%)

Table 2.23 ν_eCC events mode in $4 \sim 8$ GeV

Interaction mode	QE	DIS	Res	Coh
Tot	36(12.4%)	204(70.3%)	39(13.4%)	1(0.345%)
Scanned	36(14.2%)	167(66%)	39(15.4%)	1(0.395%)
After cuts	15(10.3%)	90(62.1%)	28(19.3%)	0(0%)

Table 2.24 NC events mode in $4 \sim 8$ GeV

mode	$1\pi^0$	nπ	$1\pi^+/\pi^-$	Coh
Tot	19(1.99%)	937(97.9%)	0(0%)	0(0%)
Scanned	17(3.59%)	457(96.4%)	0(0%)	0(0%)
After cuts	7(25%)	21(75%)	0(0%)	0(0%)

persons. Scan events are smeared following the Super-Kamikande (SK) resolution, and subjected to simple kinematic cuts to arrive at a ν_e-CC and NC efficiency as a function of visible energy. A Figure-of-Merit for the sensitivity (FoM) is defined as $FoM = \nu_e - Eff/\sqrt{NC - Eff}$ Although the focus of the scan-study is in the energy range 1.5–8 GeV covering the first oscillation maximum, we have also included events in the 0.5–1.5 GeV region.

From the scan, we find the majority (75%) of ν_e-CC signal are induced by deep inelastic scattering (DIS) and resonance (Res); about 25% of the signal are due to quasi-elastic (QE) interactions. The background NC are dominated by events with ≥ 2 pions in the final state, where one of the two photon evades detection either by lying on top of the other or by being the product of highly asymmetric decay. The final efficiencies we get in $0.5 \leq E_{vis} \leq 1.5$ GeV are 46.6% for ν_e and 2.2% for NC, with $FoM = 31.4$; and in $1.5 \leq E_{vis} \leq 4$ GeV are 41.2% for ν_e and 1.9% for NC, with $FoM = 30.3$.

This study proves a large Water Cherenkov detector's capability in serving as the far detector for future ν_e appearance oscillation experiments. Moreover, it has been shown that in few-GeV neutrino energy region which covers the $\nu_\mu \longrightarrow \nu_e$ oscillation maximum, the interactions have large contributions from RES and DIS other than QE. To maximize the ν_e-appearance sensitivity, it is thus important not to bias the

selection toward QE at the expense of RES and DIS channels. A better understanding of cross-section and the energy scales of RES and DIS is therefore crucial to future oscillation experiments such as LBNE.

Chapter 3

Resonance Neutrino Interactions Measurement In NOMAD Detector

This chapter presents a measurement of charged current resonance neutrino interaction (RES) in NOMAD detector. Resonance interaction is an important contribution to ν_e signal in neutrino oscillation experiments with few-GeV level neutrino energy. A precise knowledge of RES cross-section is important in not only neutrino-nuclear interaction itself but also in the precision analysis of the next generation of neutrino oscillation experiments such as NOνA and LBNE.

NOMAD is a neutrino experiment on CERN SPS beam designed for the searching of ν_μ to ν_τ oscillation. The large sample of high-resolution data accumulated by NOMAD detector is an excellent sample for neutrino interaction studies.

In this chapter, we take 2 channels of RES interaction mode in NOMAD detector: 3-track final states (muon, proton and charged pion) and 2-track final states (muon, proton or charged pion). They are measured separately and give consistent result with each other. The method of Neural Network is implemented in the analysis of both channel. The two channels are then combined to give a very precise final measurement of inclusive RES interaction. This combined analysis method reduces both statistic and systematic uncertainties.

Section 3.1 of this chapter outlines the physics of resonance interaction. Section 3.2 gives an brief introduction to NOMAD experiment at CERN. The MC simulation and signal/background of RES measurement is discussed in section 3.3 and 3.4. 3-

track and 2-track analysis are presented separately in the sections 3.5 and 3.6. In section 3.7, the two channels are combined to give a final measurement, in the form of ratio of CCRES with respect to inclusive CC as well as the cross-section. A systematic study is performed in section 3.8.

3.1 Resonance: Physics and Motivation

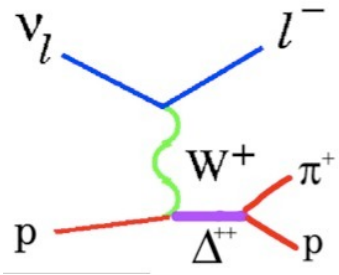

Figure 3.1 Feynman diagram showing a resonance interaction with a Δ^{++} intermediate state which decays into a proton and a π^+.

Neutrino can inelastically scatter off target nucleon, with a short term resonant state of the excited target nucleon created (N^*, Δ) and then almost immediately decays, most often into a nucleon and a single pion, which is the focus of this chapter. Other decay modes are also possible, such as multi-pion, different mesons or photons production.

There are three possible channels for charged current resonance 1π production. The intermediate states have isospin 1/3 or 2/3, and the decay product are a proton or neutron plus a charged or neutral pion. For ν_μ, they are

$$\nu_\mu + p \longrightarrow \mu + p + \pi^+$$
$$\nu_\mu + n \longrightarrow \mu + n + \pi^+$$
$$\nu_\mu + n \longrightarrow \mu + p + \pi^0$$

For neutral current current, four channels are possible:

$$\nu_\mu + p \longrightarrow \nu_\mu + p + \pi^0$$
$$\nu_\mu + p \longrightarrow \nu_\mu + n + \pi^+$$
$$\nu_\mu + n \longrightarrow \nu_\mu + p + \pi^-$$
$$\nu_\mu + n \longrightarrow \nu_\mu + n + \pi^0$$

And there are 7 corresponding interaction channels for $\bar{\nu}_\mu$.

Resonance interaction are described by Rein-Seghal (RS) model[6]. Figure 2.1 shows the Feynman diagram of the resonance interaction with a Δ^{++} intermediate state. The interaction can be divided into Lepton current part and hadron current part. In the limit of $m_l = 0$, the matrix element is written as

$$T(\nu_\mu N \longrightarrow \mu^- N^*) = \frac{G}{\sqrt{2}} \left[\bar{\mu}_l \gamma^\beta (1-\gamma_5)\mu_\nu\right] \left\langle N|J^+_\beta(0)|N^*\right\rangle \tag{3.1}$$

where $G = G_F \cos\theta_C$.

$\bar{\mu}_l \gamma^\beta (1-\gamma_5)\mu_\nu$ is the lepton current part. It can be expanded in the rest frame of the resonance as

$$\bar{\mu}_l \gamma^\beta (1-\gamma_5)\mu_\nu = -2\sqrt{2}E_\nu \sqrt{\frac{Q^2}{|\boldsymbol{q}|^2}} (\mu e^\mu_L - \nu e^\mu_R + \sqrt{2\mu\nu} e^\mu_S) \tag{3.2}$$

where Q^2 is the momentum transfer, $\mu = \frac{E+E'+Q}{2E}$, $\nu = \frac{E+E'-Q}{2E}$. The left-handed, right-handed and scalar polarization vector are:

$$e^\mu_L = \frac{1}{\sqrt{2}}(0,1,-i,0), e^\mu_R = \frac{1}{\sqrt{2}}(0,-1,-i,0), e^\mu_S = \frac{1}{\sqrt{Q^2}}(Q^*,0,0,\nu^*) \tag{3.3}$$

$\left\langle N|J^+_\beta(0)|N^*\right\rangle$ is the hadron current part. The hadron current operator J^+_β contains a vector part V_β and axial vector part A_β:

$$J^+_\beta = V_\beta - A_\beta = 2MF_\beta = 2M(F^V_\beta - F^A_\beta) \tag{3.4}$$

Now the matrix elements are:

$$T(\nu_\mu N \longrightarrow \mu N^*) = -4GME_\nu \left\{ \sqrt{\frac{Q^2}{|\boldsymbol{q}|^2}} \langle N|\mu F_- - \nu F_+|N^*\rangle + \frac{M_N}{N}\sqrt{2\mu\nu}\,\langle N|F_0|N^*\rangle \right\} \tag{3.5}$$

with

$$F_+ = e_R^\mu F_\mu = -\frac{1}{\sqrt{2}}(F_x + iF_y) \tag{3.6}$$

$$F_- = e_L^\mu F_\mu = \frac{1}{\sqrt{2}}(F_x - iF_y) \tag{3.7}$$

$$F_0 = \sqrt{\frac{Q^2}{Q^{*2}}} e_S^\mu F_\mu = F_t + \frac{\nu^*}{Q^*} F_z \tag{3.8}$$

And the differential cross-section is

$$\frac{d\sigma}{dQ^2 dW^2} = \frac{G^2}{8\pi^2 M_N} \kappa \frac{Q^2}{|\boldsymbol{q}|^2} \left[\mu^2 \sigma_L + \nu^2 \sigma_R + 2\mu\nu\sigma_S\right] \tag{3.9}$$

with

$$\sigma_{L,R} = \frac{\pi M}{2M_N} \frac{1}{\kappa} \sum_{j_z} |\langle N, j_z \mp 1 | F_\mp | N^*, j_z \rangle|^2 \delta(W - M) \tag{3.10}$$

$$\sigma_{L,R} = \frac{\pi M}{2M_N} \frac{1}{\kappa} \frac{|\boldsymbol{q}|^2}{Q^2} \sum_{j_z} |\langle N, j_z | F_0 | N^*, j_z \rangle|^2 \delta(W - M) \tag{3.11}$$

and the flux factor

$$\kappa = \frac{W^2 - M_N^2}{2M_N} \tag{3.12}$$

The original RS model for RES assumes zero lepton mass. It shows some disagreement with the pion production data, especially in the low Q^2 region. The non-zero lepton mass effect was later introduced by Berger and Sehgal [21].

Resonance interaction plays an important role in neutrino oscillation experiments. As already discussed in chapter 1, RES is a large contribution to neutrino oscillation measurement in oscillation energy at few-GeV level. Although neutrino oscillation experiments use both a near and far detector to measure interactions before and after oscillation which reduces uncertainties from cross-sections, those uncertainties can not be completely cancelled due to differences in detector efficiencies, flux and interactions between these two detector. The cross-section knowledge of RES therefore is very important for oscillation measurement, especially at few-GeV level. Moreover, π^0s from resonance also make background to ν_e appearance measurement.

Historically, resonance pion production was measured by old bubble chamber experiments. There were large uncertainties due to lack of statistics. Figure 2.2 shows some historical measurement of 3 charged current resonance interaction channels along with theoretical calculation by NUANCE neutrino generator. A good summary of previous RES single pion production measurement can be found in [22].

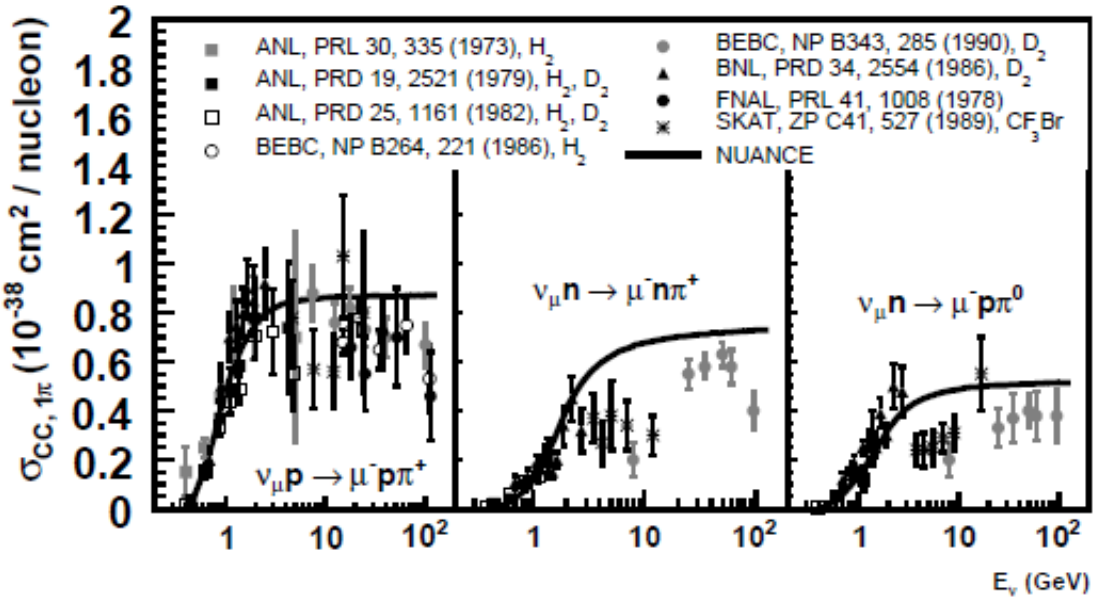

Figure 3.2 Historical measurement of resonance single pion production. The black line represents theoretical calculation using NUANCE using MA = 1.1 GeV [23]. (Plot taken from [22])

3.2 Introduction to NOMAD

The **N**eutrino **O**scillation **MA**gnetic **D**etector (NOMAD, WA-96) was designed to search for ν_μ to ν_τ oscillations in the CERN SPS wide band neutrino beam. The neutrino beam was produced by the 450 GeV protons from the Super Proton Synchrotron (SPS) incident on a beryllium target.The positively charged secondary π, K mesons were focused by two magnetic horns into a 290 m long evacuated decay pipe and then decayed into neutrinos.

The NOMAD detector was composed of several sub-detectors [26]. The target consisted of 132 planes of $3 \times 3m^2$ drift chamber (DC), with a 2.7 ton fiducial mass composed primarily of carbon (64%), oxygen (22%), nitrogen (6%), and hydrogen (5%). The measured composition of the target was 52.43% protons and 47.57% neutrons. The average density of $0.1gm/cm^3$ is similar to that of liquid hydrogen, and the effective atomic number of 12.8 is similar to carbon [30]. Following the drift chambers are a Transition Radiation Detector (TRD), a pre-shower detector (PRS) and a lead-glass electromagnetic calorimeter (ECAL). The ensemble of DC, TRD, and PRS/ECAL was placed within a dipole magnet providing a 0.4 T magnetic field orthogonal to the neutrino beam line, which makes high precision momentum measurement of charged particles possible.

During its run, the NOMAD experiment recorded over 1.7 million neutrino interactions in its active drift-chamber target. This high resolution neutrino data sample offers an unprecedented opportunity to study a large number of neutrino interactions in addition to the neutrino oscillation search. The NOMAD ν_ν flux energy spans from few-GeV up to 300 GeV, with a mean energy of 24.3 GeV, which covers the neutrino oscillation energy range of many modern and next generation ν_e appearance experiments such as NOνA and LBNE. The neutrino cross-section measurement from NOMAD therefore can play an important role in current and future ν_e appearance search.

3.3 Monte Carlo Simulation

NOMAD uses NEGLIB, built based upon LEPTO 6.1 [27] and JETSET [28], as its standard neutrino event generator. We also used GENIE, a relatively modern neutrino generator to achieve better agreement with data. RS model is used for RES simulation [24]. A GEANT program was used to simulate the NOMAD detector response [29]. All major interaction types are simulated. For this analysis, the

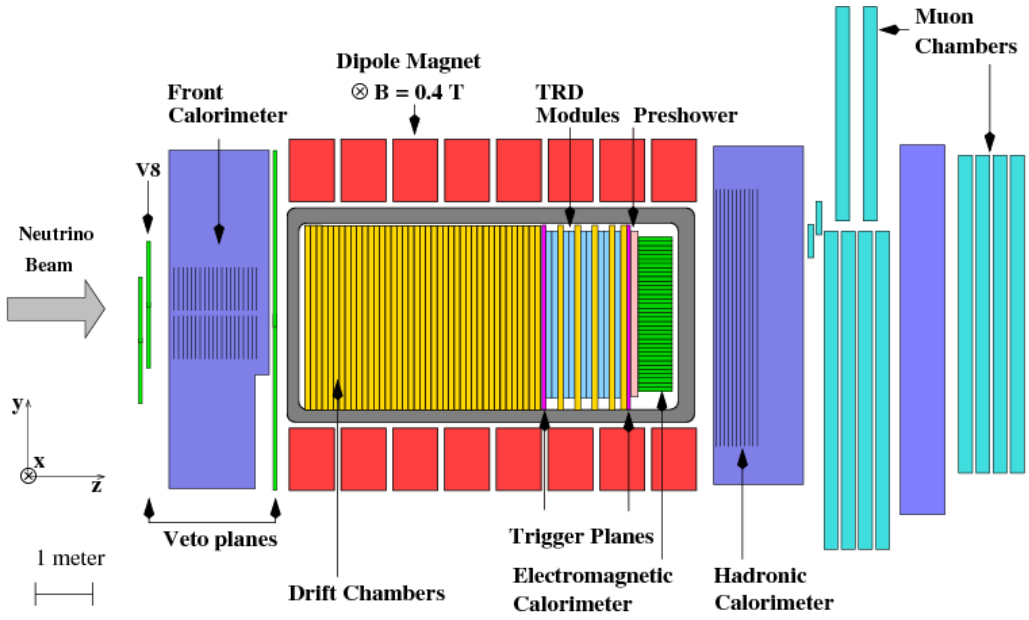

Figure 3.3 The NOMAD detector.

sample of MC events includes 50K RES. 1.35M CCDIS, 36K QE, 8K NCDIS and 7K COH. The total number of CC events is about 1.36M based on inclusive CC measurement [25] and the relative abundance of DIS:RES:QE was taken to be approximately 1.0:0.035:0.024.

One issue with the RES simulation is the value of axial-mass (MA). We take the default value in GENIE to be 1.12 in the standard simulation and analysis. We also vary it by $\pm$ 20% to evalute systematic error from MA uncertainty. Moreover, the analysis can be a measurement of MA itself by comparing Data/MC agreement using simulation with different MA values. The GENIE calculated cross-section of RES with different MA values are shown in figure 2.4.

3.4 Signal and Background

We first focus on the first channel of RES interaction, in which a proton and a π^+ are produced: $\nu_\mu + p \longrightarrow \mu p \pi^+$. It is dominated by Δ^{++} production. In NOMAD detector, the signal events have 3 tracks: one negative muon track, and two positive

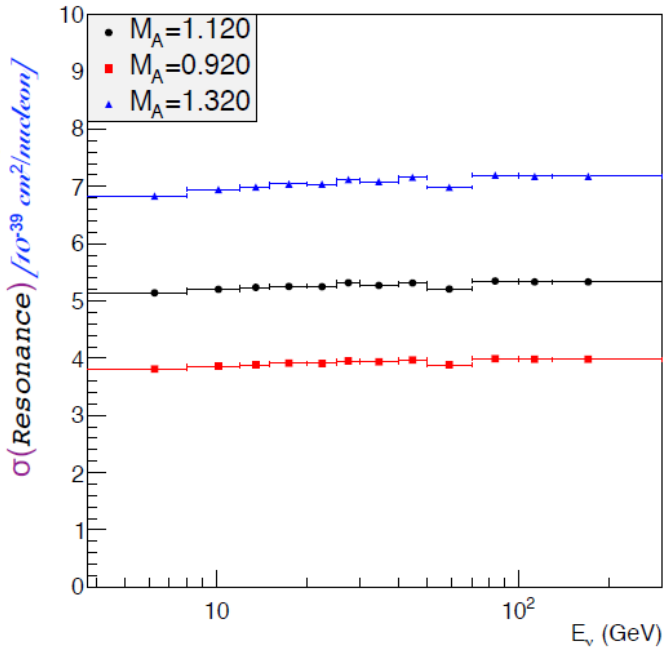

Figure 3.4 Genie calculated cross-section of RES interaction with different MA values as a function of neutrino energy. The default MA value in GENIE is 1.12 GeV (black). Variations of 0.92 GeV (blue) and 1.32 GeV (red) are also shown.

tracks from proton and π^+, with little others. Fig 2.5 show a candidate event in NOMAD detector. One long negative track (curving downward) and two positive tracks (curving upward) can be seen in the eventdisplay.

Another type of RES event we consider are 2-track events, including a negative muon track and a positive hadron track. They may from the decay of Δ^+ decay: $\Delta^+ \longrightarrow n\pi^+$, $\Delta^+ \longrightarrow p\pi^0$, or a Δ^{++} decay where one of the hadron track is missing.

The 2 channels (3-track and 2-track) will be measured separately, presented in section 3.5 and section 3.6. Then section 3.7 will present a combined measurement of inclusive resonance interaction.

The major background for RES are from charged-current Deep-Inelastic scattering (CCDIS). In a DIS event, a neutrino scatters off a quark in the nucleon via the exchange of a virtual W or Z boson, producing a lepton and a hadron shower in the final state. There can be 2 positive tracks of π^+ or proton in the hadron shower

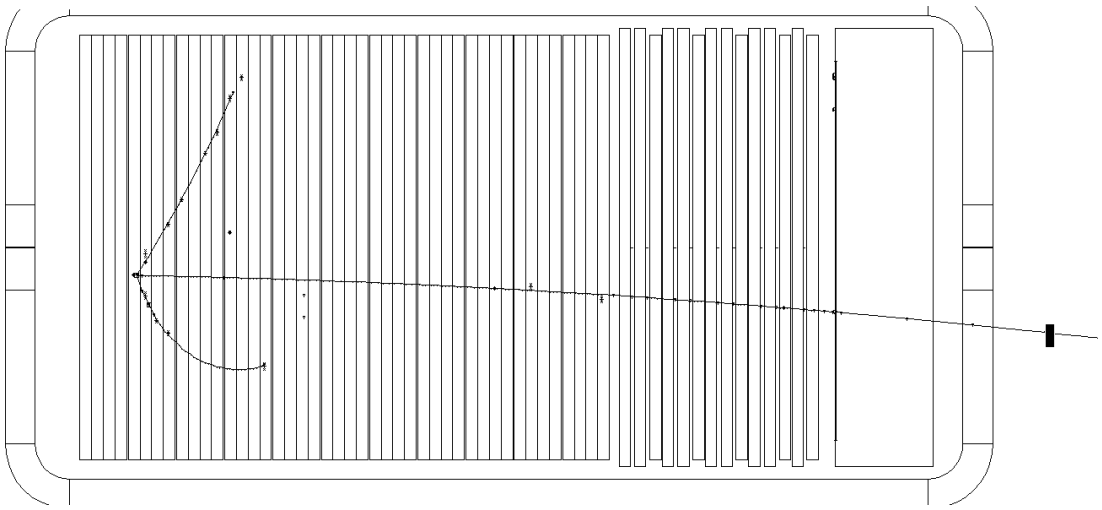

Figure 3.5 A Δ^{++} candidate event in NOMAD detector. One long negative track (curving downward) and two positive tracks (curving upward) can be seen in the eventdisplay.

besides the muon track, which mimic a 3 track RES signal. Other interactions, such as QE and COH, is much smaller in number compared to DIS in 3-track sample, but may produce backgrounds to track measurement.

To separate signal from background, we first look at kinematic variable distributions and apply selection cuts. Then neural networks are trained using MC for further separation.

3.5 Neural Network

Artificial neural networks (ANN or just NN) are widely used in physics data analysis [31]. A neural network has at least 3 layers: input layer, hidden layer and output layer. Each of the layers has one or more neutrons. Different Layers are connected by bias and weighted links between them.

1. Input layer. The neurons in a input layer are used to take the inputs. The inputs are forwarded to the first hidden layer after normalization.

2. Hidden layer. Each of the neutrons in a hidden layer takes a linear combination of the outputs of the previous layer and outputs a sigmoid function of that

combination. A sigmoid function is defined as

$$S(x) = \frac{1}{1 + e^{-x}}$$

There can be more than one hidden layers.

3. Output layer. The output of a output layer is simply a linear combination of the outputs of the previous layer.

Any continuous function can be approximated by a linear combination of sigmoid functions. In physics analysis, a neural network are often designed to take a set of kinematic variables $(x_1, x_2...)$ as input and use a single output to indicate signal or background. $(f = f(x_1, x_2...))$ The NN should be trained and tested before being used in analysis.

A Monte Carlo sample consists of signal and background events is used in training, with an integer F defined to be 1 for the signal events and 0 for the background events. The training process tunes the weights of the connection between NN layers to minimize the error between the NN output f and the MC integer F (0 or 1). After the training, the NN is tested by an independent MC sample to make sure there is no over-training. The trained neural network is then a function of inputs with the output being the probability of signal against background.

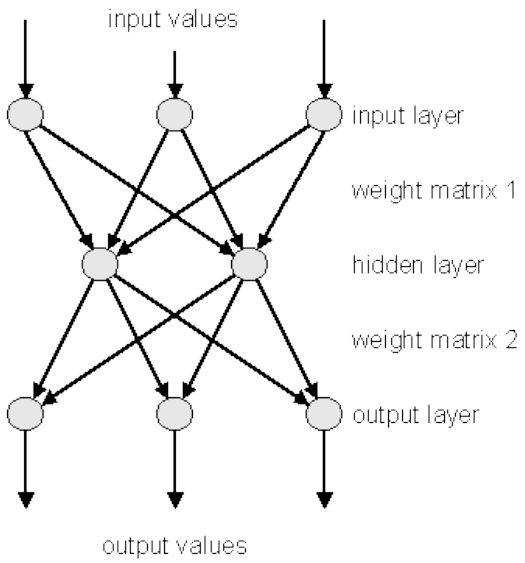

Figure 3.6 An example of the structure of an artificial neural network. Three layers are shown in this case: input layer (3 neurons), hidden layer (2 neurons) and output layer (3 neurons). Neurons of nearby layers are connected by weighted links. The number of layers and neurons can be customized for different analysis purpose. Picture taken from [31].

3.6 3-Track Analysis

This section presents details of the analysis of the 3-track sample. We are looking for RES events with 3 tracks : muon, proton and π^+. Major background is from CC-DIS with 2 positive tracks from hadron shower. We first look at differences between RES and CC-DIS in kinematic variables, upon which selection cuts are developed. Then a neural network is trained using RES and DIS MC events surviving the cuts. We see a good separation between signal and background in the NN output. Then the background is normalized, and finally a corrected number of signal is measured. We do the analysis in 14 neutrino energy bins, with a fixed background normalization factor used for all bins.

Events Selection

We first apply pre-selection cuts, including the fiducial cut, requiring negative track identified as muon with 2 additional positive hadron track, and veto all photons to select the 3-track events. A shape comparison of kinematics between RES and DIS is made using the 3-track MC events selected, including missing P_T, total hadron energy P_{Had} and hadron angle from incoming neutrino θ_{Had} (figure 2.7). Differences between RES and DIS can be seen. DIS tends to have more energy transfer and thus the hadron shower show higher energy and smaller angle from incoming neutrino direction. DIS also has higher missing P_t.

Based upon those comparison, we choose the cut on $p_{had} < 2.5$, $P_t^m < 0.7$ and $\theta_{had} > 0.35$. The number of events passing each cut are shown in table 2.1. The events selected are then subject to the neural network analysis.

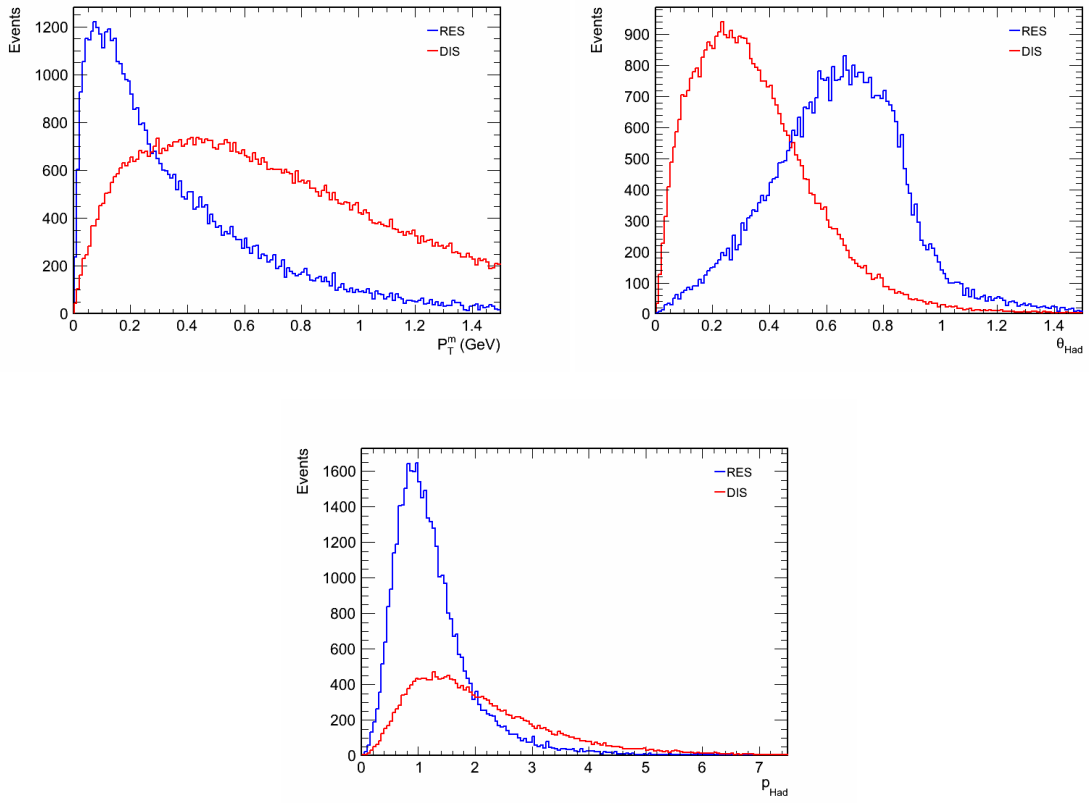

Figure 3.7 Shape comparison of kinematic variables between 3-track RES (blue) and DIS (red) MC, including missing P_t, θ_{Had} and P_{had}.

Table 3.1 Cut table of 3-track analysis.

Cuts	QE	RES	CCDIS	NCDIS	COH	TOT-Bac	MC	Data
3-track	727.5	9836.4	70962.5	4.4	18.0	71712.4	81548.8	29568.0
$P_t^m < 0.7$	497.6	8326.4	36172.3	1.1	16.0	36687.0	45013.5	19800.0
$\theta_{had} > 0.35$	491.0	7467.1	16917.0	0.2	6.8	17415.0	24882.1	13982.0
$p_{had} < 2.5$	449.0	6999.2	12367.2	0.2	6.4	12822.8	19822.0	11992.0
Norm	271.6	4234.4	7482.0	0.1	3.9	7757.6	11992.0	11992.0

Neural Network

We use TMultiLayerPerceptron class in root to built neural networks [31]. The structure of NN is shown in Figure 2.6. The input layer has 9 input variables which are reconstructed 3-momentums (px, py, pz) of reconstructed muon, proton and pion tracks. It is followed by 3 hidden layers, with 9, 6 and 3 neurons respectively. The output is an integer defined as 1 for RES and 0 for DIS. A sample of RES (signal) and DIS (background) 3-track MC events are used as the training sample. The trained NN is then tested by an independent sample of RES and DIS MC events to make sure there is no over-training. NN successfully separates RES signal from DIS background as shown in Figure 2.9.

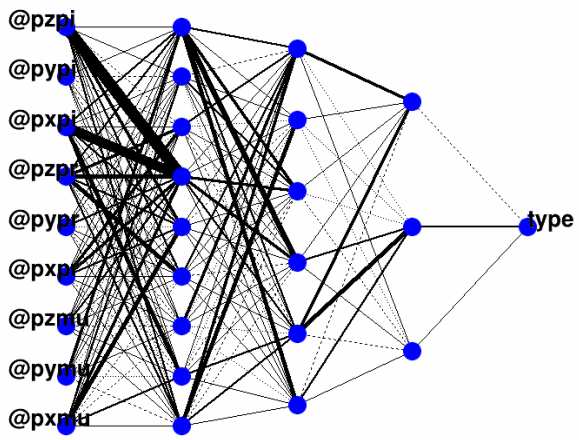

Figure 3.8 The stucture of NN built for 3-track resonance analysis. 5 layers are used, with 1 input layer, 3 hidden layer, and 1 output layer. The number of neutrons are 9:9:6:3:1 respectively.

We then define signal region and background region based upon NN output distribution. Signal region defined as NN output greater than 0.4 where RES events dominate and background region is defined as NN output smaller than 0.4 where the dominate is DIS. The signal efficiency is 75% compared to the background efficiency of 32%. Next we can normalize the background to fit data.

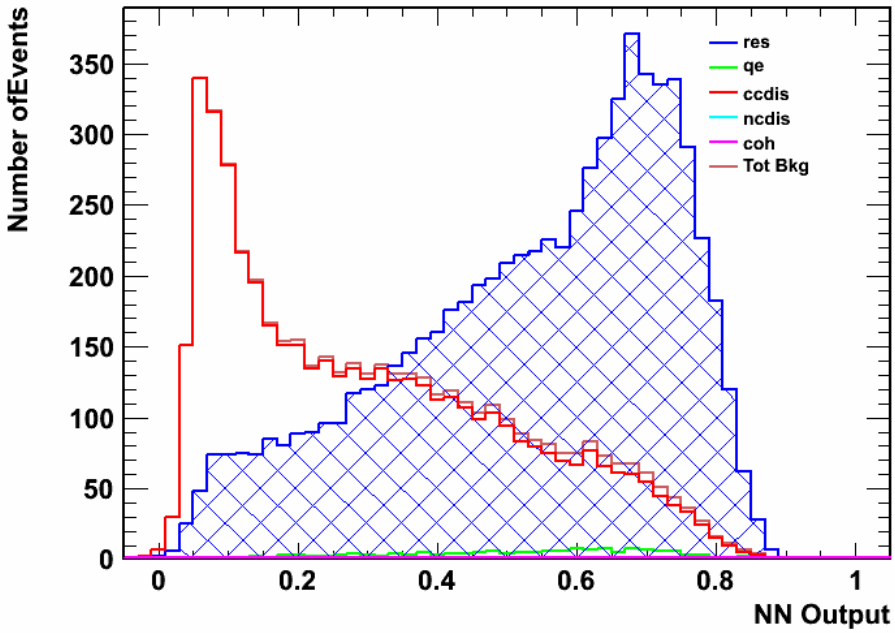

Figure 3.9 The NN output of RES (blue) and DIS (red) 3 track MC sample. No normalization is applied.

Background Normalization

The normalization process works as the following. First assume there is no signal in background region. A zero order background normalization factor ($BN(0)$) is calculated as the ratio of data events (D_b) to background events (B_b), both in background region ($BN(0) = D_b/B_b$). Then this background normalization factor is applied to background events in signal region (B_s), and a number of raw signal S_{raw} is defined as data events in signal region (D_s) subtract normalized background events ($S_{raw} = D_s - B_b * BN(0)$). This is the first order calculation. A signal normalization factor (SN) can be calculated as the ratio of raw signal to the original signal events in signal region ($SN = S_{raw}/S_s$), and then be applied to signal events in background region (S_b), to get a first-order background normalization factor calculated as

$BN(1) = \dfrac{D_b - SN * S_b}{B_b}$. And we can re-write it as a function of BN(0):

$$BN(1) = \frac{D_b - \dfrac{D_s - B_b * BN(0)}{S_s} * S_b}{B_b} = \frac{D_b - D_s \dfrac{S_b}{S_s}}{B_b} + \frac{B_s}{B_b} * \frac{S_b}{S_s} * BN(0) \qquad (3.13)$$

Note that $\dfrac{B_s}{B_b} \ll 1$ and $\dfrac{S_b}{S_s} \ll 1$, given good separation of signal and background by NN. Similarly we calculate $BN(2)$ as a function as $BN(1)$ and so a function of $BN(0)$, and then $BN(3)$ ... $BN(N)$ until it converge. This will be the best fit. Figure 2.10 shows the NN output of MC after normalization compared against data. The MC fits data very well.

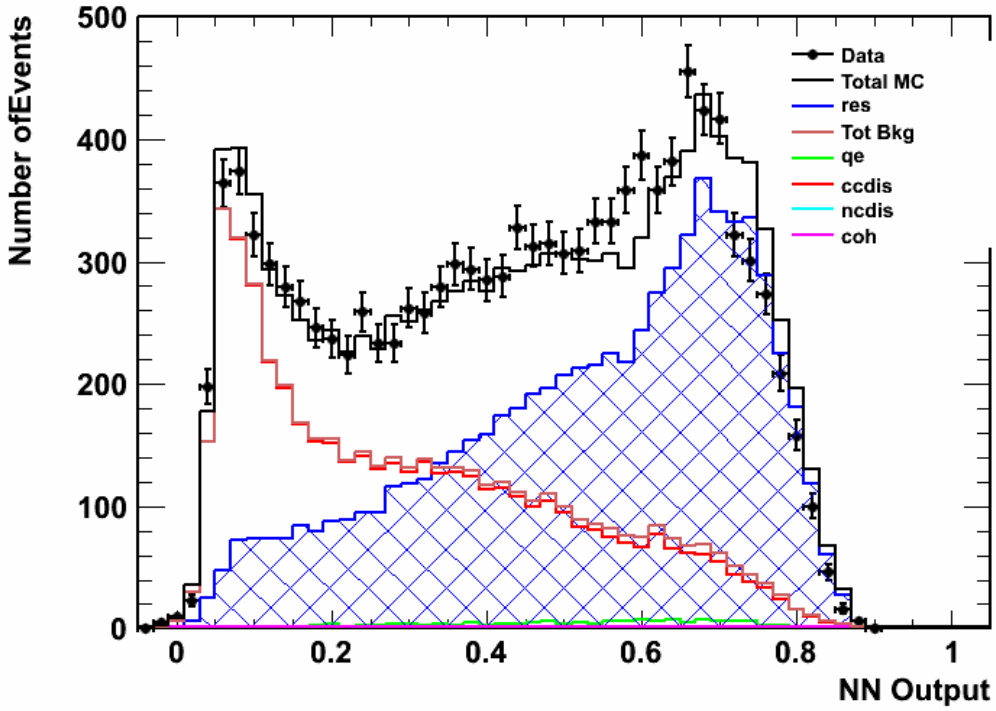

Figure 3.10 NN output of RES (blue) and DIS (red) 3 track MC events after normalization, compared against data (black dots).

Table 3.2 3-track analysis in 14 neutrino energy bins.

E_ν(GeV)	$\langle E \rangle$ (GeV)	TotBkg	BN	NormBkg	Data	RawSig	Eff	CorrSig
2.5∼ 6	4.6	74.5	1.089	81.11	256	174.9	0.09021	1607
6∼ 8	7.1	103.4	1.089	112.6	375	262.4	0.1027	2391
8∼ 10	9	121.8	1.089	132.6	580	447.4	0.105	3807
10∼ 12	11	127.2	1.089	138.5	593	454.5	0.1093	4151
12∼ 15	13.5	186.7	1.089	203.2	892	688.8	0.1084	6002
15∼ 20	17.3	237.2	1.089	258.3	1226	967.7	0.1084	8648
20∼ 25	22.3	164.6	1.089	179.2	845	665.8	0.105	6220
25∼ 30	27.4	108.7	1.089	118.3	549	430.7	0.1064	3964
30∼ 40	34.3	121.8	1.089	132.6	638	505.4	0.104	4629
40∼ 50	44.5	58.12	1.089	63.27	300	236.7	0.1076	2097
50∼ 70	58.6	59.67	1.089	64.96	291	226	0.1011	2124
70∼100	83.1	42.77	1.089	46.56	208	161.4	0.1092	1464
100∼130	112.8	22.28	1.089	24.25	87	62.75	0.09704	573.9
130∼200	154.4	13.61	1.089	14.82	38	23.18	0.1031	222.6
sum	25	1442	1.089	1570	6878	5308	0.1048	48308

Signal Measurement

The raw signal events is then calculated as the data events subtract normalized background events. We do it in 14 reconstructed neutrino energy bins. A efficiency (Eff) is calculated as the ratio of RES MC in signal region (S_s) divided by total generated RES MC (S_{gen}) in each bin. Then the corrected signal is $S_{corr} = S_{raw}/Eff$. The numbers are subject to isoscalar correction. In this way a total number of $48,308 \pm 1004(stat)$ corrected RES signal events is measured. The numbers of events in each reconstructed neutrino energy bins are converted to true neutrino energy bins using a smearing matrix calculated from RES MC. The detailed corrected signal calculation in each neutrino energy bin as well as the cumulative result is shown in table 2.2.

Comparisons of kinematic variables in signal region are made after normalization, including Bjorken scaling variables x_{bj} and y_{bj}, Q^2, momentums of muons and hadrons P_μ, P_{pr} and P_π. They all show good agreement between MC and data (figure 2.16). An invariant mass is reconstructed using 4-momentum of proton track and pion track. A clear peak of signal Δ^{++} mass is seen in figure 2.12. MC describes hadronic

Table 3.3 Cut table of 2-track analysis.

Cuts	QE	RES	CCDIS	NCDIS	COH	TOT-Bac	MC	Data
2-track	11736.2	18212.3	73774.8	3.1	4044.8	89558.9	107771.3	46391.0
θ^{μ}_{Had}	4000.5	12767.7	47978.3	0.9	1609.2	53588.9	66356.5	27707.0
Q^2	2042.5	9730.9	17084.5	0.7	1572.0	20699.8	30430.7	15817.0
Norm	1061.6	5057.9	8880.0	0.4	817.1	10759.1	15817.0	15817.0

system very well.

3.7 2-track Analysis

A similar neutral network analysis is performed for 2-track events. The procedure is similar to 3 track analysis, including event selection, neural network analysis, background normalization and signal measurement, which will be presented in the following subsections.

Selection

The preselection is the same as 3-track, except that we require one positive track besides the muon track instead of two. we get significant background contribution from QE and COH as well as DIS. Selection cuts are chosen to be $0.35 < \theta^{\mu}_{Had} < 1.0$ and $Q^2 < 1$ to reduce backgrounds. The number of events passing each cut are shown in the cut table 2.3.

Neural Network

A neural network is trained to separate RES from DIS using 2-track. It takes 9 variables as input, including x_{bj}, y_{bj}, Q^2 and the 3-momentums of muon and hadron track. There are 2 hidden layers, with 6 and 3 neurons respectively, and the single output is a likelihood indicating signal or background. The distribution of NN output of MC are shown in figure 2.14.

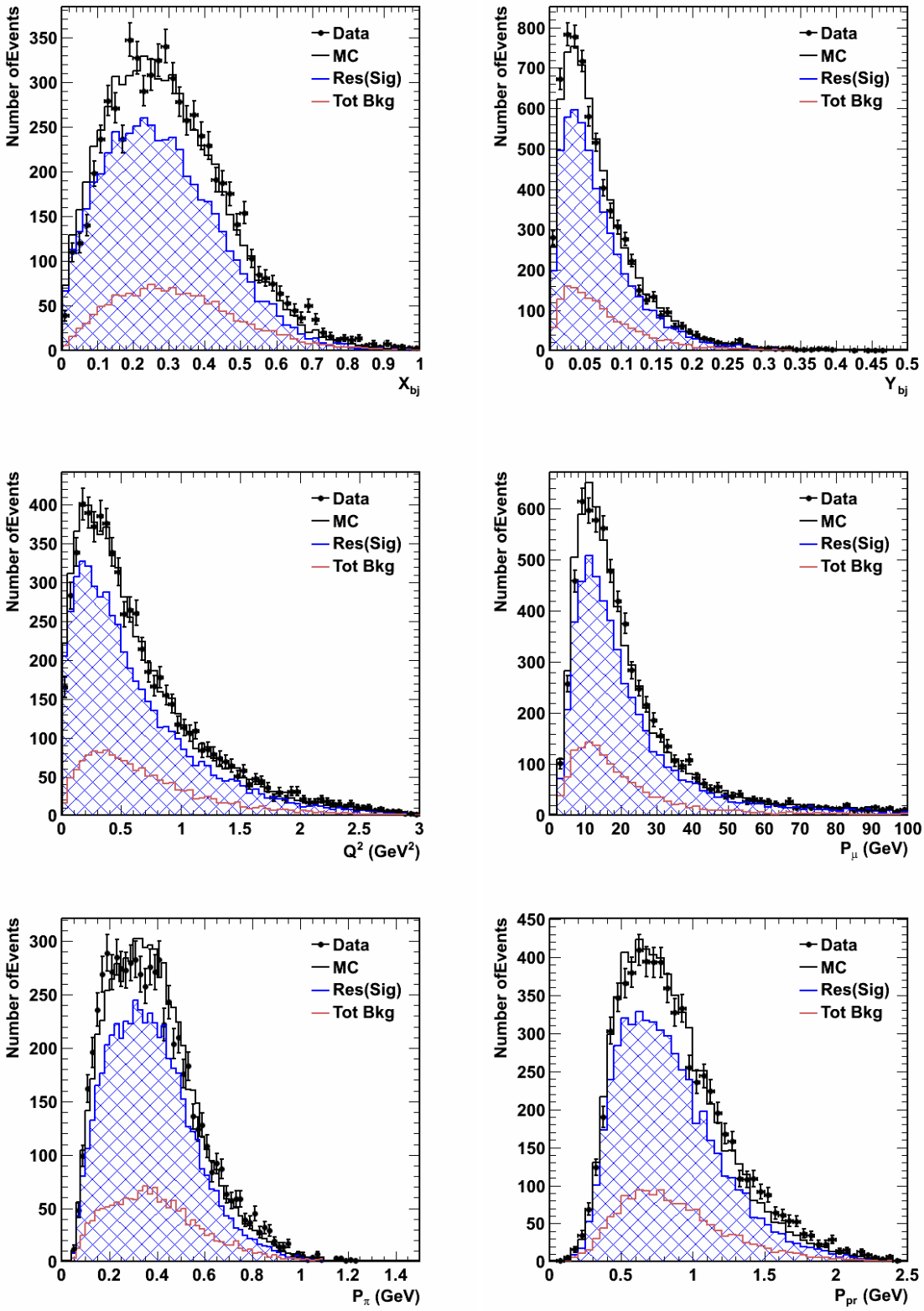

Figure 3.11 Kinematics variables of RES (blue) and DIS (red) MC with normalization in 3-track analysis compared against data (black dots). From top left to bottom right are x_{bj}, y_{bj}, Q^2, P_μ, P_π and P_{pr}.

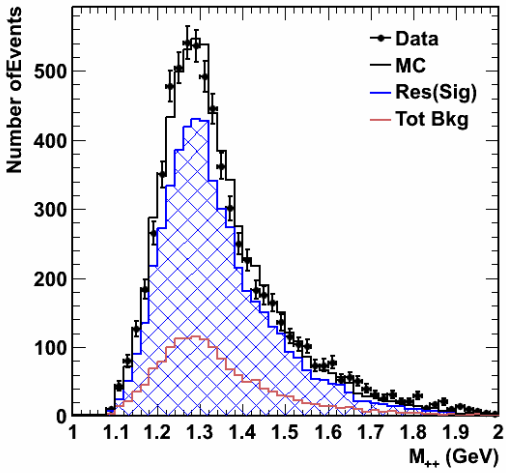

Figure 3.12 Reconstructed invariant mass of two hadron tracks in 3-track analysis. RES (blue), DIS (red), total MC (black line) and data (black symbols) are shown. The plot show a peak around Δ^{++} mass.

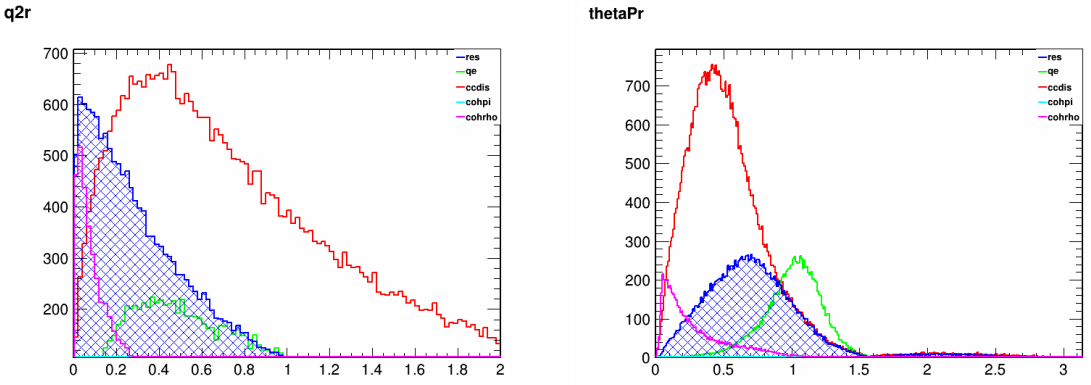

Figure 3.13 Shape comparison of kinematic variables between 3-track RES (blue), DIS (red), QE (green) and COH (purple) MC, including Q^2 and θ_{had}.

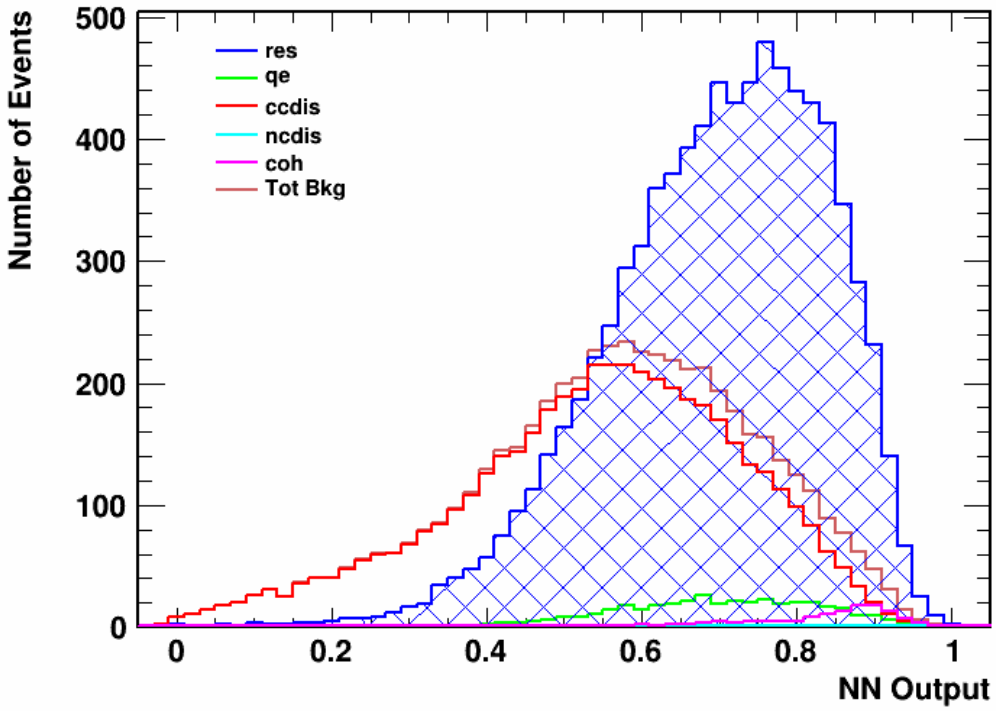

Figure 3.14 NN output of MC, without normalization.

Signal region is defined as NN output greater than 0.4 and background region is defined as NN output smaller than 0.4, same as in 3-track analysis.

Background Normalization

The same normalization method described in previous section is applied to 2-track analysis. The normalization result is shown in 2.15 with almost prefect agreement between data and MC.

Signal measurement

Table 2.4 shows 2 track signal measurement result. It is done in 14 neutrino energy bins same as used in 3-track analysis. A smearing matrix is used to convert events

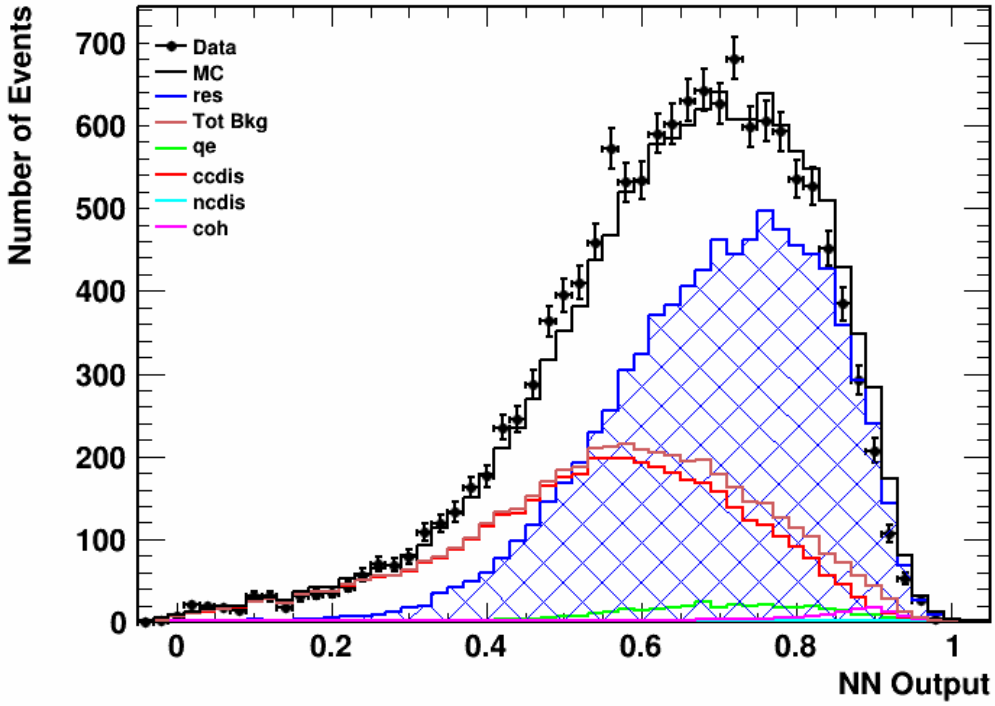

Figure 3.15 NN output of RES (blue) and DIS (red) 2 track MC events after normalization, compared against data (black dots).

in reconstructed neutrino energy bins to true neutrino energy bins. The numbers are subject to isoscalar correction. The total number of corrected signal is $51,693 \pm 1521(stat)$.

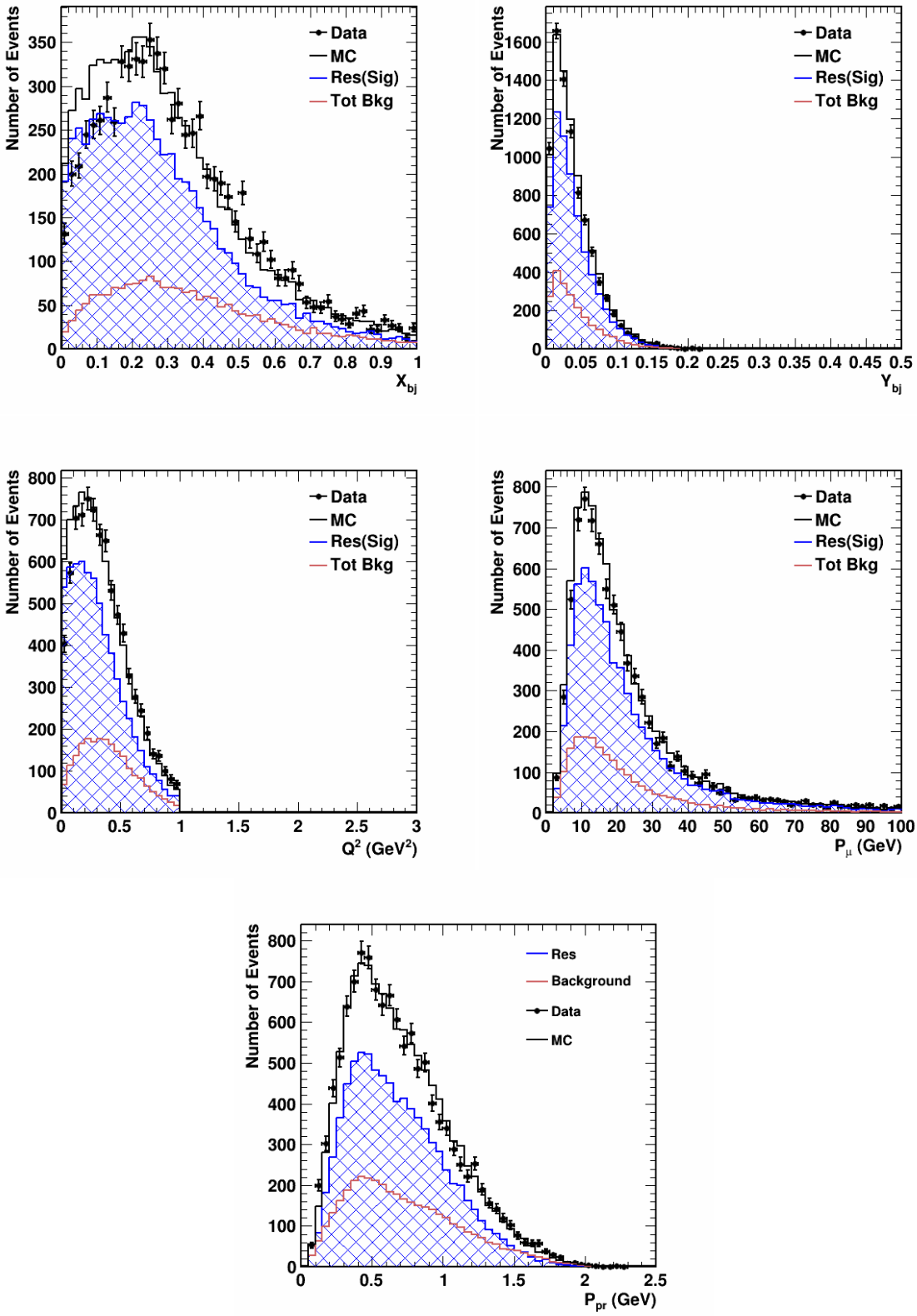

Figure 3.16 Kinematics variables of RES (blue) and DIS (red) MC with normalization in 2-track analysis compared against data (black dots). From top left to bottom right: x_{bj}, y_{bj}, Q^2, P_μ, P_{pr}.

Table 3.4 2 track analysis in 14 neutrino energy bins.

$E_\nu(GeV)$	$\langle E \rangle$ (GeV)	TotBkg	BN	NormBkg	Data	RawSig	Eff	CorrSig
2.5∼ 6	4.6	250.7	0.9207	230.8	452	221.2	0.1372	1199
6∼ 8	7.1	314.7	0.9207	289.8	757	467.2	0.1595	2499
8∼ 10	9	377.8	0.9207	347.9	1020	672.1	0.1593	4017
10∼ 12	11	378.7	0.9207	348.7	1147	798.3	0.1609	4854
12∼ 15	13.5	547	0.9207	503.6	1582	1078	0.1632	6790
15∼ 20	17.3	686.5	0.9207	632.1	2086	1454	0.1606	9438
20∼ 25	22.3	469.5	0.9207	432.3	1464	1032	0.1637	6588
25∼ 30	27.4	308.5	0.9207	284	988	704	0.1654	4357
30∼ 40	34.3	350.5	0.9207	322.7	996	673.3	0.1635	4350
40∼ 50	44.5	186.3	0.9207	171.5	548	376.5	0.1717	2215
50∼ 70	58.6	181.3	0.9207	166.9	510	343.1	0.1718	2048
70∼100	83.1	127.5	0.9207	117.4	390	272.6	0.1646	1662
100∼130	112.8	58.1	0.9207	53.49	179	125.5	0.1783	718.1
130∼200	154.4	37.91	0.9207	34.91	127	92.09	0.1715	493.9
sum	25	4275	0.9207	3936	12246	8310	0.161	51693

3.8 Result

The goal of this analysis is the inclusive RES cross-section (σ_{RES}). It is calculated as the number of corrected RES signal events divided by the NOMAD flux, which are taken from [25]. The result is also reported here as the ratio of RES with respect to inclusive ν_μ-CC, times neutrino energy ($R_{RES} = \sigma_{RES}/\sigma_{CC} \times E_\nu$). The advantage of presenting the ratio is the fact that it would be independent of flux measurement.

The ratio and cross-section are first calculated in 14 neutrino energy bins using 3-track and 2-track measurement separately, shown in figure 2.17 and 2.18. The 3-track and 2-track measurement show good agreement, with some opposite trend, especially in high energy region. This is understandable, as some Δ^{++} decays enters either 3-track, or 2-track when one hadron track is missing.

Adding up 3-track and 2-track analysis we get a combined result of inclusive RES measurement. The combined analysis not only increases statistics, but also reduces some systematic errors. The corrected signal in 14 neutrino energy bins are presented in table 2.5. The cross-sections and ratios calculated from 3-track, 2-track and the combined analysis are shown in figure 2.17 and 2.18, with statistic error bars.

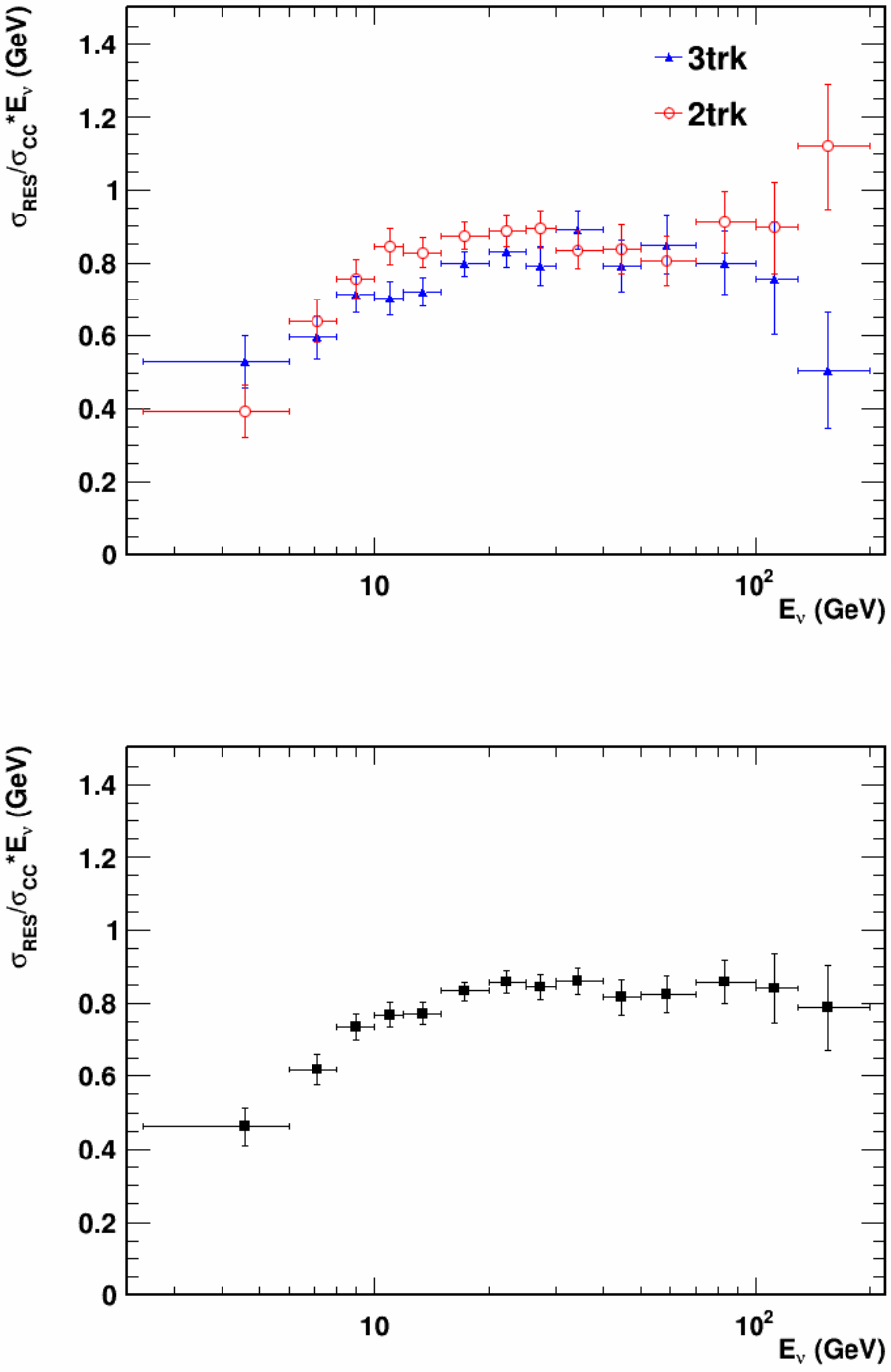

Figure 3.17 Ratio of fully-corrected RES signal with respect to inclusive CC events. The top plot shows measurement from 3-track analysis (blue) and 2-track analysis (red). The bottom plot shows the result of combined analysis.

Table 3.5 Corrected signal events and statistic errors from 3-track, 2-track and combined analysis.

E_ν (GeV)	$\langle E \rangle$(GeV)	3trk	3trkErr	2trk	2trkErr	Combine	Err
2.5∼ 6	4.6	1530	207.9	1140	208	1335	147
6∼ 8	7.1	2216	220.3	2385	222.5	2300	156.5
8∼ 10	9	3610	255.9	3825	261.8	3715	183
10∼ 12	11	3836	249.2	4617	268.6	4197	182.7
12∼ 15	13.5	5644	309.4	6483	326.7	6041	224.6
15∼ 20	17.3	8296	361.8	9092	388.6	8665	264.8
20∼ 25	22.3	5862	308	6251	303	6060	216
25∼ 30	27.4	3651	243.9	4120	236.1	3893	169.6
30∼ 40	34.3	4412	268.4	4140	247.5	4265	182
40∼ 50	44.5	1964	176.9	2074	166.5	2022	121.2
50∼ 70	58.6	2021	186.4	1915	161.5	1961	122.1
70∼100	83.1	1355	145.7	1547	143.3	1452	102.2
100∼130	112.8	535.7	108.1	633.7	87.85	594.7	68.17
130∼200	154.4	222.6	69.82	493.9	75.71	347.3	51.32
sum	25	4.831e+04	1004	5.169e+04	1521	4.934e+04	838.2

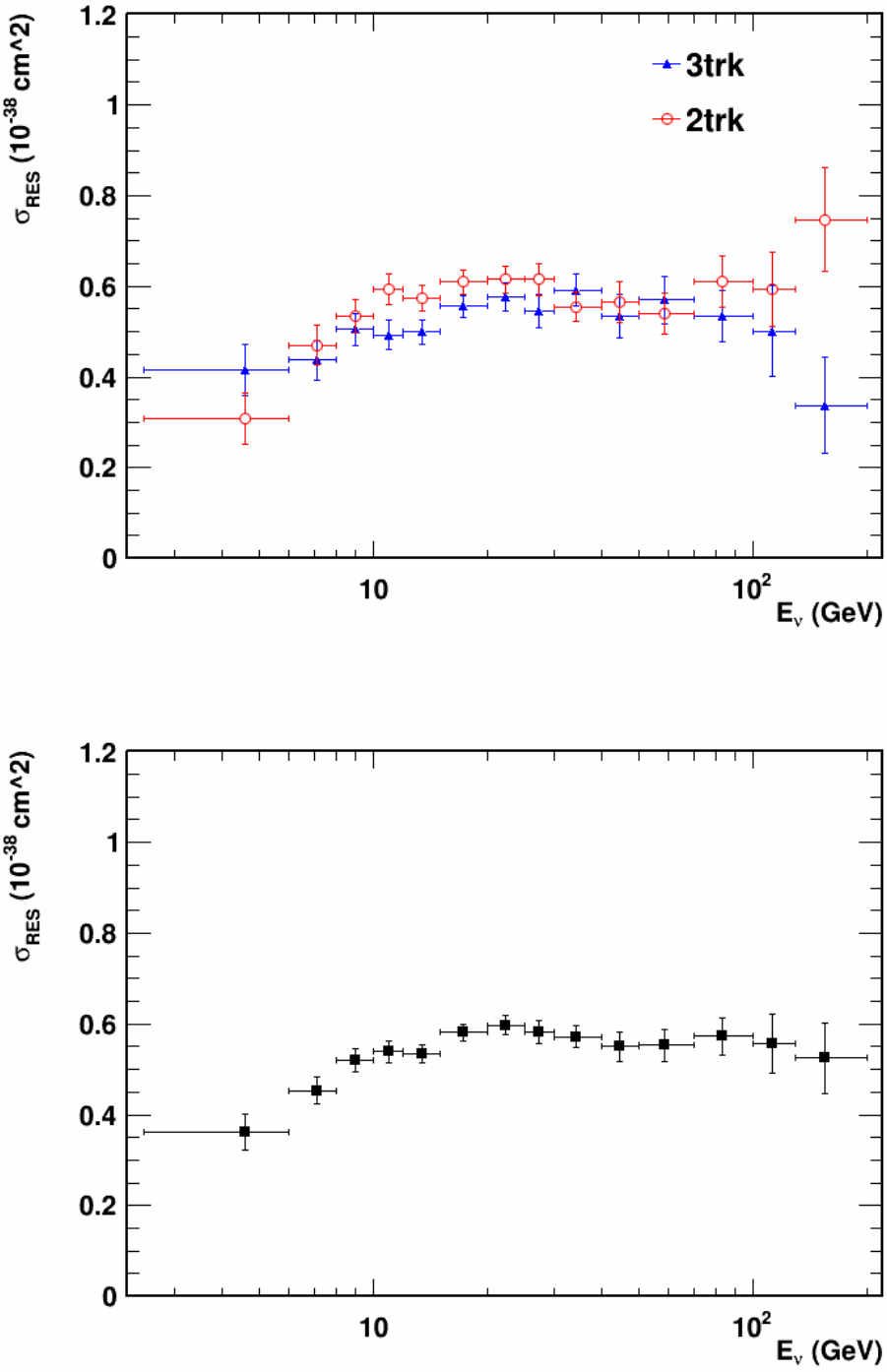

Figure 3.18 Cross-section of measured RES interaction. The top plot shows measurement from 3-track analysis (blue) and 2-track analysis (red). The bottom plot shows the result of combined analysis.

Table 3.6 Selection and NN cut variations for systematic uncertainties evaluation (3-track)

	Lower	Defualt	Higher
Cut1 (Missing P_t) (GeV)	0.67	0.70	0.73
Cut2 (θ_{Had}) (rad)	0.33	0.35	0.37
Cut3 (P_{had}) (GeV)	2.4	2.5	2.6
NN output	0.35	0.4	0.45

Table 3.7 Selection and NN cut variations for systematic uncertainties evaluation (2-track)

	Lower	Defualt	Higher
Cut1 (θ_{LH}) (rad)	0.34, 1.01	0.35, 1.00	0.36, 0.99
Cut2 (Q^2) (GeV^2)	0.97	1.0	1.03
NN output	0.35	0.4	0.45

3.9 Systematic Uncertainties

Systematic uncertainties of this analysis comes from two major sources. The first source is the selection of signal events, including the selection cuts and the cut on NN output defining signal region in the analysis. The second is the physics modelling of RES in MC simulations. Both of the uncertainties can be evaluated by varying the cuts and physics constant values in simulation.

1. Analysis selection cuts. To evaluate the systematic uncertainties from selection and NN cuts, we vary the cut value to approximately $\pm\sigma$ from the default. σ is defined as the resolution of certain kinematic variables. In this way we get two deviations from the central value of the measurement for each cut, and the uncertainty from that cut will be the average of the two. The variations of the selection cuts are shown in table 2.6 and 2.7. The systematic uncertainties are calculated as the percentage deviation from the central value, in 14 neutrino energy bins.

2. MC Modelling of RES. We consider the physics modelling of RES used in GENIE neutrino event generator. The uncertainties come from those physics constants which are not well defined, such as axial mass (MA), vector mass (MV), and mean free path (MFP). To evaluate the uncertainties, we vary MA by $\pm$20%, MV

Table 3.8 Physics modelling constant variations.

	Lower	Default	Higher
MA (GeV)	0.90	1.12	1.35
MV (GeV)	0.76	0.84	0.92
MFP	-20%	-	+20%

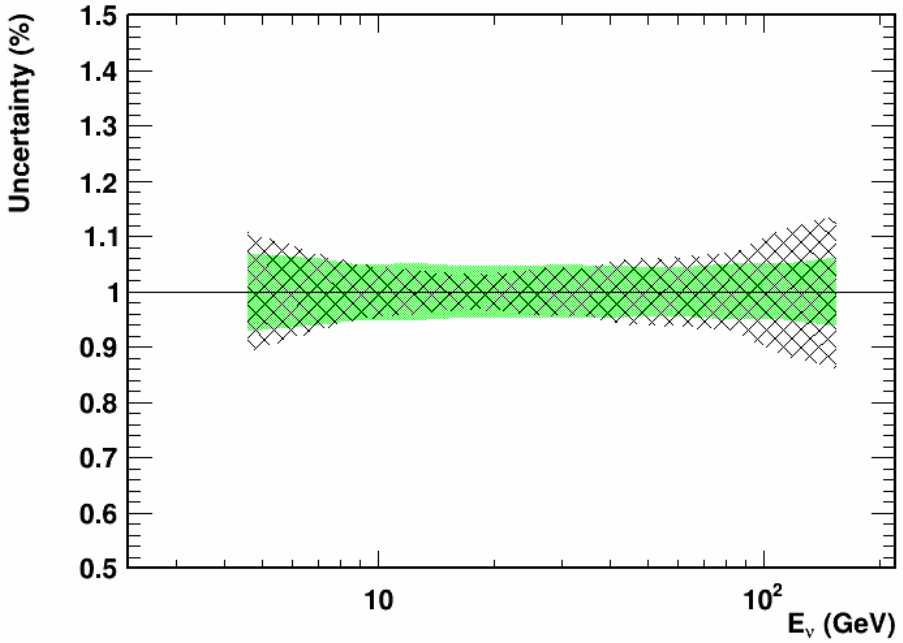

Figure 3.19 Statistic (hatch) and systematic (green) uncertainties in percentage.

by ±10%, and MFP by ±20% respectively in MC simulation according to GENIE documents [29]. The MC events are fed into the analysis, both 3-track and 2-track, and then the combined analysis. The systematic error is calculated as the percentage deviation from the central value, in 14 neutrino bins as shown in table.

The uncertainties from each source are taken as the average of the $+\sigma$ and $-\sigma$ deviation, listed in table 2.9 and 2.10. Finally, the total systematic uncertainties, along with statistic errors and central values of cross-section and ration of $\sigma_{RES}/\sigma_{CC} * E_\nu$, are plotted in figure 2.19, and the detained numbers are in table 2.11, 2.11 and 2.13.

Table 3.9 3-track systematic uncertainty contributions in 14 neutrino energy bins.

E_ν(GeV)	Cut1	Cut2	Cut3	MV	MA	MFP	Tot
2∼ 6	0.3	0.4	0.3	3.2	7.4	1.1	8.1
6∼ 8	1.0	0.2	0.5	2.2	5.6	2.3	6.6
8∼ 10	0.5	0.4	0.5	1.7	4.6	1.4	5.2
10∼ 12	0.5	0.4	0.2	2.1	4.9	2.1	5.8
12∼ 15	0.3	0.5	0.3	2.2	4.9	1.2	5.5
15∼ 20	0.1	0.2	0.0	1.8	4.4	1.7	5.1
20∼ 25	0.4	0.2	0.1	2.0	4.6	1.0	5.1
25∼ 30	0.2	0.1	0.4	1.8	4.4	2.5	5.4
30∼ 40	0.3	0.6	0.4	2.3	4.5	1.1	5.2
40∼ 50	0.7	0.3	0.9	1.6	3.6	2.2	4.7
50∼ 70	0.3	1.1	0.4	1.8	4.0	1.4	4.7
70∼100	0.7	0.9	0.5	2.4	4.5	1.6	5.5
100∼130	0.7	1.0	0.5	2.5	5.0	1.4	5.9
130∼200	1.4	2.0	1.0	3.2	6.1	1.7	7.6
Cumulative	0.1	0.2	0.1	2.0	4.7	1.6	5.4

Table 3.10 2-track systematic uncertainty contributions in 14 neutrino energy bins.

E_ν(GeV)	Cut1	Cut2	MV	MA	MFP	Tot
2∼ 6	2.4	0.6	6.2	12.6	0.9	14.3
6∼ 8	0.8	0.4	5.7	10.9	0.5	12.4
8∼ 10	0.9	0.8	5.4	10.6	0.9	12.0
10∼ 12	0.9	0.1	5.3	10.3	0.2	11.6
12∼ 15	0.7	0.1	5.2	10.1	0.6	11.5
15∼ 20	0.4	0.4	5.1	9.9	0.4	11.2
20∼ 25	0.6	0.5	5.1	10.0	0.2	11.2
25∼ 30	1.1	1.1	5.0	9.4	0.3	10.8
30∼ 40	1.0	0.9	5.3	9.8	0.7	11.3
40∼ 50	2.2	0.5	4.7	8.6	1.1	10.2
50∼ 70	1.7	0.3	5.0	9.1	0.1	10.5
70∼100	0.9	0.0	4.7	8.6	0.3	9.9
100∼130	0.1	0.5	4.2	7.6	1.2	8.8
130∼200	2.2	1.8	4.3	7.8	0.9	9.4
Cumulative	0.7	0.3	5.2	9.9	0.4	11.2

Table 3.11 Ratio of RES with respect to inclusive CC and cross-section of RES from 3-track analysis as a function of neutrino energy. Statistic and systematic uncertainties are shown in percentage.

E_ν(GeV)	$\langle E \rangle$(GeV)	σ_{RES} ($10^{-38} cm^2$)	$\sigma_{RES}/\sigma_{CC} \times E_\nu$(GeV)	Stat.(%)	Syst.(%)
2.5∼ 6	4.6	0.416	0.529	13.6	8.1
6.0∼8.0	7.1	0.437	0.596	9.9	6.6
8.0∼10.0	9.0	0.506	0.713	7.1	5.2
10.0∼12.0	11.0	0.493	0.702	6.5	5.8
12.0∼15.0	13.5	0.500	0.721	5.5	5.5
15.0∼20.0	17.3	0.556	0.797	4.4	5.1
20.0∼25.0	22.3	0.577	0.831	5.3	5.1
25.0∼30.0	27.4	0.546	0.792	6.7	5.4
30.0∼40.0	34.3	0.592	0.890	6.1	5.2
40.0∼50.0	44.5	0.535	0.792	9.0	4.7
50.0∼70.0	58.6	0.570	0.850	9.2	4.7
70.0∼100.0	83.1	0.535	0.800	10.8	5.5
100.0∼130.0	112.8	0.502	0.758	20.2	5.9
130.0∼200.0	154.4	0.337	0.504	31.4	7.6
Cumulative	25.0	0.563	0.838	2.1	5.4

Table 3.12 Ratio of RES with respect to inclusive CC and cross-section of RES from 2-track analysis as a function of neutrino energy. Statistic and systematic uncertainties are shown in percentage.

E_ν(GeV)	$\langle E \rangle$(GeV)	σ_{RES} ($10^{-38} cm^2$)	$\sigma_{RES}/\sigma_{CC} \times E_\nu$(GeV)	Stat.(%)	Syst.(%)
2.5∼6.0	4.6	0.309	0.394	18.3	14.3
6.0∼8.0	7.1	0.471	0.641	9.3	12.4
8.0∼10.0	9.0	0.536	0.756	6.8	12.0
10.0∼12.0	11.0	0.593	0.845	5.8	11.6
12.0∼15.0	13.5	0.574	0.828	5.0	11.5
15.0∼20.0	17.3	0.610	0.874	4.3	11.2
20.0∼25.0	22.3	0.616	0.886	4.8	11.2
25.0∼30.0	27.4	0.616	0.894	5.7	10.8
30.0∼40.0	34.3	0.555	0.835	6.0	11.3
40.0∼50.0	44.5	0.564	0.837	8.0	10.2
50.0∼70.0	58.6	0.540	0.805	8.4	10.5
70.0∼100.0	83.1	0.610	0.913	9.3	9.9
100.0∼130.0	112.8	0.593	0.896	13.9	8.8
130.0∼200.0	154.4	0.748	1.119	15.3	9.4
Cumulative	25.0	0.603	0.897	2.9	11.2

Table 3.13 Ratio of RES with respect to inclusive CC and cross-section of RES from combined 3-track and 2-track analysis as a function of neutrino energy. Statistic and systematic uncertainties are shown in percentage.

E_ν(GeV)	$\langle E \rangle$(GeV)	σ_{RES} ($10^{-38} cm^2$)	$\sigma_{RES}/\sigma_{CC} \times E_\nu$(GeV)	Stat.(%)	Syst.(%)
2.5∼6.0	4.6	0.362	0.462	10.9	7.1
6.0∼8.0	7.1	0.454	0.618	6.8	5.8
8.0∼10.0	9.0	0.520	0.734	4.9	4.8
10.0∼12.0	11.0	0.539	0.768	4.3	5.2
12.0∼15.0	13.5	0.535	0.772	3.7	5.0
15.0∼20.0	17.3	0.581	0.833	3.1	4.6
20.0∼25.0	22.3	0.597	0.859	3.6	4.7
25.0∼30.0	27.4	0.582	0.845	4.3	4.8
30.0∼40.0	34.3	0.572	0.860	4.3	4.7
40.0∼50.0	44.5	0.550	0.816	6.0	4.3
50.0∼70.0	58.6	0.553	0.824	6.2	4.3
70.0∼100.0	83.1	0.573	0.857	7.0	4.8
100.0∼130.0	112.8	0.557	0.841	11.4	4.9
130.0∼200.0	154.4	0.526	0.787	13.8	5.9
Cumulative	25.0	0.575	0.856	1.7	4.8

3.10 Conclusion

A measurement of resonance neutrino interaction is done using NOMAD data. The result is reported as cross-section and ration of RES with respect to CC. Two channels are analysed: 3-track events (one muon track plus two hadron tracks) and 2-track (one muon track plus one hadron tracks). By combining the 2 channels we are able to get a very precise measurement. A total number of $49,336 \pm 838(stat) \pm 2370(syst)$ fully-corrected RES events are measured in NOMAD detector, which leads to the inclusive cross-section of RES being $0.575 \times 10^{-38} cm^3$. The ratio of RES to inclusive CC ($\sigma_{RES}/\sigma_{CC} \times E_\nu$) is measured to be $0.575(GeV)$. The statistic and systematic errors are constrained to 1.7% and 4.8%. The result is consistent with the RS model prediction (figure 2.4). This is the most precise measurement of resonance interaction so far.

Chapter 4

Relative Flux Measurement and Cosmic-Induced EM Shower in NOνA Detectors

NOνA (NuMI Off-Axis ν_e Appearance) is a long-baseline neutrino oscillation experiment designed to precisely measure the neutrino mixing angles, CP violation, and mass hierarchy by observing the oscillation of muon neutrinos to electron neutrinos. It uses muon neutrino beam generated by the Main Injector (NuMI) at Fermilab and measures it by the near detector located at Fermilab and the far detector at Ash River, MN. The NOνA detectors are constructed from extruded PVC modules filled with liquid scintillator. Two detectors are under construction: a 15 kilotons far detector which is 15.7 meters wide, 15.7 meters tall, and 78 meters long, and a 222 tons near detector designed as a smaller copy of the far detector which is 2.9 meters wide, 4.2 meters tall and 15.3 meters long.

Being a ν_e-appearance experiment, NOνA finds signal ν_e events by detecting electrons in the final state of charged current electron neutrino interaction (ν_e-CC).The biggest background to ν_e-CC signal events is from ν_μ-NC events where π^0s from hadronic showers decay into energetic photons which can fake electron-induced EM showers. Another important contribution to the background is the intrinsic ν_e in the NUMI beam. To reduce the background the particle ID identification algorithm should be able to correctly identify an EM shower as either from an electrons or a π^0. Intrinsic ν_e events should also be well constrained.

This chapter of the thesis deal with two aspects of NOνA ν_e measurement. The

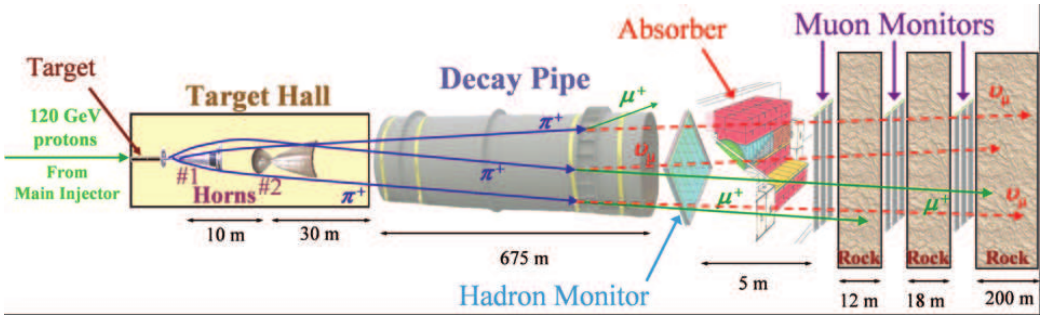

Figure 4.1 The NuMI beam production.

first part of this chapter will introduce the method of low-ν flux measurement. It uses near detector ν_μ-CC data to measure relative flux by tuning the parametrized hadron production cross-sections. We will show that beam ν_e can also be constrained by this method. The second part will present a method proposed by the University of South Carolina group at 2012 Minnesota collaboration meeting to check EM shower modelling and reconstruction efficiency using cosmic-ray-induced EM showers in NOνA detectors.

4.1 NuMI Beam

Main Injector neutrino beam (NuMI) is created at Fermilab by colliding 120 GeV protons from the Main Injector onto a graphite target. The target is a rectangular rod 6.4 mm in width, 15 mm in height, and 940 mm in length. The particles produced, including kaons and pions, are focused by two magnetic parabolic horns. The horns are able to choose positively or negatively charged particles by using forward horn current (FHC) or reverse horn current (RHC) so as to generate a beam dominated by either ν_μ or $\bar{\nu}_\mu$ The mesons then decay into neutrinos in the 675 m long, 2 m diameter steel decay pipe. This length is approximately the decay length of a 10 GeV pion. The pipe is evacuated to $\sim$0.5 Torr to reduce meson absorption and scattering. A water-cooled absorber is placed at the end of the decay pipe with

an aluminium core encased in steel to stop any remaining primary and undecayed secondary particles. The absorber is followed by 240 m of dense Dolomite rock where any muons passing through the absorber are stopped before they reach the Near Detector cavern. Ionization chambers are used to monitor the remnant hadrons and the tertiary muon from the π and K decays [32].

The NUMI neutrino beam is predominated by ν_μ (92.9%) with small contributions of $\bar{\nu}_\mu$ (5.8%) from μ^+ and π^- decays. There is a small 1.2% ν_e component which makes a background to ν_e appearance measurement in NOνA detector. The contribution from $\bar{\nu}_e$ is even smaller at 0.1%.

4.2 NOνA Detectors

Three detectors are built for the NOνA project: the Near Detector, the Far Detector, and the Near Detector Prototype [32]. All NOνA detectors are built upon PVC plastic cells filled with liquid scintilator. The light created by charged particles traversing the cell is collected by wavelength-shifting fibers(WSF) and converted to electronic signal by Avalanche Photodiode (APD) photodetectors at the top of each cell (figure 3.2). Two side by side 16-cell PVC extrusions constitute a NOνA extrusion module. a Front-End Board (FEB) is used for each module to readout signals from the APDs.

The three NOνA detectors have an identical structure and are assembled in alternating layers of vertical and horizontal extrusions as showed in figure 3.3. This structure enables the detectors to serve both as trackers and calorimeters since 70% of the mass is active liquid scintillator.

Near Detector Prototype

The prototype of the Near Detector is first assembled on the surface at Fermilab site, 110 mrad off the NUMI beam. The prototype has four blocks, each consisting of 31 planes that are 64 cells wide (2 extrusion modules) and 96 cells high (3 extrusion

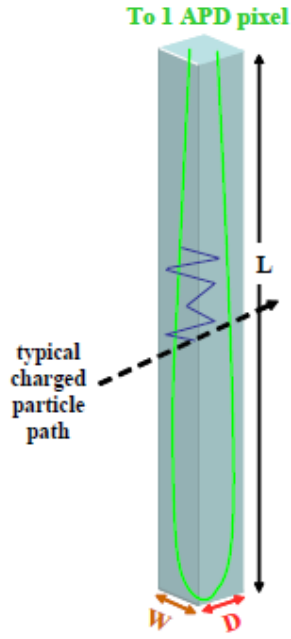

Figure 4.2 The NOνA PVC cell containing liquid scintilator and a wavelength-shifting fibers(WSF).

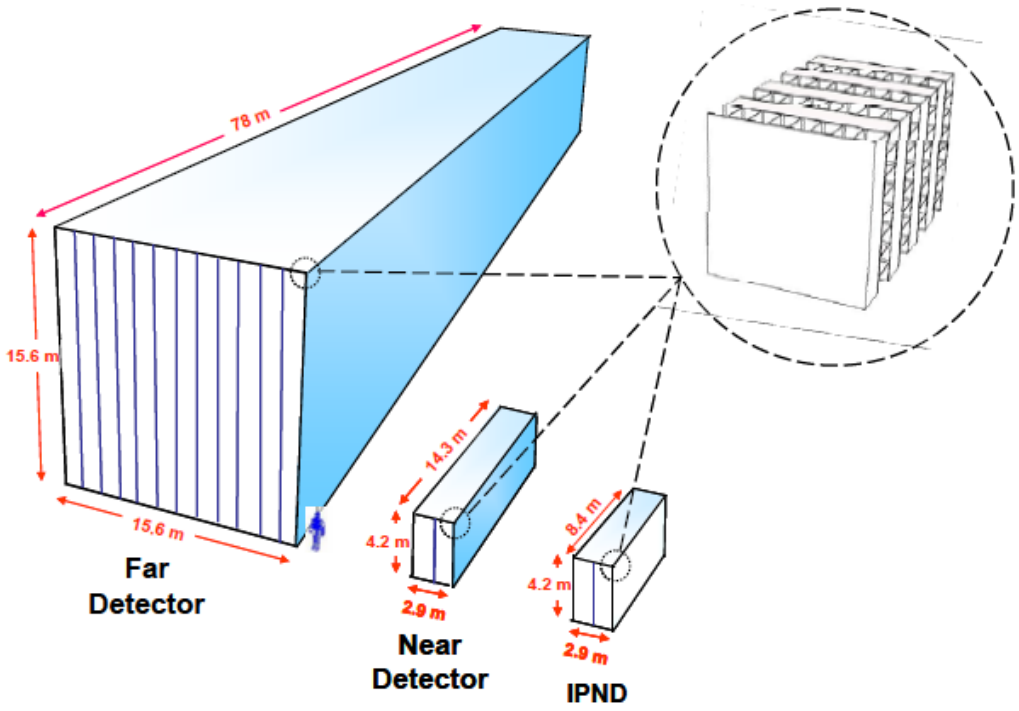

Figure 4.3 The NOνA detectors.

modules), arranged in alternating horizontal and vertical layers. It serves as part of the R&D effort to test all part of NOνA detectors

Near Detector

The Near Detector is also at the Fermilab site, 14.6 mrad off the NUMI beam. It is an identical copy of the Far Detector except with shorter extrusion modules. The detector has six blocks, each consisting of 31 planes that are 64 cells wide (2 extrusion modules) and 96 cells high (3 extrusion modules) arranged in alternating horizontal and vertical layers with an additional set of ten planes at the end.

Far Detector

The Far Detector will be located at Ash River, MN, 810.5 kilometres from Fermilab. Each plane has 12 extrusion modules, 31 such planes form a block, and 5 blocks form a Superblock. A total of 6 Superblocks plus one smaller set of 3 blocks comprise the full 1003 planes in the NOνA Far Detector. The far detector will have a total mass of 15 kilotons and will be 15.7 meters wide, 15.7 meters tall, and 78 meters long.

4.3 Low-ν Flux Measurement Method

Knowledge of neutrino flux is important in neutrino oscillation measurements. However, there are large uncertainties coming from modelling of hadron production and neutrino interaction cross-section. Low-ν flux feasurement method is a way to constrain neutrino flux using neutrino interaction data in near detector [33]. This section will present the conceptual idea behind, as well as the general procedure of this method.

The general differential cross section of neutrino interaction can be written in terms of structure functions F_1, F_2, F_3:

$$\frac{d\sigma}{dxdy} = \frac{G_F^2 M}{\pi}\left[(1-y-\frac{Mxy}{2E})F_2 + \frac{y^2}{2}2xF_1 \pm y(1-\frac{y}{2}xF_3)\right] \tag{4.1}$$

where G_F is the Fermi weak coupling constant, M is the proton mass, E is the incident neutrino energy in the lab frame, and x, y are the Bjorken scaling variables.

Using $\nu = E \times y$, differential cross-section can be re-written as

$$\frac{d\sigma}{d\nu} = A(1 + \frac{B}{A}\frac{\nu}{E} - \frac{C}{A}\frac{\nu^2}{2E^2}) \tag{4.2}$$

where

$$A = \frac{G_F^2 M}{\pi}\int F_2(x)dx \tag{4.3}$$

$$B = -\frac{G_F^2 M}{\pi}\int (F_2(x) \mp xF_3(x))dx \tag{4.4}$$

$$C = B - \frac{G_F^2 M}{\pi}\int F_2(x)R_{TERM}dx \tag{4.5}$$

$$R_{TERM} = \frac{1+\frac{2Mx}{\nu}}{1+R_L} - \frac{Mx}{\nu} - 1 \tag{4.6}$$

At $\nu \longrightarrow 0$ limit the cross-section is independent of energy, which means the number of events in a given energy bin is proportional to the neutrino flux, up to the correction of ν/E and $(\nu/E)^2$

$$N(E) \propto \phi(E) \tag{4.7}$$

Therefore by measuring neutrino interaction with low ν we are able to get a measurement of relative neutrino flux.

The procedure of low-ν flux measurement follows. The first step is to parametrize the hadron production cross-sections. The default parameters should be tuned to fit the near detector MC. The near detector MC is compared against near detector data, and a standard difference χ^2 is calculated. The fitting software (Minuit[35]) then minimizes χ^2 by tuning the parameters. For each tuning, a weight is calculated and

Table 4.1 Default BMPT parameter values from [34].

	$A(mb/GeV^2)$	B	α	β	$a(GeV^{-1})$	γ	δ	r_0	r_1
π	62.3	1.57	3.45	0.517	6.10	0.153	0.478	1.05	2.65
K	7.74	-	2.45	0.444	5.04	0.121	2γ	1.15	-3.17

applied to each MC event as the ratio of the value of parametrization function with new parameters to the one with default. The resulting MC flux will be the measured relative flux.

4.4 Hadron production Parametrization

A BMPT-type function is used to parametrize the hadron production cross-section [34]:

$$(E \times \frac{d^3\sigma}{dp^3}) = A(1-x_F)^{\alpha}(1+Bx_F)x_F^{-\beta}(1+a'(x_F)p_T+b'(x_F)p_T^2)e^{-a'(x_F)P_T}) \quad (4.8)$$

where $a'(x_F) = a/x_F^{\gamma}$ and $b'(x_F) = a^2/2x_F^{\delta}$, and $x_F = p/120$.

The ratios of positive to negative mesons π^+/π^- K^+/K^- are also parametrized:

$$r(\pi) = r_0(1+x_F)^{r_1} \quad (4.9)$$

$$r(K) = r_0(1-x_F)^{r_1} \quad (4.10)$$

There are 9 variables for pion production: A, B, α, β, a, γ, δ, r_0 and r_1. For kaon production, B vanishes, and δ is taken as 2γ. In this way a total number of 16 variables are used. Default values of the BMPT parameters are taken from [34], showed in table 3.1.

4.5 Flux Fit Test with Mockdata

We produce the mockdata sample by tuning the BMPT parameters away from default and applying weight on each event. This study serves as a good test for the low-ν fit technique.

Table 4.2 Interaction modes selected (ND MC S13-04-09, FHC)

	QE	RES	DIS	COH	NC	Tot
All	5842	9102	15945	198	8769	39865
Remid > 0.66	2296	2806	3514	81	230	8927
Fiducial	1132	1471	1849	42	137	4631

The events are selected using reconstructed information. ν_μ-CC events are selected by applying cut on RecoMuonID (ReMId), the standard muon identification package for NOνA. The cut is chosen to be at 0.66 for this test. Fiducial cuts are applied on vertex position (x, y, z): $-140cm \leq x \leq 140cm$, $-140cm \leq y \leq 140cm$, $50cm \leq z \leq 1200cm$. No low-ν cut is applied to boost statistics. The interaction mode is listed according to the truth information before and after the cuts, as showed in table 3.2. ReMId cut successfully cut off most NC events. $\sim 0.9\%$ NC are left in the final sample selected for fitting. 24% are QE, and the rest 75% are non-QE.

The event selected are divided into 2 indepent samples, one as mockdata and the other as MC. The mockdata sample is re-weighted using a set of BMPT parameters taken from best fit result in [36] A fitting program based upon TMinuit ([35]) is developed to fit MC to Mockdata by tuning BMPT parameters. Figure 3.4 shows the result. TMinuit successfully fit MC to mockdata. The re-weight of π^+ and K^+ are shown in figure 3.5 and 3.6.

This study validates the fit technique and the fitting code is ready to take ND data when available.

4.6 Beam ν_e Constraint

The measurement of ν_μ flux constrain the hadron productions, and therefore also can be used to constrain ν_e flux from the same hadron decays.

The ν_e flux is produced by μ^+ (from π^+ decay), K^+ and K^0_L decays: $\pi^+ \longrightarrow \mu^+\nu_\mu$, $\mu^+ \longrightarrow e^+\nu_e\bar{\nu}_\mu$, $K^+ \longrightarrow \pi^0 e^+\nu_e$, $K^0_L \longrightarrow \pi^- e^+\nu_e$. K^+ is constrained in ν_μ

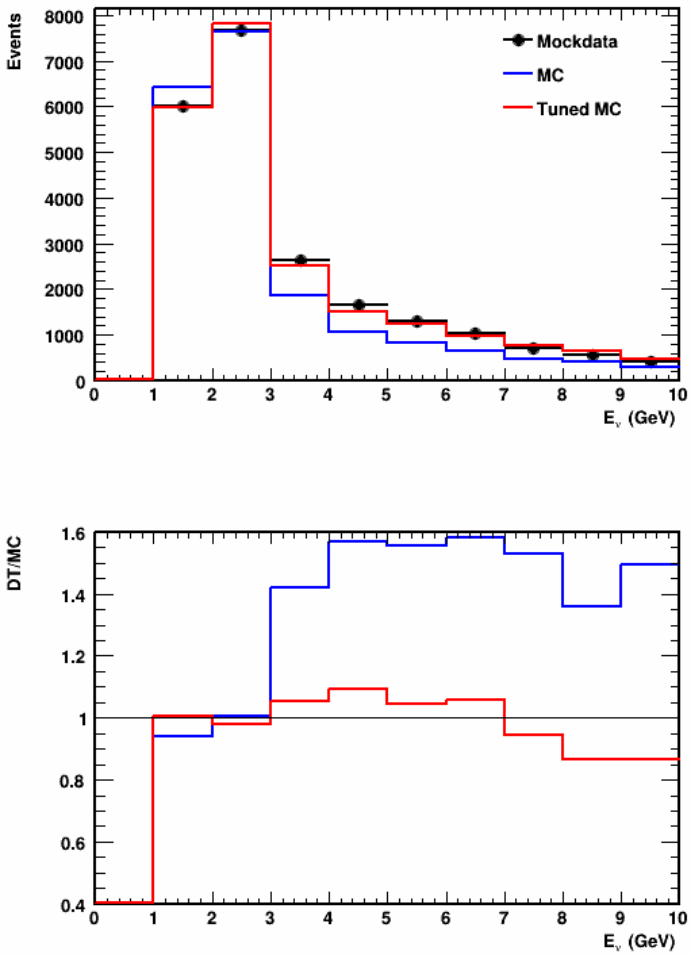

Figure 4.4 The fitting result of mockdata test.

measurement, and The μ^+ can be constrained by π fit from ν_μ measurement. K_L^0 can not be directly constrained, but can be estimated by K^+ and K^- with the formula: $K_L = (K^+ + 3K^-)/4$. Figure 3.7 shows the measured ν_μ and ν_e flux deposited by contributions from pions and kaons.

4.7 Cosmic Induced EM Shower

NOνA finds signal ν_e events by detecting electrons in the final state of charged current electron neutrino interaction (ν_e-CC). This requires correct modelling and recon-

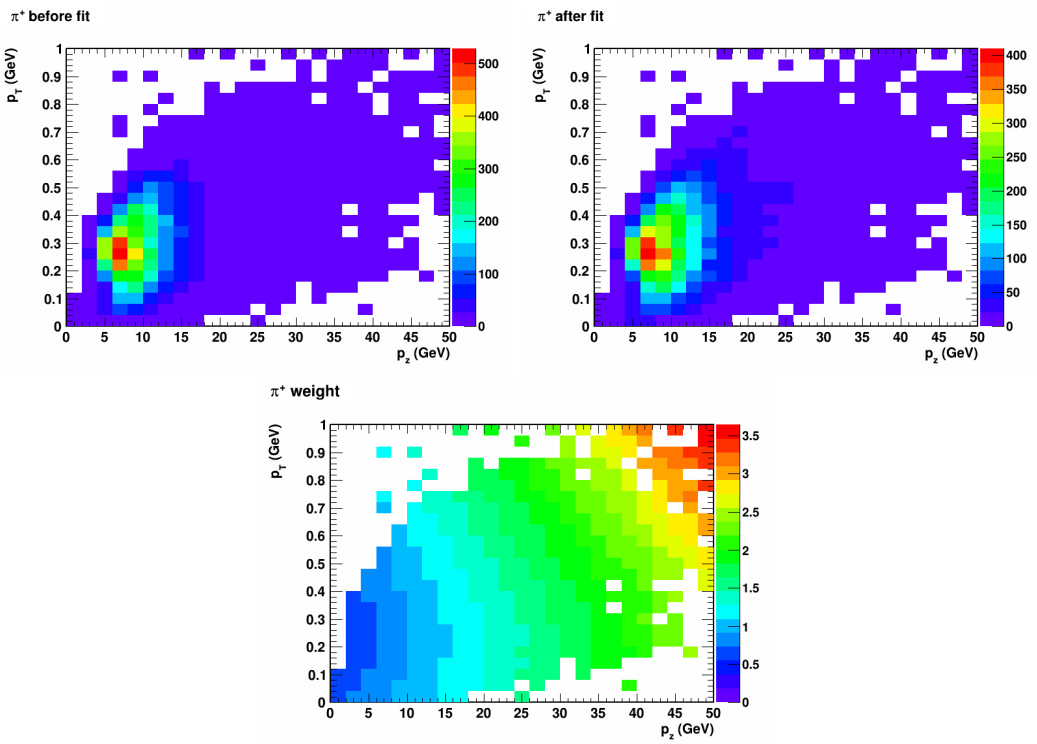

Figure 4.5 The re-weight of pion production using BMPT function in the Mockdata test. The top left plot shows the p_Z/p_T distribution of π^+ before the fitting, and the top right plot shows the p_Z/p_T distribution of π^+ after the fitting. The bottom plot is the weight applied in the p_Z/p_T space.

struction of electrons, as well as good efficiency of background rejection. The biggest background to ν_e-CC signal events is from ν_μ-NC events where π^0s from hadronic showers decay into energetic photons which can fake electron-induced EM showers. To reduce the background the particle ID identification algorithm should be able to correctly identify an EM shower as either from an electrons or a π^0.

It was proposed by the University of South Carolina group at 2012 Minnesota collaboration meeting that we can check EM shower modelling and reconstruction efficiency using cosmic-ray-induced EM showers in NOνA detectors.

Cosmic ray muons are produced by cosmic rays interacting with the upper atmosphere. Cosmic muons are abundant in NOνA detectors. Our study shows that the cosmic muon rates are approximately 72 kHz in the NOνA far detector and 22 Hz in

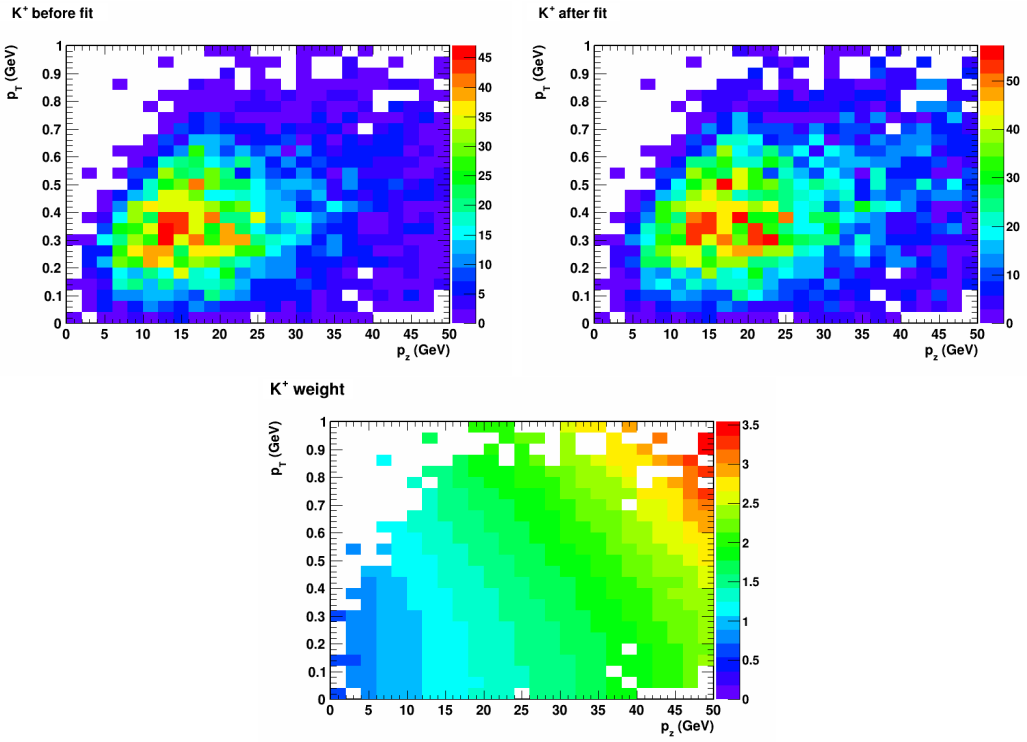

Figure 4.6 The re-weight of kaon production using BMPT function in the Mockdata test. The top left plot shows the p_Z/p_T distribution of K^+ before the fitting, and the top right plot shows the p_Z/p_T distribution of K^+ after the fitting. The bottom plot is the weight applied in the p_Z/p_T space.

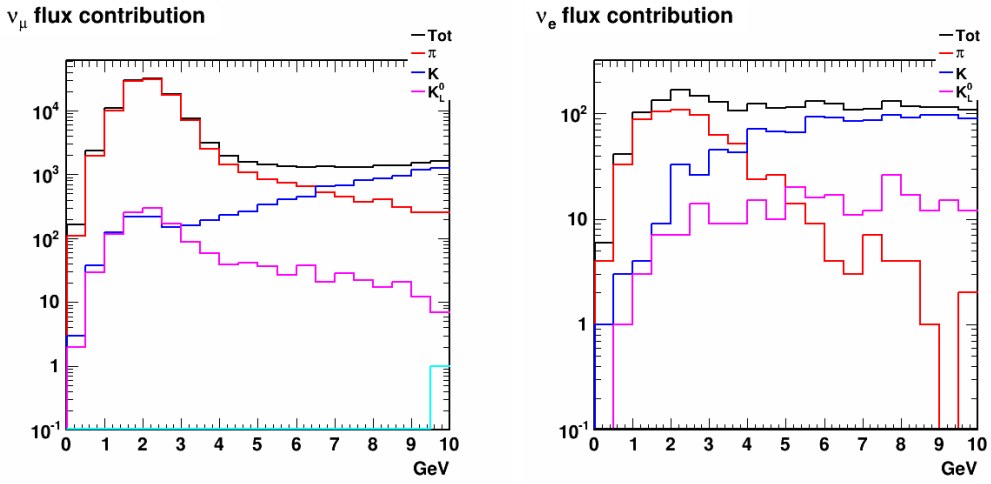

Figure 4.7 ν_μ (left) and ν_e (right) flux composition in NOνA near detector.

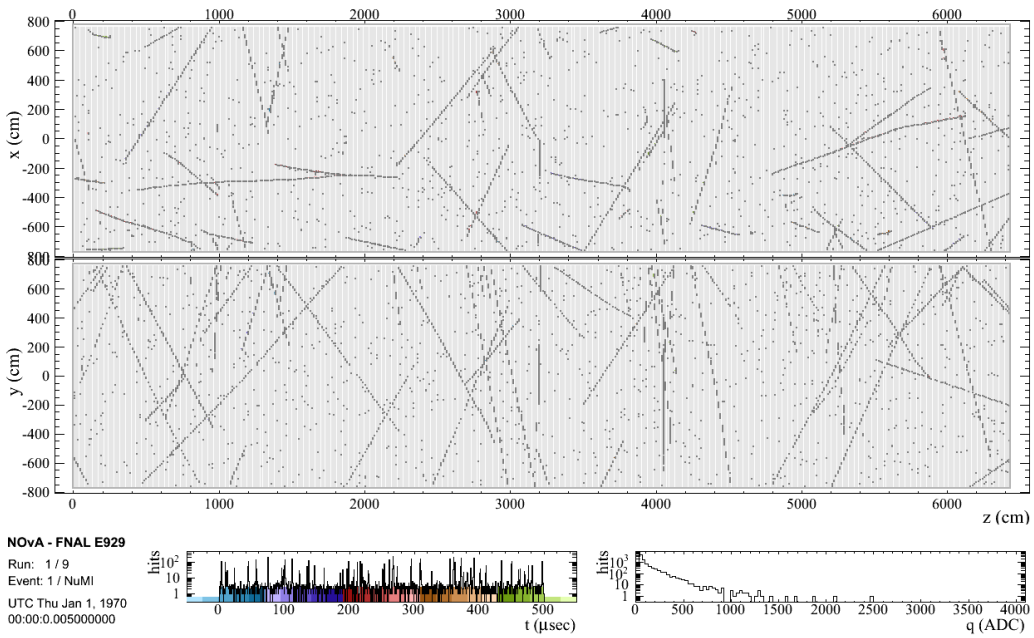

Figure 4.8 Simulated cosmic events in NOνA far detector showed as raw digits in eventdisplay.

the near detector [37].

EM showers can be induced by three types of cosmic ray muon: energetic muons undergoing bremsstrahlung radiation while traversing the detector, muons decay in flight (DiF), and muons stop in the detectors and decay into Michel electrons. Michel electrons have long been used in calibration. However, energy of Michel electrons (<0.5MeV) is small compared to energy region of beam ν_e events. DiF and bremsstrahlung muons, on the other hand, provide abundant EM shower samples at GeV energy region, which, once isolated, can be used to check EM shower modelling and reconstruction algorithms developed by the ν_e group.

However, cosmic induced EM shower is not identified and reconstructed in the current standard reconstruction in NOνA. We therefore need to develop our own method to find and isolate the shower. I break the procedure into 3 steps.

1. Shower Finding. We need to develop an EM shower finding algorithm to identify the cosmic muons with EM shower we want.

2. Muon removal. Once the EM showers are identified, they should be isolated, in both data and MC, by applying muon-removal techniques to get pure EM shower samples.

3. EM shower reconstruction and MC/data comparison. The pure EM shower samples from data and MC will be used to check the EM shower modelling and reconstruction. A MC/data comparison will be performed.

The details of the three steps above More details will be discussed in the following sections.

4.8 Shower Finding

Our estimation shows that the rate of bremsstrahlung muons is 51 Hz in the far detector and that of DiF muons is 0.1 Hz. The rates are small compared to the cosmic muon rate cited at the beginning of this section. A good shower-finding algorithm should therefore be able to pick up the muons with EM-shower from a large number of cosmic muons with good efficiency and purity.

As mentioned before, EM showers in cosmic events are not well-reconstructed. Part of bremsstrahlung shower hits are reconstructed as belonging to muon tracks; Electrons from DiF muons are also reconstructed as part of muon tracks. A characteristic of muons in NOνA detectors is that they deposit energy of roughly a *mip* in detector cells along the track. EM showers, however, can deposit much more energy in a small shower region. It is then possible that an algorithm can take the energy deposition of reconstructed muon tracks over detector planes as inputs and look for the region where the energy is significantly greater than a MIP. Examples of Bremsstrahlung and DiF showers are showed in figure 3.9.

We use the following algorithm to find the EM showers.

1. Take the reconstructed muon track, find the energy deposition along detector planes.

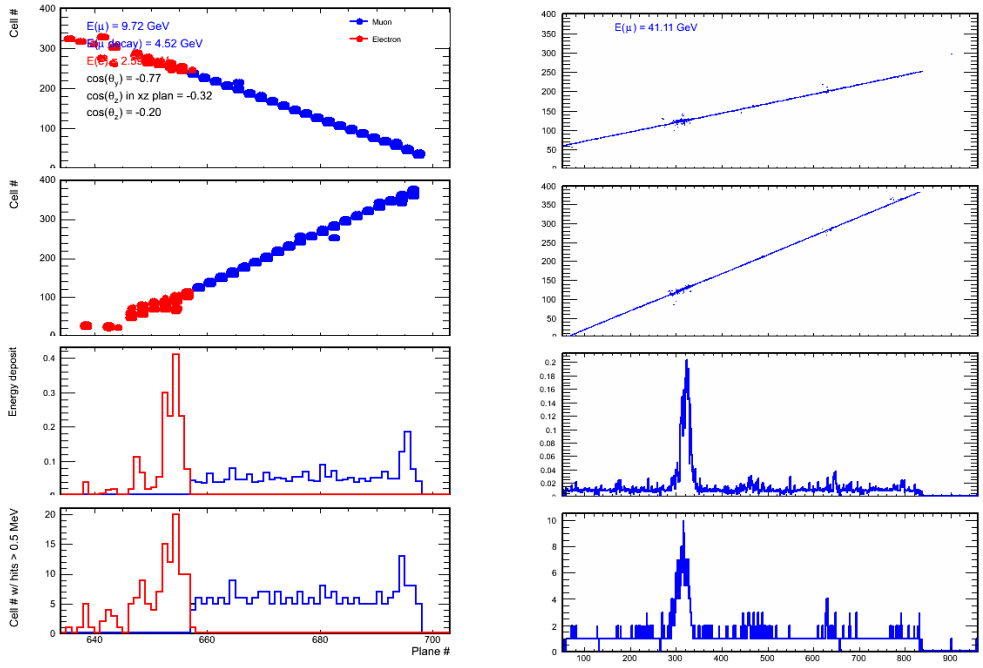

Figure 4.9 Energy deposition distribution of cosmic induced EM shower in NOνA detectors. The right figure shows a DiF muon (blue) and the electron from decay (red).The right figure show a muon with bremsstrahlung shower. Showed from top to bottom and the reconstructed hit energy in XZ view, YZ view, energy deposition over planes, and number of cell hit with energy greater than 0.5 MeV.

2. Loop over the planes from the beginning of the track to the end of the track.

3. If we find 5 consecutive planes with energy greater than 2 MIP, we call this the shower start point.

4. If we find 5 consecutive plane with energy in the range of 0.5 MIP to 1.5 MIP, we call this the shower end point.

5. If we find both the shower start and end point, then the shower is identified as Brem. If we find only the shower start point, and reach the end of track without an end point, the shower is identified as an electron from DiF.

4.9 Muon Removal

A Muon-Remove program has been developed by NOνA collaboration as a tool to simulate ν_μ-NC background using ν_μ-CC data [38]. However, this program is designed

to remove muons in beam ν_μ-CC events and cannot be applied directly to cosmic events. As a result we have to develop our own Muon-Removal technique.

To do this, we look at the slice where a cosmic muon is found. In the case of DiF muon the task is relatively simple. With a shower region defined by the shower-finding algorithm we can just remove all hits outside that region and what left will be pure electron hits. In the case of bremsstrahlung showers one additional problem is that we have a muon track inside the EM shower region. Therefore the muon-removal algorithm should be able to remove hits that belong to muon track with energy of a *mip* in the shower region. All other digits in those slices where no shower is found will be removed.

Figure 3.10 shows a muon with bremsstrahlung shower before and after muon removal. Figure 3.11 shows a DiF muon event before and ter muon removal using eventdisplay.

4.10 EM Shower Reconstruction

The showers isolated then are subject to standard EM shower reconstruction. One example product of RecoJMShower, the standard EM shower reconstruction package, is showed in figure 3.12. We want to check the shower reconstruction and particle identification process.

For this purpose, we use the raw digits of electrons from DiF events, and look at the reconstruction product such as energy and PID likelihood functions. Figure 3.13 compares the reconstructed energy against true energy. They agree well but show a slightly lower energy from reconstruction. This may be due to missing electron hits in the selection. Figure 3.14 shows the likelihood functions of electron against γ, electron against μ and electron against π^0. The result shows the efficiency of successfully identifying electrons to be 84%, 86%, and 85% respectively. In this way we validate the shower reconstruction and particle identification algorithms.

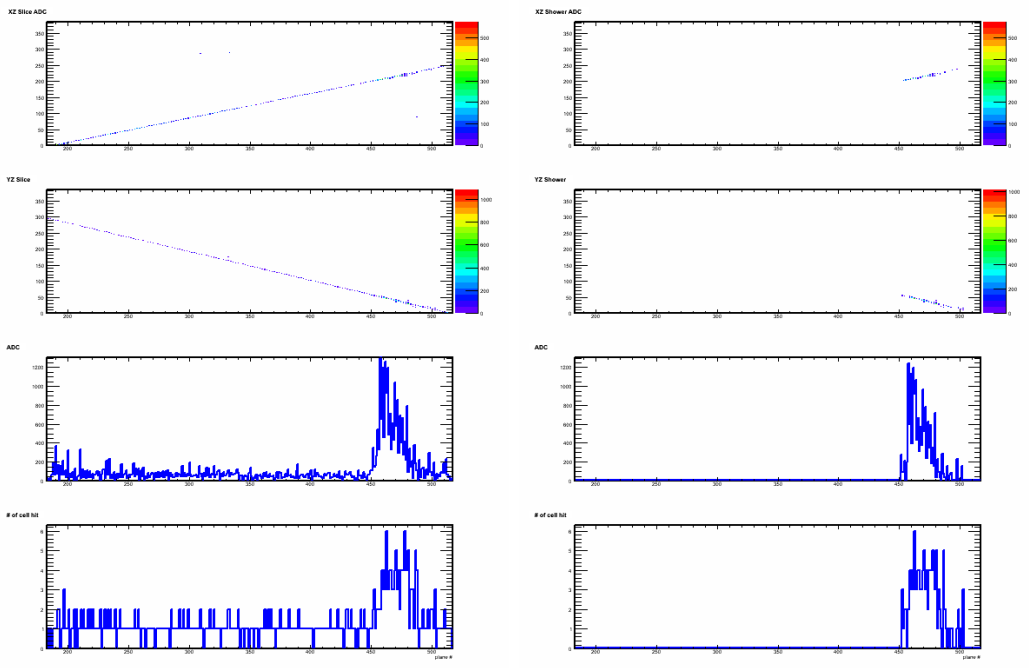

Figure 4.10 Example of Muon Remove for cosmic events. The left plot shows a muon with a bremsstrahlung shower. The right plot shows the bremsstrahlung shower after Muon Remove. Hits outside of shower regions are all removed. In the shower region, a MIP is removed. First row of each plot is the XZ view in detector; The second row is the YZ view; The third row is the sum of ADC on each plane; The fourth is the number of cell hit on each Plane. X axis is plane ID number.

4.11 Conclusion

To summarize the NOνA work: two topics are covered in this chapter: flux measurement using near detector data, and cosmic-induced EM showers. As the NOνA detectors are still under construction, those studies serve as a practice as well as a validation of the physics idea.

Using low-ν method we have shown the ability to measure relative neutrino flux using near detector ν_μ-CC data. One of the most important backgrounds to ν_e appearance measurement, beam ν_e, is constrained by this method.

In the cosmic induced EM shower study, we are able to develop an algorithm which successfully identifies the EM shower and isolates the shower digits. The muon removal method is able to remove all the muon hits other than the shower. A test

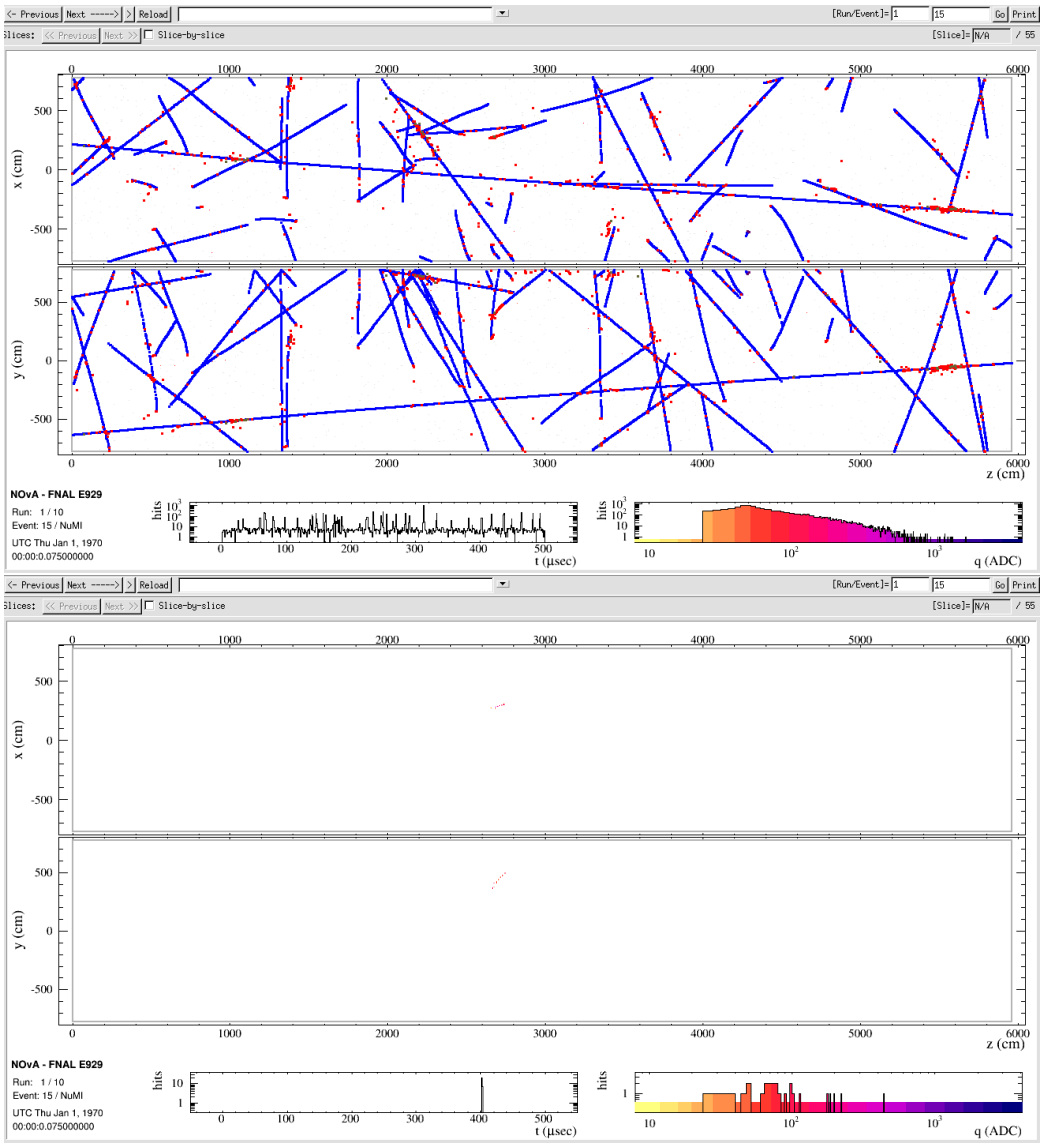

Figure 4.11 An Electron from DiF cosmic muon before (top) and after (bottom) muon-removal. The top plots showed true FLS hits, with blue being the muon hits and red being the shower hits. The bottom plot shows the raw digits of only the shower with all other digits removed.

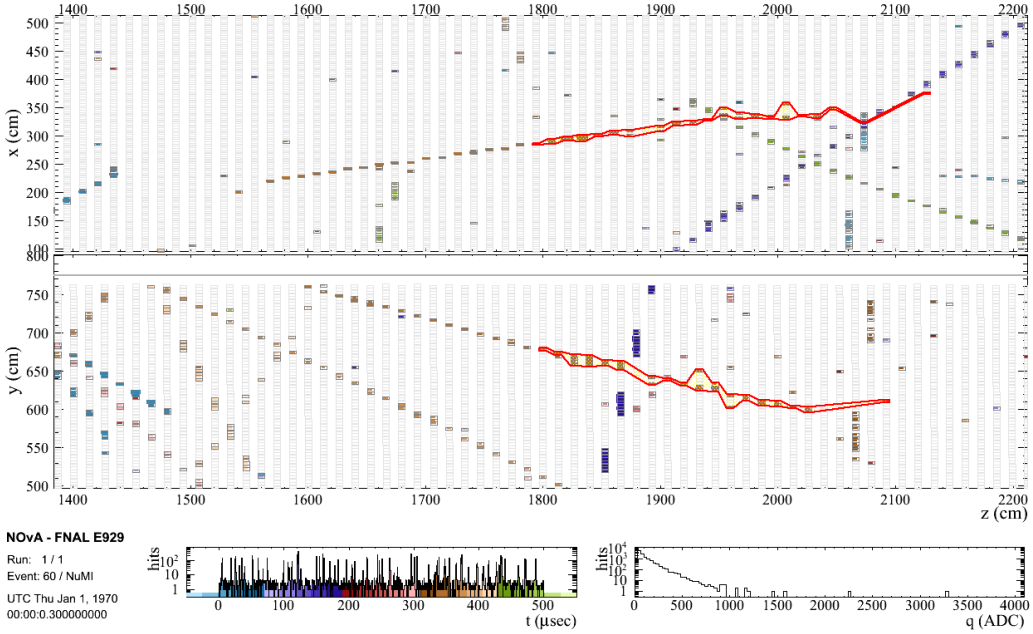

Figure 4.12 Product of RecoJMShower on a electron selected in a DiF event as showed in eventdisplay.

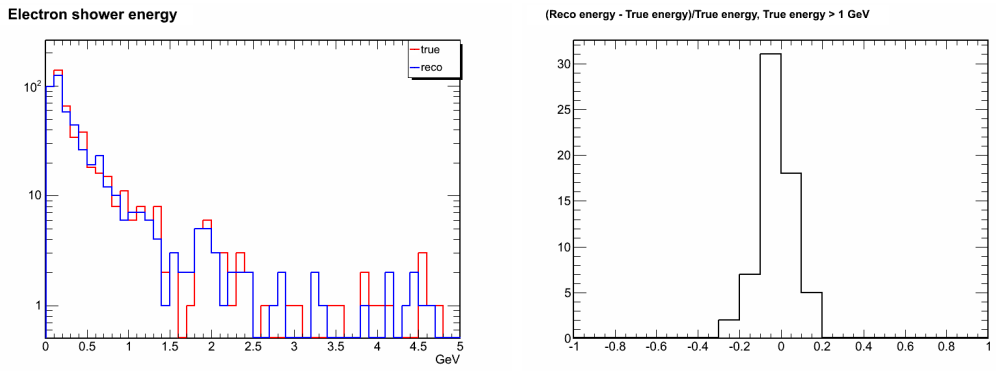

Figure 4.13 Reconstructed electron energy from DiF compared to the truth. The left figure shows the energies in log scale, and the right figure plots the difference between the two difined as (Reco energy - True energy)/(True energy).

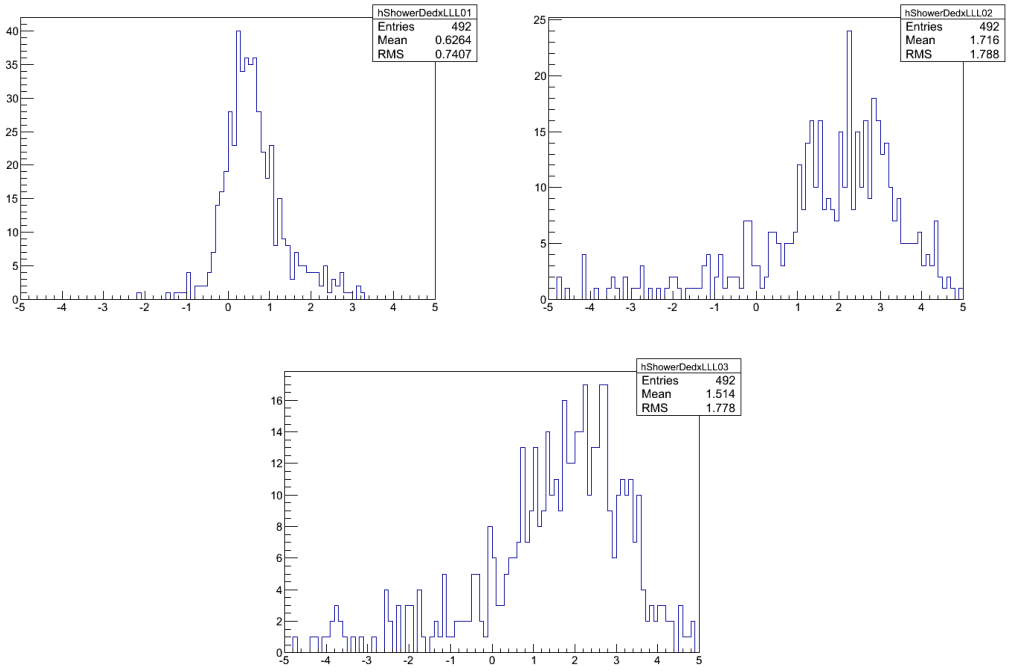

Figure 4.14 PID likelihood function difference of electron against background particles: (from left to right) likelihood of electron - likelihood of γ, likelihood of electron - likelihood of μ, likelihood of electron - likelihood of π^0. The result shows the efficiency of successfully identifying electrons to be 84%, 86%, and 85% respectively

reconstruction has been run using standard reconstruction packages on the electron digits saved from DiF MC events. This reconstruction has been checked against the truth, which validates the shower-selection process as well as the reconstruction and particle identification algorithms.

Chapter 5

CONCLUSION

This thesis has presented the measurement of ν_e appearance towards the discoveries of neutrino mixing, including the mixing angles, mass hierarchy and CP-violation. The study is performed on three experiments: NOMAD, NOνA, and LBNE, to cover different aspects of the measurement, including the signals, the backgrounds, and the neutrino flux.

The biggest contribution to ν_e appearance background comes from π^0s in ν_μ-NC. Chapter 2 uses a method of simulation and hand scan to study the ν_e signal sensitivity against NC background. In the oscillation energy region, we find ν_e efficiency to be 41.2% and NC efficiency to be 1.9%, leading to a FoM of $\sim$30. This study proves a large Water Cherenkov detector's capability in serving as the far detector for future ν_e appearance oscillation experiments.

Moreover, this study shows that in few-GeV neutrino energy region the interactions have large contributions from RES and DIS besides QE. To maximize the ν_e-appearance sensitivity, it is thus important not to bias the selection toward QE at the expense of RES and DIS channels. A better understanding of cross-sections and the energy scales of RES and DIS is therefore crucial to future oscillation experiments such as LBNE.

Chapter 3 presented the measurement of resonance interaction with the best precision so far using NOMAD data. A total number of $49,336 \pm 838(stat) \pm 2370(syst)$ fully-corrected RES events are observed in NOMAD detector, which leads to the cross-section being $0.575 \times 10^{-38} cm^3$. The ratio of RES to inclusive CC ($\sigma_{RES}/\sigma_{CC} \times E_\nu$)

is measured to be $0.575(GeV)$. The statistic and systematic uncertainties are determined to be 1.7% and 4.8% respectively. This is an important study, not only for the analysis of current ν_e appearance measurement, but also for the design of the next generation of oscillation-searching experiments.

Another examination of ν_e signal against NC background is performed in NOνA detectors in Chapter 4 using EM shower induced by cosmic rays. By removing the muon track we are able to get a pure EM shower sample from bremsstrahlung radiation or decay-in-flight muons. This sample provides an important check of the EM shower modelling in MC simulation. The EM shower reconstruction and particle identification is also validated using this method.

The final piece of the ν_e appearance measurement, the neutrino flux, is also studied in chapter 4. A low-ν technique is developed to measure relative ν_μ flux using near detector data. This measurement also constrained intrinsic beam ν_e, another dangerous background in ν_e appearance measurement.

All together, this thesis covers different aspects of ν_e appearance measurement, and contributes to current and future neutrino oscillation experiments.

Bibliography

[1] F. Reines and C. L. Cowan, Phys. Rev. **92**, (1953).

[2] G. Danby *et al.*, Phys. Rev. Lett. **9**,(1962).

[3] K. Kodama et al., Phys. Lett. B **504**, (2001).

[4] M. Maki, M. Nakagawa, and S. Sakata, Prog. Theor. Phys. **28**,870(1962).

[5] L. Wolfenstein. Phys. Rev., D17:2369,2374, (1978).

[6] D. Rein and L. M. Sehgal, Annals Phys. **133**, 79 (1981).

[7] Raymond Davis Jr., Don S. Harmer, and Kenneth C. Hoffman Phys. Rev. Lett. 20: 1205. (1968).

[8] Fukuda, Y., *et al.* Physical Review Letters 81 (8): 15621567. (1988)

[9] Y. Fukuda *et al.* , Phys. B **436** (1998)p.33.

[10] Aharmin **et al.**, [SNO collaboration], Phys. Rev. C72, 055502(2005).

[11] B. Aharmim *et al.*, Phys. Rev. C75, 045502(2007). B.

[12] K. Eguchi *et al.*, Phys. Rev. D74, 094009(2006).

[13] P. Adamson *et al.* [MINOS Collaboration], arXiv:1301.4581.

[14] K. Abe *et al.* (T2K Collaboration) , PRL 107. 041801(2011).

[15] F. P. An **et al.** [DAYA-BAY Collaboration], Phys. Rev. Lett. **108**, 171803 (2012) [arXiv:1203.1669 [hep-ex]].

[16] C. Adams *et al.* [LBNE Collaboration], arXiv:1307.7335 [hep-ex].

[17] F.M. Dufour, Ph.D. thesis, arXiv:1001.5165v1 [hep-ph], (2010).

[18] T. Barszczak, Ph.D. thesis,

[19] J. M. Conrad, arXiv:0708.2446 [hep-ex]. UC Irvine, (2005).

[20] Johannes Hoppenau, *Simulating Cylindrical Water Cherenkov Detectors Using WCSim* LBNE-DocDB-324-v2

[21] C. .Berger and L. M. Sehgal, Phys. Rev. D **76**, 113004 (2007) [arXiv:0709.4378 [hep-ph]].

[22] J. A. Formaggio and G. P. Zeller, Rev. Mod. Phys. **84**, 1307 (2012) [arXiv:1305.7513 [hep-ex]].

[23] Casper, D., Nucl. Phys. Proc. Suppl. **112**, 161 (2002)

[24] C. Andreopoulos, A. Bell, D. Bhattacharya, F. Cavanna, J. Dobson, S. Dytman, H. Gallagher and P. Guzowski *et al.*, Nucl. Instrum. Meth. A **614**, 87 (2010) [arXiv:0905.2517 [hep-ph]].

[25] Q. Wu *et al.* [NOMAD Collaboration], Phys. Lett. B **660**, 19 (2008) [arXiv:0711.1183 [hep-ex]].

[26] J. Altegoer *et al.* [NOMAD Collaboration], NIM A404, 96-128 (1998)

[27] G.Ingelman *et al.*, Comput. Phys.Comm, 101, 108-134(1997)

[28] T.SjÂĺostrand, Comput. Phys.Comm, 82, 74-90(1994)

[29] R.Brun *et al.*, CERN Program Library, W5013, 1993.

[30] M. Anfreville, P. Astier, M. Authier, A. Baldisseri, M. Banner, N. Besson, J. Bouchez and A. Castera **et al.**, Nucl. Instrum. Meth. A **481**, 339 (2002) [hep-ex/0104012].

[31] http://root.cern.ch/root/html/TMultiLayerPerceptron.html

[32] D. S. Ayres *et al.* [NOvA Collaboration], The NOvA Technical Design Report, FERMILAB-DESIGN-2007- 01.

[33] S. R. Mishra. Wold Scientific, 84âĂŞ123, 1990.

[34] M. Bonesini, A. Marchionni, F. Pietropaolo and T. Tabarelli de Fatis, Eur. Phys. J. C **20**, 13 (2001) [hep-ph/0101163].

[35] http://root.cern.ch/root/html/TMinuit.html

[36] J. Ling, Fermilab-Thesis-2010-24, MINOS-doc-7448

[37] Honguye Duyang *et al.*, *Cosmic Ray Muon Induced EM Shower in NOvA*. NOvA-doc-7742-v2

[38] Kanika Sachdev, *MRCC Overview and Analysis*. NOVA-doc-8581-v3